

NIST Special Publication 1018-5

Fire Dynamics Simulator (Version 5) Technical Reference Guide

Volume 2: Verification

Randall McDermott

Kevin McGrattan

Simo Hostikka

Jason Floyd

NIST Special Publication 1018-5

Fire Dynamics Simulator (Version 5) Technical Reference Guide

Volume 2: Verification

Randall McDermott
Kevin McGrattan
*Fire Research Division
Building and Fire Research Laboratory*

Simo Hostikka
*VTT Technical Research Centre of Finland
Espoo, Finland*

Jason Floyd
*Hughes Associates, Inc.
Baltimore, Maryland*

October 29, 2010
FDS Version 5.5
SVNRepository Revision : 6843



U.S. Department of Commerce
Gary Locke, Secretary

National Institute of Standards and Technology
Patrick Gallagher, Director

Preface

This is Volume 2 of the FDS Technical Reference Guide. Volume 1 describes the mathematical model and numerical method. Volume 3 documents past and present experimental validation work. Instructions for using FDS are contained in a separate User's Guide [1].

The three volumes of the FDS Technical Reference Guide are based in part on the “Standard Guide for Evaluating the Predictive Capability of Deterministic Fire Models,” ASTM E 1355 [2]. ASTM E 1355 defines *model evaluation* as “the process of quantifying the accuracy of chosen results from a model when applied for a specific use.” The model evaluation process consists of two main components: verification and validation. *Verification* is a process to check the correctness of the solution of the governing equations. Verification does not imply that the governing equations are appropriate; only that the equations are being solved correctly. *Validation* is a process to determine the appropriateness of the governing equations as a mathematical model of the physical phenomena of interest. Typically, validation involves comparing model results with experimental measurement. Differences that cannot be explained in terms of numerical errors in the model or uncertainty in the measurements are attributed to the assumptions and simplifications of the physical model.

Evaluation is critical to establishing both the acceptable uses and limitations of a model. Throughout its development, FDS has undergone various forms of evaluation, both at NIST and beyond. This volume provides a survey of verification work conducted to date to evaluate FDS.

About the Authors

Randall McDermott joined the research staff of the Building and Fire Research Lab in 2008. He received a B.S. degree from the University of Tulsa in Chemical Engineering in 1994 and a doctorate at the University of Utah in 2005. His research interests include subgrid-scale models and numerical methods for large-eddy simulation, adaptive mesh refinement, Lagrangian particle methods, and immersed boundary methods.

Kevin McGrattan is a mathematician in the Building and Fire Research Laboratory (BFRL) of NIST. He received a bachelors of science degree from the School of Engineering and Applied Science of Columbia University in 1987 and a doctorate at the Courant Institute of New York University in 1991. He joined the NIST staff in 1992 and has since worked on the development of fire models, most notably the Fire Dynamics Simulator.

Simo Hostikka is a Senior Research Scientist at VTT Technical Research Centre of Finland. He received a master of science (technology) degree in 1997 and a doctorate in 2008 from the Department of Engineering Physics and Mathematics of the Helsinki University of Technology. He is the principal developer of the radiation and solid phase sub-models within FDS.

Jason Floyd is a Senior Engineer at Hughes Associates, Inc., in Baltimore, Maryland. He received a bachelors of science and Ph.D. in the Nuclear Engineering Program of the University of Maryland. After graduating, he won a National Research Council Post-Doctoral Fellowship at the Building and Fire Research Laboratory of NIST, where he developed the combustion algorithm within FDS. He is currently funded by NIST under grant 70NANB8H8161 from the Fire Research Grants Program (15 USC 278f). He is the principal developer of the multi-parameter mixture fraction combustion model and control logic within FDS.

Acknowledgments

FDS is supported financially via internal funding at both NIST and VTT, Finland. In addition, support is provided by other agencies of the US Federal Government:

- The US Nuclear Regulatory Commission Office of Research has funded key validation experiments, the preparation of the FDS manuals, and the development of various sub-models that are of importance in the area of nuclear power plant safety. Special thanks to Mark Salley and Jason Dreisbach for their efforts and support. The Office of Nuclear Material Safety and Safeguards, another branch of the US NRC, has supported modeling studies of tunnel fires under the direction of Chris Bajwa and Allen Hansen.
- The Micro-Gravity Combustion Program of the National Aeronautics and Space Administration (NASA) has supported several projects that directly or indirectly benefited FDS development.
- The US Forest Service has supported the development of sub-models in FDS designed to simulate the spread of fire in the Wildland Urban Interface (WUI). Special thanks to Mark Finney and Tony Bova for their support.
- The Minerals Management Service of the US Department of the Interior funded research at NIST aimed at characterizing the burning behavior of oil spilled on the open sea or ice. Part of this research led to the development of the ALOFT (A Large Outdoor Fire plume Trajectory) model, a forerunner of FDS. Special thanks to Joe Mullin for his encouragement of the modeling efforts.

The following individuals and organizations played a role in the verification process of FDS.

- Thanks to Chris Lautenburger and Carlos Fernandez-Pello for their assistance with the “two-reaction” test case.
- Matthias Münch of the Freie Universität Berlin provided useful test cases for the basic flow solver.
- Susanne Kilian of hhpberlin (Germany) helped to debug the improved pressure solver.
- Clara Cruz, a student at the University of Puerto Rico and Summer Undergraduate Fellow at NIST, helped develop useful Matlab scripts to automate the process of compiling this Guide.
- Bryan Klein of NIST developed the source code version control system that is an essential part of the verification process.
- Anna Matala of VTT, Finland, designed the “surf mass” pyrolysis cases.
- Danielle Antonellis, a student at Worcester Polytechnic Institute and Summer Undergraduate Fellow at NIST, added the pulsating scalar verification test case.

Contents

Preface	i
About the Authors	iii
Acknowledgments	v
1 What is Verification?	1
2 Survey of Past Verification Work	3
2.1 Analytical Tests	3
2.2 Numerical Tests	4
2.3 Sensitivity Analysis	5
2.3.1 Grid Sensitivity	5
2.3.2 Sensitivity of Large Eddy Simulation Parameters	7
2.3.3 Sensitivity of Radiation Parameters	7
2.3.4 Sensitivity of Thermophysical Properties of Solid Fuels	8
2.4 Code Checking	9
3 The Basic Flow Solver	11
3.1 2D Analytical Solution to Navier-Stokes	11
3.2 Decaying Isotropic Turbulence	15
3.3 The Dynamic Smagorinsky Model	18
3.4 FDS Wall Flows Part I: Straight Channels	20
3.4.1 Formulation	20
3.4.2 Results	21
3.4.3 Conclusions	22
3.5 Analytical Solutions to the Continuity Equation	25
3.5.1 Pulsating 1D solution	25
3.5.2 Pulsating 2D solution	26
3.5.3 Stationary compression wave in 1D	27
3.5.4 Stationary compression wave in 2D	27
3.6 Scalar Transport (move_slug)	30
3.7 Energy Conservation (energy_budget)	32
3.7.1 The Heat from a Fire (energy_budget)	32
3.7.2 Gas Injection via an Isentropic Process (isentropic)	32
3.7.3 Gas Injection via a Non-Isentropic Process (isentropic2)	33
3.8 Checking for Coding Errors (symmetry_test)	36

4	Thermal Radiation	37
4.1	Radiation from parallel plate in different co-ordinate systems (plate_view_factor)	38
4.2	Radiation inside a box (radiation_in_a_box)	39
4.3	Radiation from a plane layer (radiation_plane_layer)	40
4.4	Wall Internal Radiation (wall_internal_radiation)	41
4.5	Radiation Emitted by Hot Spheres (hot_spheres)	42
4.6	Radiation Absorbed by Liquid Droplets (droplet_absorption)	43
5	Species and Combustion	45
5.1	Boundary Conditions	45
5.1.1	Specified Mass Flux (low_flux_hot_gas_filling)	45
5.2	Fractional Effective Dose (FED_Device)	46
6	Heat Conduction	49
6.1	Simple Heat Conduction Through a Solid Slab (heat_conduction)	50
6.2	Temperature-Dependent Thermal Properties (heat_conduction_kc)	51
6.3	Simple Thermocouple Model (thermocouples)	52
7	Pyrolysis	53
7.1	Mass conservation of pyrolyzed mass (surf_mass_conservation)	53
7.1.1	Pyrolysis at a Solid Surface	54
7.1.2	Pyrolysis of Discrete Particles	57
7.2	Development of surface emissivity (emissivity)	60
7.3	Enthalpy of solid materials (enthalpy)	61
7.4	A Simple Two-Step Pyrolysis Example (two_step_solid_reaction)	62
7.5	Interpreting Bench-Scale Measurements	63
7.5.1	General Theory	63
7.5.2	Using Micro-Calorimetry Data (cable_11_mcc)	64
7.5.3	Using TGA Data (birch_tga)	66
8	Lagrangian Particles	67
8.1	Momentum Transfer (particle_drag)	67
8.2	Water Droplet Evaporation (water_evaporation)	69
	Bibliography	71

Chapter 1

What is Verification?

The terms *verification* and *validation* are often used interchangeably to mean the process of checking the accuracy of a numerical model. For many, this entails comparing model predictions with experimental measurements. However, there is now a fairly broad-based consensus that comparing model and experiment is largely what is considered *validation*. So what is *verification*? ASTM E 1355 [2], “Standard Guide for Evaluating the Predictive Capability of Deterministic Fire Models,” defines verification as

The process of determining that the implementation of a calculation method accurately represents the developer’s conceptual description of the calculation method and the solution to the calculation method.

and it defines validation as

The process of determining the degree to which a calculation method is an accurate representation of the real world from the perspective of the intended uses of the calculation method.

Simply put, verification is a check of the math; validation is a check of the physics. If the model predictions closely match the results of experiments, using whatever metric is appropriate, it is assumed by most that the model suitably describes, via its mathematical equations, what is happening. It is also assumed that the solution of these equations must be correct. So why do we need to perform model verification? Why not just skip to validation and be done with it? The reason is that rarely do model and measurement agree so well in all applications that anyone would just accept its results unquestionably. Because there is inevitably differences between model and experiment, we need to know if these differences are due to limitations or errors in the numerical solution, or the physical sub-models, or both.

Whereas model validation consists mainly of comparing predictions with measurements, as documented for FDS in Volume 3 of the Technical Reference Guide, model verification consists of a much broader range of activities, from checking the computer program itself to comparing calculations to analytical (exact) solutions to considering the sensitivity of the dozens of numerical parameters. The next chapter discusses these various activities, and the rest of the Guide is devoted mainly to comparisons of various sub-model calculations with analytical solutions.

Chapter 2

Survey of Past Verification Work

This chapter documents work of the past few decades at NIST, VTT and elsewhere to verify the algorithms within FDS.

2.1 Analytical Tests

Most complex combustion processes, including fire, are turbulent and time-dependent. There are no closed-form mathematical solutions for the fully-turbulent, time-dependent Navier-Stokes equations. CFD provides an approximate solution for the non-linear partial differential equations by replacing them with discretized algebraic equations that can be solved using a powerful computer. While there is no general analytical solution for fully-turbulent flows, certain sub-models address phenomenon that do have analytical solutions, for example, one-dimensional heat conduction through a solid. These analytical solutions can be used to test sub-models within a complex code such as FDS. The developers of FDS routinely use such practices to verify the correctness of the coding of the model [3, 4]. Such verification efforts are relatively simple and routine and the results may not always be published nor included in the documentation. Examples of routine analytical testing include:

- The radiation solver has been verified with scenarios where simple objects, like cubes or flat plates, are positioned in simple, sealed compartments. All convective motion is turned off, the object is given a fixed surface temperature and emissivity of one (making it a black body radiator). The heat flux to the cold surrounding walls is recorded and compared to analytical solutions. These studies help determine the appropriate number of solid angles to be set as the default.
- Solid objects are heated with a fixed heat flux, and the interior and surface temperatures as a function of time are compared to analytical solutions of the one-dimensional heat transfer equation. These studies help determine the number of nodes to use in the solid phase heat transfer model. Similar studies are performed to check the pyrolysis models for thermoplastic and charring solids.
- Early in its development, the hydrodynamic solver that evolved to form the core of FDS was checked against analytical solutions of simplified fluid flow phenomena. These studies were conducted at the National Bureau of Standards (NBS)¹ by Rehm, Baum and co-workers [5, 6, 7, 8]. The emphasis of this early work was to test the stability and consistency of the basic hydrodynamic solver, especially the velocity-pressure coupling that is vitally important in low Mach number applications. Many numerical algorithms developed up to that point in time were intended for use in high-speed flow applications, like aerospace. Many of the techniques adopted by FDS were originally developed for

¹The National Institute of Standards and Technology (NIST) was formerly known as the National Bureau of Standards.

meteorological models, and as such needed to be tested to assess whether they would be appropriate to describe relatively low-speed flow within enclosures.

- A fundamental decision made by Rehm and Baum early in the FDS development was to use a direct (rather than iterative) solver for the pressure. In the low Mach number formulation of the Navier-Stokes equations, an elliptic partial differential equation for the pressure emerges, often referred to as the Poisson equation. Most CFD methods use iterative techniques to solve the governing conservation equations to avoid the necessity of directly solving the Poisson equation. The reason for this is that the equation is time-consuming to solve numerically on anything but a rectilinear grid. Because FDS is designed specifically for rectilinear grids, it can exploit fast, direct solvers of the Poisson equation, obtaining the pressure field with one pass through the solver to machine accuracy. FDS employs double-precision (8 byte) arithmetic, meaning that the relative difference between the computed and the exact solution of the discretized Poisson equation is on the order of 10^{-12} . The fidelity of the numerical solution of the entire system of equations is tied to the pressure/velocity coupling because often simulations can involve hundreds of thousands of time steps, with each time step consisting of two solutions of the Poisson equation to preserve second-order accuracy. Without the use of the direct Poisson solver, build-up of numerical error over the course of a simulation could produce spurious results. Indeed, an attempt to use single-precision (4 byte) arithmetic to conserve machine memory led to spurious results simply because the error per time step built up to an intolerable level.

2.2 Numerical Tests

Numerical techniques used to solve the governing equations within a model can be a source of error in the predicted results. The hydrodynamic model within FDS is second-order accurate in space and time. This means that the error terms associated with the approximation of the spatial partial derivatives by finite differences is of the order of the square of the grid cell size, and likewise the error in the approximation of the temporal derivatives is of the order of the square of the time step. As the numerical grid is refined, the “discretization error” decreases, and a more faithful rendering of the flow field emerges. The issue of grid sensitivity is extremely important to the proper use of the model and will be taken up in the next chapter.

A common technique of testing flow solvers is to systematically refine the numerical grid until the computed solution does not change, at which point the calculation is referred to as a Direct Numerical Solution (DNS) of the governing equations. For most practical fire scenarios, DNS is not possible on conventional computers. However, FDS does have the option of running in DNS mode, where the Navier-Stokes equations are solved without the use of sub-grid scale turbulence models of any kind. Because the basic numerical method is the same for LES and DNS, DNS calculations are a very effective way to test the basic solver, especially in cases where the solution is steady-state. Throughout its development, FDS has been used in DNS mode for special applications. For example, FDS (or its core algorithms) have been used at a grid resolution of roughly 1 mm to look at flames spreading over paper in a microgravity environment [9, 10, 11, 12, 13, 14], as well as “g-jitter” effects aboard spacecraft [15]. Simulations have been compared to experiments performed aboard the US Space Shuttle. The flames are laminar and relatively simple in structure, and the comparisons are a qualitative assessment of the model solution. Similar studies have been performed comparing DNS simulations of a simple burner flame to laboratory experiments [16]. Another study compared FDS simulations of a counterflow diffusion flames to experimental measurements and the results of a one-dimensional multi-step kinetics model [17].

Early work with the hydrodynamic solver compared two-dimensional simulations of gravity currents with salt-water experiments [18]. In these tests, the numerical grid was systematically refined until almost perfect agreement with experiment was obtained. Such convergence would not be possible if there were a fundamental flaw in the hydrodynamic solver.

2.3 Sensitivity Analysis

A sensitivity analysis considers the extent to which uncertainty in model inputs influences model output. Model parameters can be the physical properties of solids and gases, boundary conditions, initial conditions, *etc.* The parameters can also be purely numerical, like the size of the numerical grid. FDS typically requires the user to provide several dozen different types of input parameters that describe the geometry, materials, combustion phenomena, *etc.* By design, the user is not expected to provide numerical parameters besides the grid size, although the optional numerical parameters are described in both the Technical Reference Guide and the User's Guide.

FDS does not limit the range of most of the input parameters because applications often push beyond the range for which the model has been validated. FDS is still used for research at NIST and elsewhere, and the developers do not presume to know in all cases what the acceptable range of any parameter is. Plus, FDS solves the fundamental conservation equations and is much less susceptible to errors resulting from input parameters that stray beyond the limits of simpler empirical models. However, the user is warned that he/she is responsible for the prescription of all parameters. The FDS manuals can only provide guidance.

The grid size is the most important numerical parameter in the model, as it dictates the spatial and temporal accuracy of the discretized partial differential equations. The heat release rate is the most important physical parameter, as it is the source term in the energy equation. Property data, like the thermal conductivity, density, heat of vaporization, heat capacity, *etc.*, ought to be assessed in terms of their influence on the heat release rate. Validation studies have shown that FDS predicts well the transport of heat and smoke when the HRR is prescribed. In such cases, minor changes in the properties of bounding surfaces do not have a significant impact on the results. However, when the HRR is not prescribed, but rather predicted by the model using the thermophysical properties of the fuels, the model output is sensitive to even minor changes in these properties.

The sensitivity analyses described in this chapter are all performed in basically the same way. For a given scenario, best estimates of all the relevant physical and numerical parameters are made, and a “baseline” simulation is performed. Then, one by one, parameters are varied by a given percentage, and the changes in predicted results are recorded. This is the simplest form of sensitivity analysis. More sophisticated techniques that involve the simultaneous variation of several parameters are impractical with a CFD model because the computation time is too long and the number of parameters too large to perform the necessary number of calculations to generate decent statistics.

2.3.1 Grid Sensitivity

The most important decision made by a model user is the size of the numerical grid. In general, the finer the numerical grid, the better the numerical solution of the equations. FDS is second-order accurate in space and time, meaning that halving the grid cell size will decrease the discretization error in the governing equations by a factor of 4. Because of the non-linearity of the equations, the decrease in discretization error does not necessarily translate into a comparable decrease in the error of a given FDS output quantity. To find out what effect a finer grid has on the solution, model users usually perform some form of grid sensitivity study in which the numerical grid is systematically refined until the output quantities do not change appreciably with each refinement. Of course, with each halving of the grid cell size, the time required for the simulation increases by a factor of $2^4 = 16$ (a factor of two for each spatial coordinate, plus time). In the end, a compromise is struck between model accuracy and computer capacity.

Some grid sensitivity studies have been documented and published. Since FDS was first publicly released in 2000, significant changes in the combustion and radiation routines have been incorporated into the model. However, the basic transport algorithm is the same, as is the critical importance of grid sensitivity. In compiling sensitivity studies, only those that examined the sensitivity of routines no longer used have been

excluded.

As part of a project to evaluate the use of FDS version 1 for large scale mechanically ventilated enclosures, Friday [19] performed a sensitivity analysis to find the approximate calculation time based on varying grid sizes. A propylene fire with a nominal heat release rate was modeled in FDS. There was no mechanical ventilation and the fire was assumed to grow as a function of the time from ignition squared. The compartment was a 3 m by 3 m by 6.1 m space. Temperatures were sampled 12 cm below the ceiling. Four grid sizes were chosen for the analysis: 30 cm, 15 cm, 10 cm, 7.5 cm. Temperature estimates were not found to change dramatically with different grid dimensions.

Using FDS version 1, Bounagui *et al.* [20] studied the effect of grid size on simulation results to determine the nominal grid size for future work. A propane burner 0.1 m by 0.1 m was modeled with a heat release rate of 1500 kW. A similar analysis was performed using Alpert's ceiling jet correlation [21] that also showed better predictions with smaller grid sizes. In a related study, Bounagui *et al.* [22] used FDS to evaluate the emergency ventilation strategies in the Louis-Hippolyte-La Fontaine Tunnel in Montreal, Canada.

Xin [23] used FDS to model a methane fueled square burner (1 m by 1 m) in the open. Engineering correlations for plume centerline temperature and velocity profiles were compared with model predictions to assess the influence of the numerical grid and the size of the computational domain. The results showed that FDS is sensitive to grid size effects, especially in the region near the fuel surface, and domain size effects when the domain width is less than twice the plume width. FDS uses a constant pressure assumption at open boundaries. This assumption will affect the plume behavior if the boundary of the computational domain is too close to the plume.

Ierardi and Barnett [24] used FDS version 3 to model a 0.3 m square methane diffusion burner with heat release rate values in the range of 14.4 kW to 57.5 kW. The physical domain used was 0.6 m by 0.6 m with uniform grid spacings of 15, 10, 7.5, 5, 3, 1.5 cm for all three coordinate directions. For both fire sizes, a grid spacing of 1.5 cm was found to provide the best agreement when compared to McCaffrey's centerline plume temperature and velocity correlations [25]. Two similar scenarios that form the basis for Alpert's ceiling jet correlation were also modeled with FDS. The first scenario was a 1 m by 1 m, 670 kW ethanol fire under a 7 m high unconfined ceiling. The planar dimensions of the computational domain were 14 m by 14 m. Four uniform grid spacings of 50, 33.3, 25, and 20 cm were used in the modeling. The best agreement for maximum ceiling jet temperature was with the 33.3 cm grid spacing. The best agreement for maximum ceiling jet velocity was for the 50 cm grid spacing. The second scenario was a 0.6 m by 0.6 m 1000 kW ethanol fire under a 7.2 m high unconfined ceiling. The planar dimensions of the computational domain were 14.4 m by 14.4 m. Three uniform grid spacings of 60, 30, and 20 cm were used in the modeling. The results show that the 60 cm grid spacing exhibits the best agreement with the correlations for both maximum ceiling jet temperature and velocity on a qualitative basis.

Petterson [26] also completed work assessing the optimal grid size for FDS version 2. The FDS model predictions of varying grid sizes were compared to two separate fire experiments: The University of Canterbury McLeans Island Tests and the US Navy Hangar Tests in Hawaii. The first set of tests utilized a room with approximate dimensions of 2.4 m by 3.6 m by 2.4 m and fire sizes of 55 kW and 110 kW. The Navy Hangar tests were performed in a hangar measuring 98 m by 74 m by 15 m in height and had fires in the range of 5.5 MW to 6.6 MW. The results of this study indicate that FDS simulations with grids of 0.15 m had temperature predictions as accurate as models with grids as small as 0.10 m. Each of these grid sizes produced results within 15 % of the University of Canterbury temperature measurements. The 0.30 m grid produced less accurate results. For the comparison of the Navy Hangar tests, grid sizes ranging from 0.60 m to 1.80 m yielded results of comparable accuracy.

Musser *et al.* [27] investigated the use of FDS for course grid modeling of non-fire and fire scenarios. Determining the appropriate grid size was found to be especially important with respect to heat transfer at heated surfaces. The convective heat transfer from the heated surfaces was most accurate when the near

surface grid cells were smaller than the depth of the thermal boundary layer. However, a finer grid size produced better results at the expense of computational time. Accurate contaminant dispersal modeling required a significantly finer grid. The results of her study indicate that non-fire simulations can be completed more quickly than fire simulations because the time step is not limited by the large flow speeds in a fire plume.

2.3.2 Sensitivity of Large Eddy Simulation Parameters

FDS uses the Smagorinsky form of the Large Eddy Simulation (LES) technique. This means that instead of using the actual fluid viscosity, the model uses a viscosity of the form

$$\mu_{\text{LES}} = \rho (C_s \Delta)^2 |S| \quad (2.1)$$

where C_s is an empirical constant, Δ is a length on the order of the size of a grid cell, and the deformation term $|S|$ is related to the Dissipation Function (see FDS Technical Reference Guide [28] for details). Related to the “turbulent viscosity” are comparable expressions for the thermal conductivity and material diffusivity:

$$k_{\text{LES}} = \frac{\mu_{\text{LES}} c_p}{\text{Pr}_t} \quad ; \quad (\rho D)_{\text{LES}} = \frac{\mu_{\text{LES}}}{\text{Sc}_t} \quad (2.2)$$

where Pr_t and Sc_t are the turbulent Prandtl and Schmidt numbers, respectively. Thus, C_s , Pr_t and Sc_t are a set of empirical constants. Most FDS users simply use the default values of (0.2,0.5,0.5), but some have explored their effect on the solution of the equations.

In an effort to validate FDS with some simple room temperature data, Zhang *et al.* [29] tried different combinations of the Smagorinsky parameters, and suggested the current default values. Of the three parameters, the Smagorinsky constant C_s is the most sensitive. Smagorinsky [30] originally proposed a value of 0.23, but researchers over the past three decades have used values ranging from 0.1 to 0.23. There are also refinements of the original Smagorinsky model [31, 32, 33] that do not require the user to prescribe the constants, but rather generate them automatically as part of the numerical scheme.

2.3.3 Sensitivity of Radiation Parameters

Radiative heat transfer is included in FDS via the solution of the radiation transport equation for a non-scattering gray gas, and in some limited cases using a wide band model. The equation is solved using a technique similar to finite volume methods for convective transport, thus the name given to it is the Finite Volume Method (FVM). There are several limitations of the model. First, the absorption coefficient for the smoke-laden gas is a complex function of its composition and temperature. Because of the simplified combustion model, the chemical composition of the smokey gases, especially the soot content, can effect both the absorption and emission of thermal radiation. Second, the radiation transport is discretized via approximately 100 solid angles. For targets far away from a localized source of radiation, like a growing fire, the discretization can lead to a non-uniform distribution of the radiant energy. This can be seen in the visualization of surface temperatures, where “hot spots” show the effect of the finite number of solid angles. The problem can be lessened by the inclusion of more solid angles, but at a price of longer computing times. In most cases, the radiative flux to far-field targets is not as important as those in the near-field, where coverage by the default number of angles is much better.

Hostikka *et al.* examined the sensitivity of the radiation solver to changes in the assumed soot production, number of spectral bands, number of control angles, and flame temperature. Some of the more interesting findings were:

- Changing the soot yield from 1 % to 2 % increased the radiative flux from a simulated methane burner about 15 %

- Lowering the soot yield to zero decreased the radiative flux about 20 %.
- Increasing the number of control angles by a factor of 3 was necessary to ensure the accuracy of the model at the discrete measurement locations.
- Changing the number of spectral bands from 6 to 10 did not have a strong effect on the results.
- Errors of 100 % in heat flux were caused by errors of 20 % in absolute temperature.

The sensitivity to flame temperature and soot composition are consistent with combustion theory, which states that the source term of the radiative transport equation is a function of the absorption coefficient multiplied by the absolute temperature raised to the fourth power. The number of control angles and spectral bands are user-controlled numerical parameters whose sensitivities ought to be checked for each new scenario. The default values in FDS are appropriate for most large scale fire scenarios, but may need to be refined for more detailed simulations such as a low-sooting methane burner.

2.3.4 Sensitivity of Thermophysical Properties of Solid Fuels

An extensive amount of verification and validation work with FDS version 4 has been performed by Hietaniemi, Hostikka, and Vaari at VTT, Finland [34]. The case studies are comprised of fire experiments ranging in scale from the cone calorimeter (ISO 5660-1) to full-scale fire tests such as the room corner test (ISO 9705). Comparisons are also made between FDS results and data obtained in the SBI (Single Burning Item) Euro-classification test apparatus (EN 13823) as well as data obtained in two *ad hoc* experimental configurations: one is similar to the room corner test but has only partial linings and the other is a space to study fires in building cavities.

All of the case studies involve real materials whose properties must be prescribed so as to conform to the assumption in FDS that solids are of uniform composition backed by a material that is either cold or totally insulating. Sensitivity of the various physical properties and the boundary conditions were tested. Some of the findings were:

- The measured burning rates of various materials often fell between two FDS predictions in which cold or insulated backings were assumed for the solid surfaces. FDS lacks a multi-layer solid model.
- The ignition time of upholstery is sensitive to the thermal properties of the fabric covering, but the steady burning rate is sensitive to the properties of the underlying foam.
- Moisture content of wooden fuels is very important and difficult to measure.
- Flame spread over complicated objects, like cables laid out in trays, can be modeled if the surface area of the simplified object is comparable to that of the real object. This suggests sensitivity not only to physical properties, but also geometry. It is difficult to quantify the extent of the geometrical sensitivity.

There is little quantification of the observed sensitivities in the study. Fire growth curves can be linear to exponential in form, and small changes in fuel properties can lead to order of magnitude changes in heat release rate for unconfined fires. The subject is discussed in the FDS Validation Guide (Volume 3 of the Technical Reference Guide), where it is noted in many of the studies that predicting fire growth is difficult.

Recently, Lautenberger, Rein and Fernandez-Pello [35] developed a method to automate the process of estimating material properties to input into FDS. The methodology involves simulating a bench-scale test with the model and iterating via a "genetic" algorithm to obtain an optimal set of material properties for that particular item. Such techniques are necessary because most bench-scale apparatus do not provide a complete set of thermal properties.

2.4 Code Checking

An examination of the structure of the computer program can be used to detect potential errors in the numerical solution of the governing equations. The coding can be verified by a third party either manually or automatically with profiling programs to detect irregularities and inconsistencies [2].

At NIST and elsewhere, FDS has been compiled and run on computers manufactured by IBM, Hewlett-Packard, Sun Microsystems, Digital Equipment Corporation, Apple, Silicon Graphics, Dell, Compaq, and various other personal computer vendors. The operating systems on these platforms include Unix, Linux, Microsoft Windows, and Mac OSX. Compilers used include Lahey Fortran, Digital Visual Fortran, Intel Fortran, IBM XL Fortran, HPUX Fortran, Forte Fortran for SunOS, the Portland Group Fortran, and several others. Each combination of hardware, operating system and compiler involves a slightly different set of compiler and run-time options and a rigorous evaluation of the source code to test its compliance with the Fortran 90 ISO/ANSI standard [36]. Through this process, out-dated and potentially harmful code is updated or eliminated, and often the code is streamlined to improve its optimization on the various machines. However, simply because the FDS source code can be compiled and run on a wide variety of platforms does not guarantee that the numerics are correct. It is only the starting point in the process because it at least rules out the possibility that erratic or spurious results are due to the platform on which the code is running.

Beyond hardware issues, there are several useful techniques for checking the FDS source code that have been developed over the years. One of the best ways is to exploit symmetry. FDS is filled with thousands of lines of code in which the partial derivatives in the conservation equations are approximated as finite differences. It is very easy in this process to make a mistake. Consider, for example, the finite difference approximation of the thermal diffusion term in the ijk th cell of the three-dimensional grid:

$$\begin{aligned}
 (\nabla \cdot k \nabla T)_{ijk} \approx & \frac{1}{\delta x} \left[k_{i+\frac{1}{2},jk} \frac{T_{i+1,jk} - T_{ijk}}{\delta x} - k_{i-\frac{1}{2},jk} \frac{T_{ijk} - T_{i-1,jk}}{\delta x} \right] + \\
 & \frac{1}{\delta y} \left[k_{i,j+\frac{1}{2},k} \frac{T_{i,j+1,k} - T_{ijk}}{\delta y} - k_{i,j-\frac{1}{2},k} \frac{T_{ijk} - T_{i,j-1,k}}{\delta y} \right] + \\
 & \frac{1}{\delta z} \left[k_{ij,k+\frac{1}{2}} \frac{T_{ij,k+1} - T_{ijk}}{\delta z} - k_{ij,k-\frac{1}{2}} \frac{T_{ijk} - T_{ij,k-1}}{\delta z} \right]
 \end{aligned}$$

which is written as follows in the Fortran source code:

```

DTDX = (TMP(I+1,J,K)-TMP(I,J,K))*RDXN(I)
KDTDX(I,J,K) = .5*(KP(I+1,J,K)+KP(I,J,K))*DTDX
DTDY = (TMP(I,J+1,K)-TMP(I,J,K))*RDYN(J)
KDTDY(I,J,K) = .5*(KP(I,J+1,K)+KP(I,J,K))*DTDY
DTDZ = (TMP(I,J,K+1)-TMP(I,J,K))*RDZN(K)
KDTDZ(I,J,K) = .5*(KP(I,J,K+1)+KP(I,J,K))*DTDZ

DELKDELT = (KDTDX(I,J,K)-KDTDX(I-1,J,K))*RDX(I) +
.          (KDTDY(I,J,K)-KDTDY(I,J-1,K))*RDY(J) +
.          (KDTDZ(I,J,K)-KDTDZ(I,J,K-1))*RDZ(K)

```

This is one of the simpler constructs because the pattern that emerges within the lines of code make it fairly easy to check. However, a mis-typing of an I or a J , a plus or a minus sign, or any of a hundred different mistakes can cause the code to fail, or worse produce the wrong answer. A simple way to eliminate many of these mistakes is to run simple scenarios that have perfectly symmetric initial and boundary conditions. For example, put a hot cube in the exact center of a larger cold compartment, turn off gravity, and watch the heat diffuse from the hot cube into the cold gas. Any simple error in the coding of the energy equation will show

up almost immediately. Then, turn on gravity, and in the absence of any coding error, a perfectly symmetric plume will rise from the hot cube. This checks both the coding of the energy and the momentum equations. Similar checks can be made for all of the three dimensional finite difference routines. So extensive are these types of checks that the release version of FDS has a routine that generates a tiny amount of random noise in the initial flow field so as to eliminate any false symmetries that might arise in the numerical solution.

The process of adding new routines to FDS is as follows: typically the routine is written by one person (not necessarily a NIST staffer) who takes the latest version of the source code, adds the new routine, and writes a theoretical and numerical description for the FDS Technical Reference Guide, plus a description of the input parameters for the FDS User's Guide. The new version of FDS is then tested at NIST with a number of benchmark scenarios that exercise the range of the new parameters. Provisional acceptance of the new routine is based on several factors: (1) it produces more accurate results when compared to experimental measurement, (2) the theoretical description is sound, and (3) any empirical parameters are obtainable from the open literature or standard bench-scale apparatus. If the new routine is accepted, it is added to a test version of the software and evaluated by external users and/or NIST grantees whose research is related to the subject. Assuming that there are no intractable issues that arise during the testing period, the new routine eventually becomes part of the release version of FDS.

Even with all the code checking performed at NIST, it is still possible for errors to go unnoticed. One remedy is the fact that the source code for FDS is publicly released. Although it consists of on the order of 30,000 lines of Fortran statements, various researchers outside of NIST have been able to work with it, add enhancements needed for very specific applications or for research purposes, and report back to the developers bugs that have been detected. The source code is organized into 27 separate files, each containing subroutines related to a particular feature of the model, like the mass, momentum, and energy conservation equations, sprinkler activation and sprays, the pressure solver, *etc.* The lengthiest routines are devoted to input, output and initialization. Most of those working with the source code do not concern themselves with these lengthy routines but rather focus on the finite-difference algorithm contained in a few of the more important files. Most serious errors are found in these files, for they contain the core of the algorithm. The external researchers provide feedback on the organization of the code and its internal documentation, that is, comments within the source code itself. Plus, they must compile the code on their own computers, adding to its portability.

Chapter 3

The Basic Flow Solver

In this chapter we present test cases aimed at exercising the advective, pressure, and viscous terms, as well as the time integration for non-reacting flows.

3.1 2D Analytical Solution to Navier-Stokes

In this section we present an analytical solution that is useful for confirming the convergence rates of the truncation errors in the discretization of the terms in the governing equations. Consider the 2D incompressible Navier-Stokes equations

$$\frac{\partial \mathbf{u}}{\partial t} + \mathbf{u} \cdot \nabla \mathbf{u} = -\nabla p + \nu \nabla^2 \mathbf{u}, \quad (3.1)$$

where the velocity is given by $\mathbf{u} = [u, v]^T$, and the kinematic viscosity and pressure are denoted ν and p , respectively. An analytical solution of these equations is given by [37]

$$u(x, y, t) = 1 - A \cos(x - t) \sin(y - t) e^{-2\nu t}, \quad (3.2)$$

$$v(x, y, t) = 1 + A \sin(x - t) \cos(y - t) e^{-2\nu t}, \quad (3.3)$$

$$p(x, y, t) = -\frac{A^2}{4} [\cos(2(x - t)) + \cos(2(y - t))] e^{-4\nu t}. \quad (3.4)$$

Here, A represents an arbitrary amplitude and is assumed to take a value of 2 in this example. Note that this solution satisfies continuity for all time,

$$\nabla \cdot \mathbf{u} = 0, \quad (3.5)$$

is spatially periodic on an interval 2π in each direction, and is temporally periodic on 2π if $\nu = 0$; otherwise, the solution decays exponentially. Below we present two series of tests which demonstrate the second-order accuracy of the FDS numerical scheme and thus provide a strong form of code verification for the advective and viscous terms which are exercised.

The physical domain of the problem is a square of side $L = 2\pi$. The grid spacing is uniform $\delta x = \delta y = L/N$ in each direction with $N = \{8, 16, 32, 64\}$ for each test series. The staggered grid locations are denoted $x_i = i\delta x$ and $y_j = j\delta y$, and the cell centers are marked by an overbar, $\bar{x}_i = x_i - \delta x/2$ and $\bar{y}_j = y_j - \delta y/2$.

First, we present qualitative results for the case in which $\nu = 0$. Thus, only the advective discretization and the time integration are being tested. Figure 3.1 shows the initial and final ($t = 2\pi$) numerical solution for the case $N = 64$. As mentioned, with $\nu = 0$ the solution is periodic in time and this figure demonstrates that, as should be the case, the FDS numerical solution is unaltered after one flow-through time.

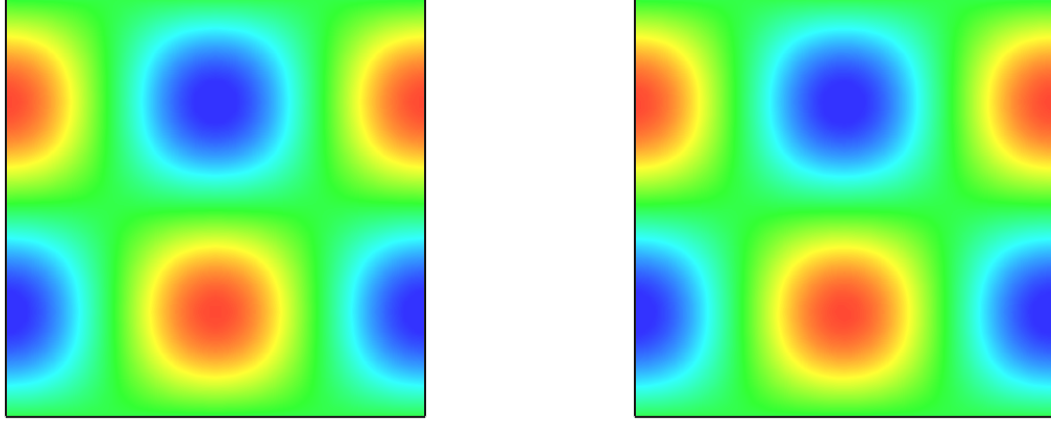


Figure 3.1: Initial and final states of the u -component of velocity.

Next, in Figure 3.2, we show time histories of the u -component of velocity at the center of the domain for the case in which $v = 0.1$. It is clearly seen that the FDS solution (thin line) converges to the analytical solution (thick line). Note that the analytical solution is evaluated at the same location as the FDS staggered grid location for the u -component of velocity, $(x_{N/2}, \bar{y}_{N/2})$, which is different in each case, $N = \{8, 16, 32, 64\}$.

Figure 3.3 is the key quantitative result of this verification test. In this figure we plot the rms error, ϵ_{rms} , in the u -component of velocity against the grid spacing. The error is defined by

$$\epsilon_{\text{rms}} \equiv \sqrt{\frac{1}{M} \sum_{k=1}^M \left[U_{ij}^k - u(x_i, \bar{y}_j, t_k) \right]^2}, \quad (3.6)$$

where M is the number of time steps and k is the time step index. The spatial indices are $(i = N/2, j = N/2)$ and U_{ij}^k represents the FDS value for the u -component of velocity at the staggered storage location for cell (i, j) at time step k ; $u(x_i, \bar{y}_j, t_k)$ is the analytical solution for the u -component at the corresponding location in space and time. The figure confirms that the advective terms, the viscous terms, and the time integration in the FDS code are convergent and second-order accurate.

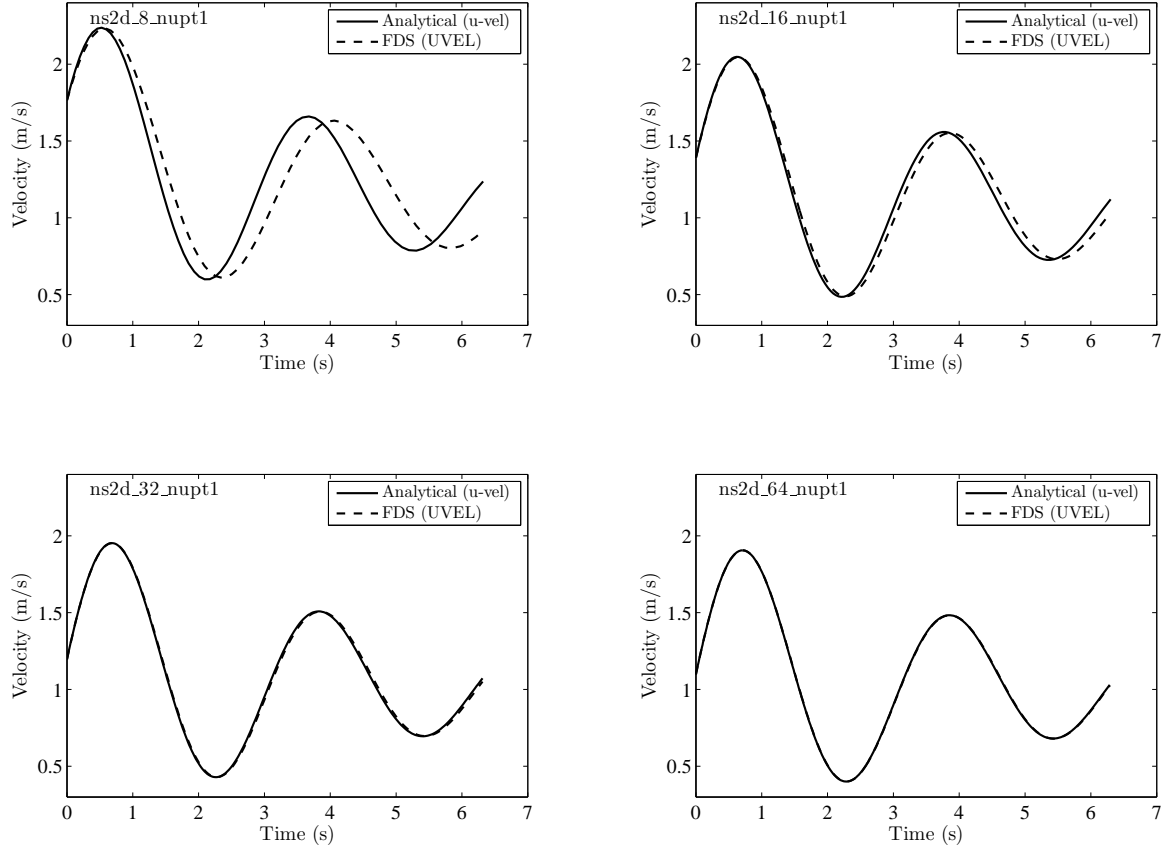


Figure 3.2: Time history of the u -component of velocity half a grid cell below the center of the domain for a range of grid resolutions. The domain is a square of side $L = 2\pi$ m. The $N \times N$ grid is uniform. Progressing from left to right and top to bottom we have resolutions $N = \{8, 16, 32, 64\}$ clearly showing convergence of the FDS numerical solution (open circles) to the analytical solution (solid line). The case is run with constant properties, $\rho = 1 \text{ kg/m}^3$ and $\mu = 0.1 \text{ kg/m/s}$, and a CFL of 0.25.

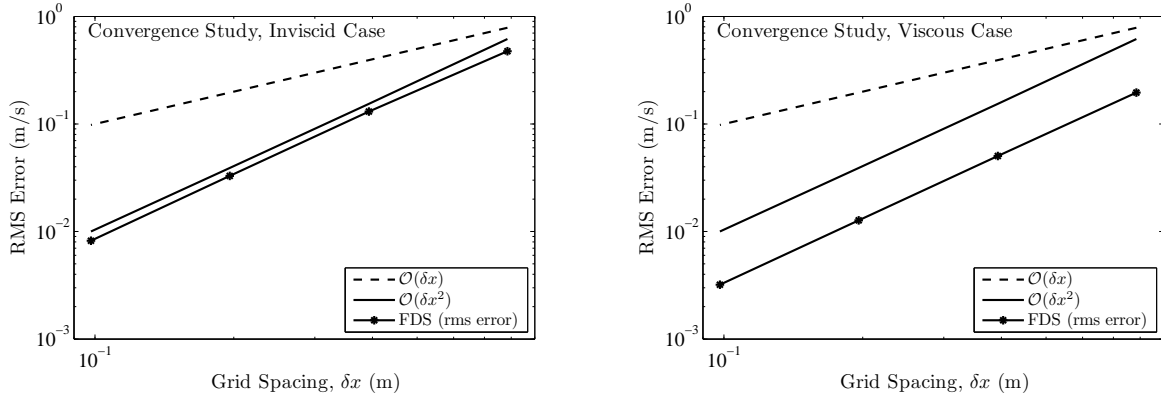


Figure 3.3: (Left) Convergence rate for the u -component of velocity with $v = 0$ showing that the advective terms in the FDS code are second-order accurate. The triangles represent the rms error in the u -component for grid spacings of $\delta x = L/N$ where $L = 2\pi$ m and $N = \{8, 16, 32, 64\}$. The solid line represents first-order accuracy and the dashed line represents second-order accuracy. The simulation is run to a time of $t = 2\pi$ s with a CFL of 0.25. The u -component at the center of the domain is compared with the analytical solution at the same location. (Right) Same case, except $v = 0.1$, showing that the viscous terms in the FDS code are second-order accurate.

3.2 Decaying Isotropic Turbulence

In this section we present a canonical flow for LES which tests whether the subgrid stress model has been coded properly. In some cases the difference between verification and validation is not so clear. Once a model is well-established and validated it may actually be used as a form of verification. Granted, such a test is not as strong a verification as the convergence study shown in Section 3.1. Nevertheless, these tests are often quite useful in discovering problems within the code. The case we examine in this section, decaying isotropic turbulence, is highly sensitive to errors in the advective and diffusive terms because the underlying physics is inherently three-dimensional and getting the problem right depends strongly on a delicate balance between vorticity dynamics and dissipation. An even more subtle yet extremely powerful verification test is also presented in this section when we set both the molecular and turbulent viscosities to zero and confirm that the integrated kinetic energy within the domain remains constant. In the absence of any form of viscosity, experience has shown that the slightest error in the advective terms or the pressure projection will cause the code to go unstable. This verification is therefore stronger than one might initially expect.

In this section we test the FDS model against the low Reynolds number (Re) data of Comte-Bellot and Corrsin (CBC) [38]. Viscous effects are important in this data set for a well-resolved LES, testing the model’s Re dependence. Following [39], we use a periodic box of side $L = 9 \times 2\pi$ centimeters (≈ 0.566 m) and $\nu = 1.5 \times 10^{-5}$ m²/s for the kinematic viscosity. The non-dimensional times for this data set are: $x/M = 42$ (initial condition), 98, and 171, where M is the characteristic mesh spacing of the CBC wind tunnel and x is the downstream location of the data station. Considering the mean velocity in the CBC wind tunnel experiment, these correspond to dimensional times of $t = 0.00, 0.28$, and 0.66 seconds in our simulations.

The initial condition for the FDS simulation is generated by superimposing Fourier modes with random phases such that the spectrum matches that of the initial CBC data. An iterative procedure is employed where the field is allowed to decay for small time increments subject to Navier-Stokes physics, each wavenumber is then injected with energy to again match the initial filtered CBC spectrum. The specific filter used here is discussed in [40].

To provide the reader with a qualitative sense of the flow, Figure 3.4 shows the initial and final states of the velocity field in the 3D periodic domain. The flow is unforced and so if viscosity is present the total energy decays with time due to viscous dissipation. Because the viscous scales are unresolved, a subgrid stress model is required. Here the stress is closed using the gradient diffusion hypothesis and the eddy viscosity is modeled by the constant coefficient Smagorinsky model with the coefficient taken to be $C_s = 0.2$ (see the Technical Reference Guide for further details).

The decay curves for two grid resolutions are shown plotted on the left in Figure 3.5. For an LES code such as FDS which uses a physically-based subgrid model, an important verification test is to run this periodic isotropic turbulence simulation in the absence of both molecular and turbulent viscosity. For so-called “energy-conserving” explicit numerics the integrated energy will remain nearly constant in time. This is demonstrated by the blue line in the top-left plot in Figure 3.5. The deviations from identical energy conservation (to machine precision) are due solely to the time discretization (the spatial terms are conservative as discussed in [41]) and converge to zero as the time step goes to the zero. Note that strict energy conservation requires implicit time integration [42, 43] and, as shown by the red curve on the same plot where only molecular viscosity is present in the simulation, this cost is unwarranted given that the molecular dissipation rate clearly overshadows the relatively insignificant amount of numerical dissipation caused by the explicit method. The FDS result using the Smagorinsky eddy viscosity (the black solid line) matches the CBC data (red open circles) well for the 32^3 case (top-left). However, the FDS results are slightly too dissipative in the 64^3 case (bottom-left). This is due to a well-known limitation of the constant coefficient Smagorinsky model: namely, that the eddy viscosity does not converge to zero at the appropriate rate as the filter width

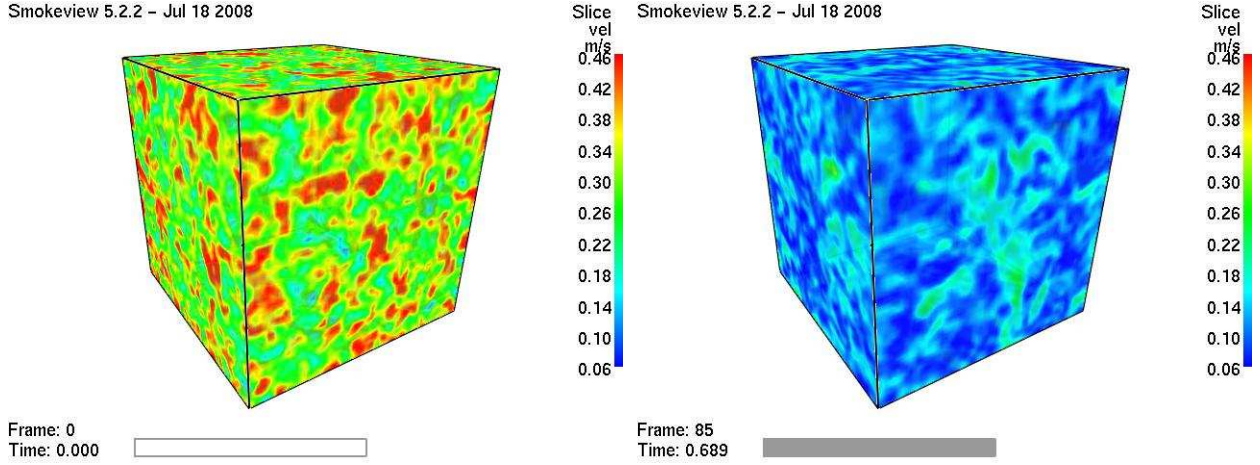


Figure 3.4: Initial and final states of the isotropic turbulence field.

(here equivalent to the grid spacing) is decreased.

To the right of each decay curve plot in Figure 3.5 is the corresponding spectral data comparison. The three black solid lines are the CBC spectral data for the points in time corresponding to dimensional times of $t = 0.00$, 0.28 , and 0.66 seconds in our simulations. As described above, the initial FDS velocity field (represented by the black dots) is specified to match the CBC data up to the grid Nyquist limit. From there the spectral energy decays rapidly as discussed in [40]. For each of the spectral plots on the right, the results of interest are the values of the red and blue dots and how well these match up with the corresponding CBC data. For the 32^3 case (top-right) the results are remarkably good. Interestingly, the results for the more highly resolved 64^3 case are not as good. This is because the viscous scales are rather well-resolved at the later times in the experiment and, as mentioned, it is well-known that the constant coefficient Smagorinsky model is too dissipative under such conditions.

Overall, the agreement between the FDS simulations and the CBC data is satisfactory and any discrepancies can be explained by limitations of the model. Therefore, as a verification the results here are positive in that nothing points to coding errors.

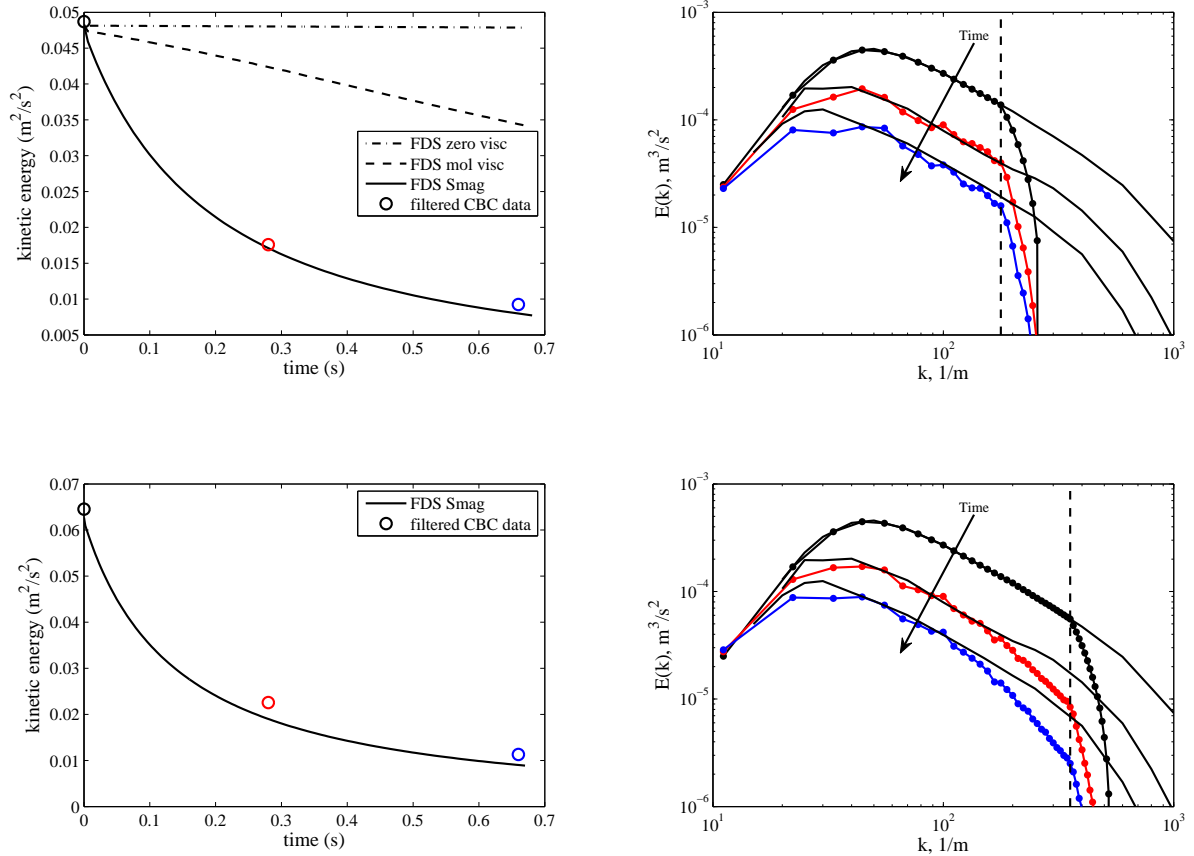


Figure 3.5: (Left) Time histories of integrated kinetic energy corresponding to the grid resolutions on the right side of the figure. In the 32^3 case (top), the CBC data (open circles) are obtained by applying a filter to the CBC energy spectra at the Nyquist limit for an $N = 32$ grid. Similarly, for the 64^3 case (bottom), the CBC data are obtained from filtered spectra for an $N = 64$ grid. Notice that the integrated FDS results for the 32^3 case compare better with the filtered CBC data than the 64^3 results. This is a well-known limitation of the constant coefficient Smagorinsky model: namely, that the eddy viscosity does not converge to zero at the appropriate rate as the filter width (here equivalent to the grid spacing) is decreased. (Right) Energy spectra for the 32^3 case (top) and the 64^3 case (bottom). The solid black lines are the spectral data of Comte-Bellot and Corrsin at three different points in time corresponding to downstream positions in the turbulent wind tunnel. The initial condition for the velocity field (spectra shown as black dots) in the FDS simulation is prescribed such that the energy spectrum matches the initial CBC data. The FDS energy spectra corresponding to the subsequent CBC data are shown by the red and blue dots. The vertical dashed line represents the wavenumber of the grid Nyquist limit.

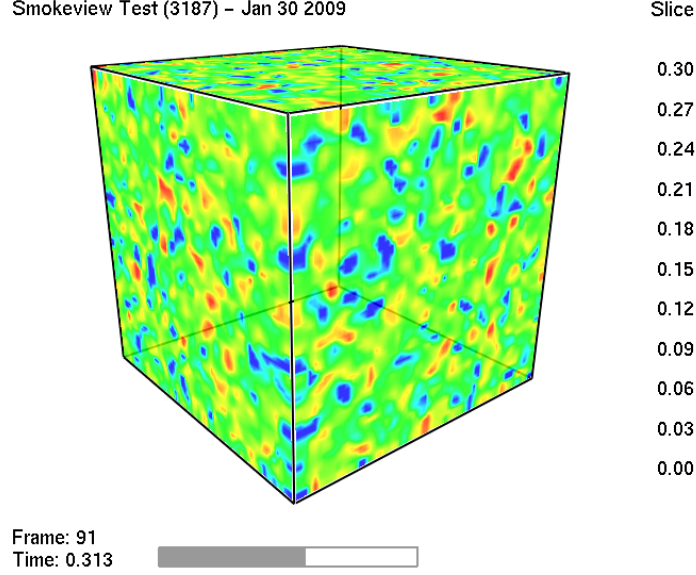


Figure 3.6: Smagorinsky coefficient for a 64^3 simulation of the CBC experiment.

3.3 The Dynamic Smagorinsky Model

In the previous section, all calculations were performed with a constant and uniform Smagorinsky coefficient, $C_s = 0.2$. For the canonical case of homogeneous decaying isotropic turbulence – *at sufficiently high Reynolds number* – this model is sufficient. However, we noticed that, even for the isotropic turbulence problem, when the grid Reynolds number is low (i.e., the flow is well-resolved) the constant coefficient model tends to over predict the dissipation of kinetic energy (see Figure 3.5). This is because the eddy viscosity does not converge to zero at the proper rate; so long as strain is present in the flow (the magnitude of the strain rate tensor is nonzero), the eddy viscosity will be nonzero. This violates a guiding principle in LES development: that the method should converge to a DNS if the flow field is sufficiently resolved [44].

The dynamic procedure for calculating the model coefficient (invoked by setting `DYNMAG = .TRUE.` on the `MISC` line) alleviates this problem. The basis of the model is that the coefficient should be the same for two different filter scales within the inertial subrange. Details of the procedure are explained in the following references [45, 46, 47, 48, 49]. Here we present results for the implementation of the dynamic model in FDS. In Figure 3.6 we show contours of the Smagorinsky coefficient $C_s(\mathbf{x}, t)$ at a time midway through a 64^3 simulation of the CBC experiment. Notice that the coefficient ranges from 0.00 to roughly 0.30 within the domain with the average value falling around 0.17.

Next, in Figure 3.7, we show results for the dynamic model analogous to Figure 3.5. For the 32^3 case the result is not dramatically different than the constant coefficient model. In fact, one might argue that the 32^3 constant coefficient results are slightly better. But there are several reasons why we should not stop here and conclude that the constant coefficient model is superior. First, as pointed out in Pope Exercise 13.34 [50], 38^3 is required to resolve 80% of the total kinetic energy (for this flow) and thus put the cutoff wavenumber within the inertial subrange of turbulent length scales. Pope recommends that simulations which are under-resolved by this criterion should be termed “very large-eddy simulations” – weather forecasting is a typical example. For a 32^3 LES, the test filter width in the dynamic model falls at a resolution of 16^3 , clearly outside the inertial range. A tacit assumption underlying the original interpretation of the dynamic model is that both the grid filter scale and the test filter scale should fall within the inertial range, since this is the

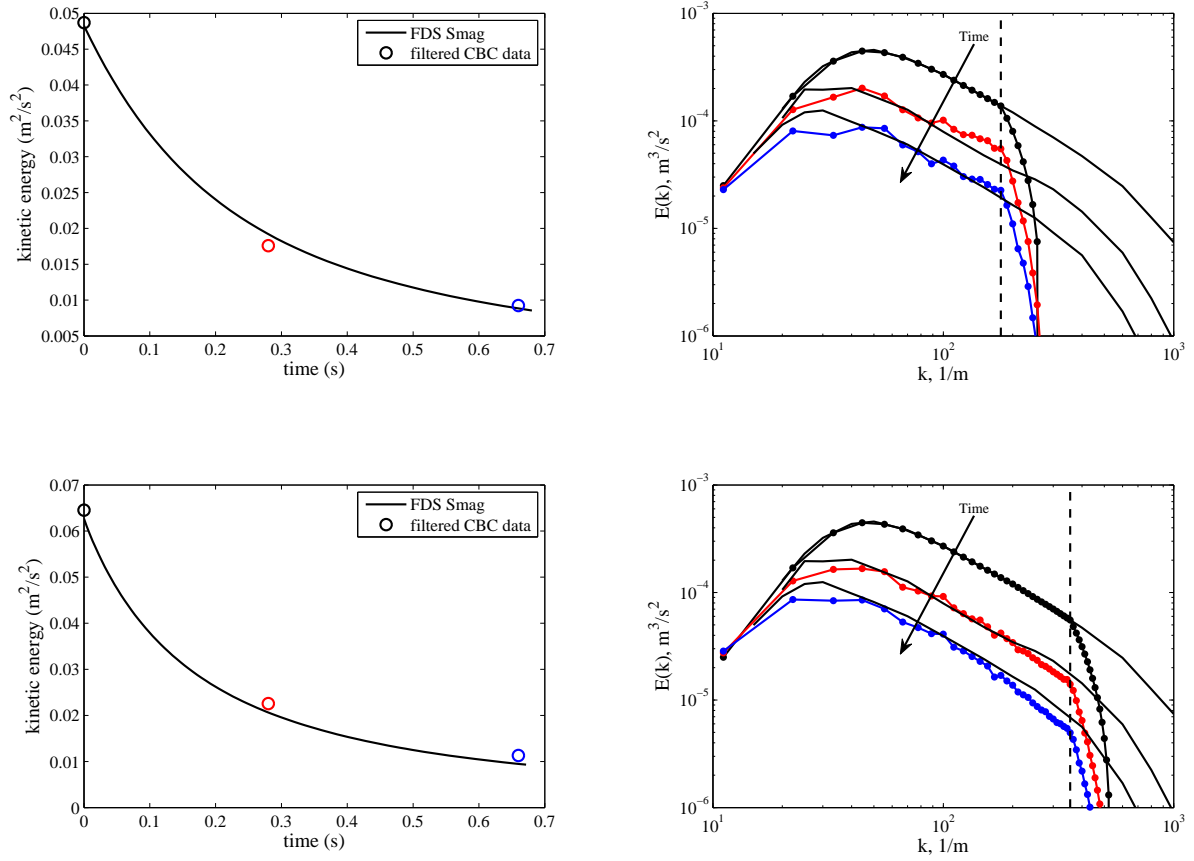


Figure 3.7: Dynamic Smagorinsky model results (analogous to Figure 3.5) for integrated kinetic energy (left) and spectra (right).

range in which the scales of turbulent motion (in theory) exhibit fractal-like, scale similar behavior (recently the procedure has been derived from other arguments [51]). With this in mind, it is perhaps not surprising that the dynamic model does not perform optimally for the low resolution case. In the higher resolution 64^3 case, however, the dynamic model does perform better than the constant coefficient model – and this is the desired result: we want better performance at higher resolution. As can be seen from the energy spectra (lower right), the energy near the grid Nyquist limit is more accurately retained by the dynamic model. This equates to better flow structure with fewer grid cells. Thus, for practical calculations of engineering interest the small computational overhead of computing the coefficient may be recuperated by a reduction in cell count.

3.4 FDS Wall Flows Part I: Straight Channels

Wall flows are notoriously challenging for large-eddy simulation (LES) [52, 53, 54, 50, 55]. In spite of their promise and sophistication, practical LES codes are resigned to *model* the wall shear stress as opposed to *resolving* the dynamically important length scales near the wall.

In this work we introduce the Werner and Wengle (WW) wall model [56] and the rough wall log law from Pope [50] into the NIST Fire Dynamics Simulator (FDS) as a practical first step in developing models for turbulent flow around complex geometry and over complex terrain. Such models are required in order for FDS to accurately model, for example, tunnel fires, smoke transport in complex architectures, and wildland-urban interface (WUI) fires [57]. As a minimum requirement, a wall model should accurately reproduce the mean wall stress for flow in a straight channel. We verify that this is true for FDS by reproducing the Moody chart, a plot of friction factor versus Reynolds number for pipe flow [58].

The remainder of this section is organized as follows. In Section 3.4.1 we describe the model formulation. Then, in Section 3.4.2, we conduct a verification study of the wall boundary conditions for laminar and turbulent flows in FDS. From this study we are able to draw quantitative conclusions in Section 3.4.3 about the accuracy of the channel flow simulations for smooth and rough walls.

3.4.1 Formulation

Details of the FDS formulation are given in the Technical Guide [28]. Here we provide only the salient components of the model necessary for treatment of constant density channel flow.

The filtered continuity and momentum equations are:

$$\frac{\partial \bar{u}_i}{\partial x_i} = 0, \quad (3.7)$$

$$\frac{\partial \bar{u}_i}{\partial t} + \frac{\partial \bar{u}_i \bar{u}_j}{\partial x_j} = -\frac{1}{\rho} \left[\frac{dp}{dx_i} + \frac{\partial \bar{p}}{\partial x_i} + \frac{\partial \bar{\tau}_{ij}}{\partial x_j} + \frac{\partial \tau_{ij}^{sgs}}{\partial x_j} \right], \quad (3.8)$$

where $\tau_{ij}^{sgs} \equiv \rho(\bar{u}_i \bar{u}_j - \bar{u}_i \bar{u}_j)$ is the subgrid-scale (sgs) stress tensor, here modeled by gradient diffusion with dynamic Smagorinsky [45] used for the eddy viscosity. In this work we specify a constant pressure drop dp/dx in the streamwise direction to drive the flow. The hydrodynamic pressure \bar{p} is obtained from a Poisson equation which enforces (3.7).

When (3.8) is integrated over a cell adjacent to a smooth wall in an LES it turns out that the most difficult term to handle is the viscous stress at the wall, e.g. $\bar{\tau}_{xz}|_{z=0}$, because the wall-normal gradient of the streamwise velocity component cannot be resolved. Note that the sgs stress at the wall is identically zero. We have, therefore, an entirely different situation than exists in the bulk flow at high Reynolds number where the viscous terms are negligible and the sgs stress is of critical importance. The quality of the sgs model still influences the wall stress, however, since other components of the sgs tensor affect the value of the near-wall velocity and hence the resulting viscous stress determined by the wall model. In particular, it is important that the sgs model is *convergent* (in the sense that the LES formulation reduces to a DNS as the filter width becomes small) so that as the grid is refined we can expect more accurate results from the simulation. For smooth walls the model used for $\tau_w = \bar{\tau}_{xz}|_{z=0}$ in this work is the Werner and Wengle model [56] which is described in detail in the FDS Tech Guide.

For rough walls the momentum flux normal to the wall is balanced by inviscid drag forces on the surface elements [59]. In this case FDS models the stress by a rough wall log law (see Pope [50]). Details are provided in the Tech Guide.

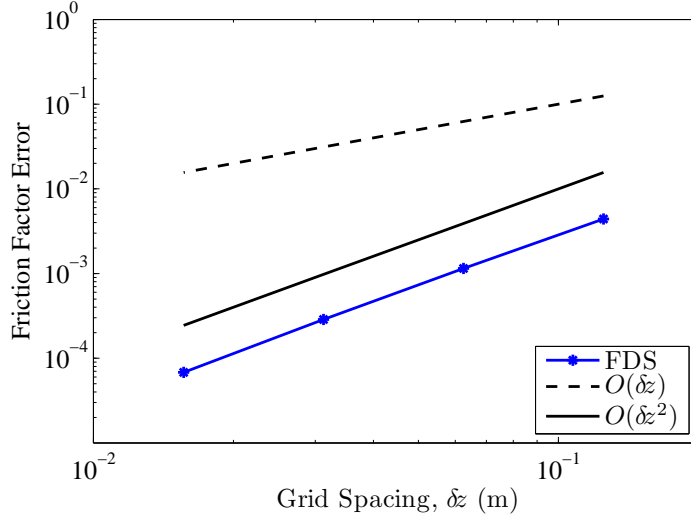


Figure 3.8: FDS exhibits second-order convergence for laminar (Poiseuille) flow in a 2D channel.

3.4.2 Results

Laminar

As verification of the no-slip boundary condition and further verification of the momentum solver in FDS, we perform a simple 2D laminar (Poiseuille) flow calculation of flow through a straight channel. The height of the channel is $H = 1$ m and the length of the channel is $L = 8$ m. The number of grid cells in the streamwise direction x is $N_x = 8$. The number of cells in the wall-normal direction z is varied $N_z = \{8, 16, 32, 64\}$. The fluid density is $\rho = 1.2 \text{ kg m}^{-3}$ and the viscosity is $0.025 \text{ kg m}^{-1} \text{ s}^{-1}$. The mean pressure drop is prescribed to be $dp/dx = -1 \text{ Pa m}^{-1}$ resulting in $Re_H \approx 160$. The (Moody) friction factor f , which satisfies

$$\Delta p = f \frac{L}{H} \frac{1}{2} \rho \bar{u}^2, \quad (3.9)$$

is determined from the steady state mean velocity \bar{u} which is output by FDS for the specified pressure drop. The exact friction factor for this flow is $f_{exact} = 24/Re_H$. The friction factor error $|f - f_{exact}|$ is plotted for a range of grid spacings $\delta z = H/N_z$ in Figure 3.8 demonstrating second-order convergence of the laminar velocity field.

Turbulent

Smooth Walls To verify the WW wall model for turbulent flow we perform 3D LES of a square channel with periodic boundaries in the streamwise direction and a constant and uniform mean pressure gradient driving the flow. The problem set up is nearly identical to the laminar cases of the previous section except here we perform 3D calculations and maintain cubic cells as we refine the grid: we hold the ratio 8:1:1 between $N_x:N_y:N_z$ for all cases. The cases shown below are identified by their grid resolution in the z direction. The velocity field is initially at rest and develops in time to a mean steady state driven by the specified mean pressure gradient. The presence of a steady state is the result of a balance between the

Table 3.1: Case matrix and friction factor results for turbulent channel flow with smooth walls. The height of the first grid cell δz is given in viscous units z^+ for each case. Additionally, the table gives the nominal Reynolds number Re_H and the FDS friction factor results compared to the Colebrook equation (3.10).

dp/dx	z^+			Re_H	f FDS	f Colebrook	rel. error
(Pa/m)	$N_z = 8$	$N_z = 16$	$N_z = 32$		($N_z = 32$)	Eq. (3.10)	%
-0.01	190	95	47	5.9×10^4	0.0212	0.0202	4.8
-1.	1.9×10^3	950	470	7.5×10^5	0.0128	0.0122	4.6
-100.	1.9×10^4	9.5×10^3	4.7×10^3	9.8×10^6	0.0077	0.0081	6.0

streamwise pressure drop and the integrated wall stress from the WW model. FDS outputs the planar average velocity in the streamwise direction and once a steady state is reached this value is used to compute the Reynolds number and the friction factor. Table 3.1 provides a case matrix: nine cases for three values of specified pressure drop and three grid resolutions. The nominal Reynolds number (obtained post-run) is listed along with the friction factor from the most refined FDS case and the friction factor computed (iteratively) from the Colebrook equation,

$$\frac{1}{\sqrt{f}} = -2.0 \log_{10} \left(\frac{z_0/H}{3.7} + \frac{2.51}{Re_H \sqrt{f}} \right), \quad (3.10)$$

which is a fit to the turbulent range of the Moody chart (for example, see Ref. [60]). The parameter z_0/H is the relative roughness where H is the hydraulic diameter of the pipe or channel and Re_H is the Reynolds number based on H . To provide a qualitative picture of the flow field, Figure 3.9 shows contours of streamwise velocity for the case $dp/dx = -1 \text{ Pa m}^{-1}$ and $N_z = 32$.

Rough Walls With the same grid set up as described above the smooth walls, a series of cases labeled as z_0^* in the repository were run at various roughness heights, grid resolutions, and Reynolds numbers. The results are presented together with the smooth wall cases in Fig. 3.10. The laminar cases provide accurate results for two different Reynolds numbers. As can be seen, both the smooth wall and rough wall treatments behave well over the range tested.

3.4.3 Conclusions

In this work the FDS wall model has been verified for both laminar and turbulent flow through straight channels with smooth or rough walls. It is shown that for the laminar (DNS) case FDS is second-order accurate. It is suggested elsewhere that, as a rule of thumb, 10 % accuracy is the best that can be expected from friction factor calculations of turbulent flow [60]. The Werner and Wengle wall model is adapted to variable density flows (though only constant density flows are tested here) for smooth walls and it is shown that FDS is capable of reproducing friction factors for a broad range of Reynolds numbers to within 6.0 % relative accuracy. A log law for rough walls is adopted to FDS with similar results.

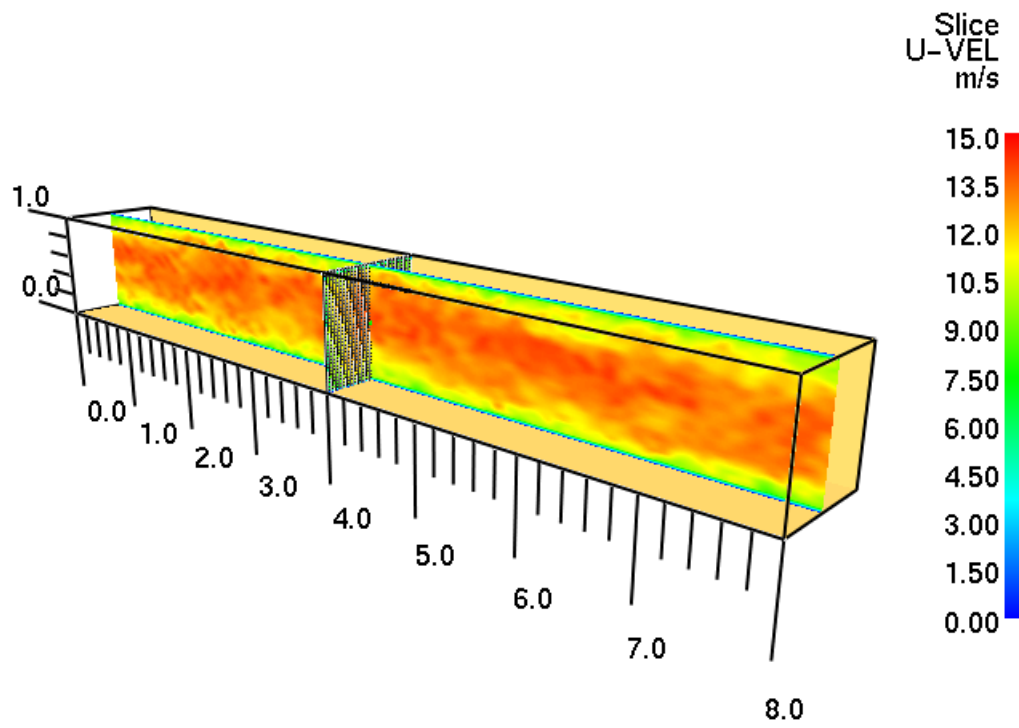


Figure 3.9: LES of square channel flow with smooth walls and periodic streamwise boundaries using dynamic Smagorinsky and the Werner Wengle wall model. For this image $N_z = 32$ and the mean pressure drop is $dp/dx = -1 \text{ Pa m}^{-1}$ resulting in $Re_H = 7.5 \times 10^5$ and a friction factor of $f = 0.0128$.

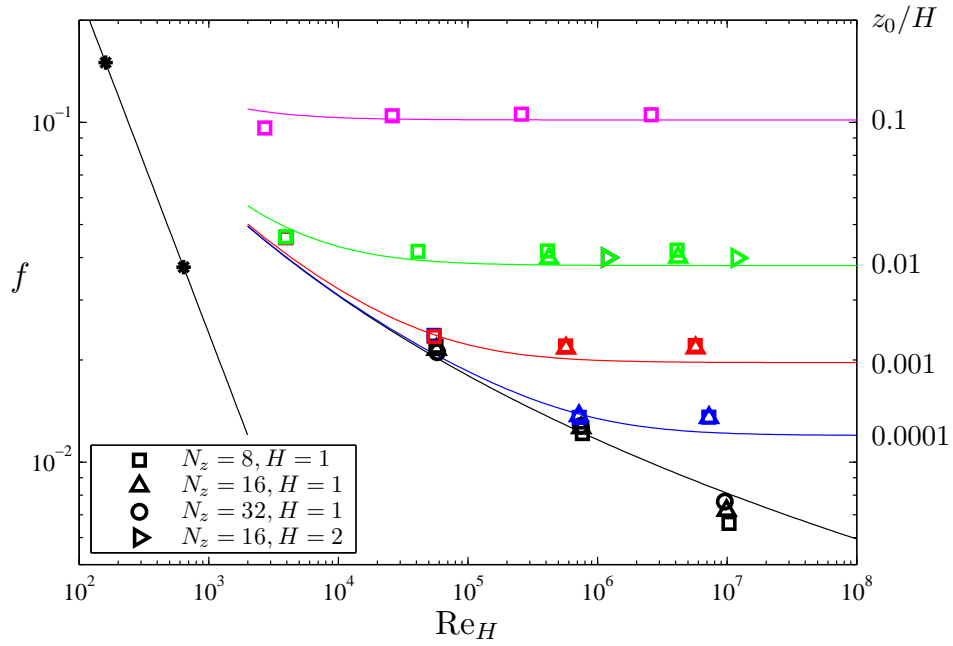


Figure 3.10: The FDS Moody Chart: friction factor, f , versus Reynolds number, Re . The solid line for $Re < 2000$ is the analytical result for 2D Poiseuille flow, $f = 24/Re$. The solid lines for $Re > 2000$ (from the Colebrook equation (3.10)) are for turbulent flow at various levels of relative roughness z_0/H shown on the right axis. Stars are DNS results from FDS at a single grid resolution ($N_z = 64$). Symbols are FDS results for 3D LES with dynamic Smagorinsky. Black symbols show results for the Werner Wengle wall model at three grid resolutions ($N_z = \{8, 16, 32\}$). Colored symbols are FDS results for the rough wall cases at different grid resolutions and relative roughnesses as differentiated by the symbol shapes.

3.5 Analytical Solutions to the Continuity Equation

Analytical solutions for primitive flow variables (density, velocity, pressure, etc.) are useful in the development and testing of numerical schemes for computational fluid dynamics (CFD). For example, an analytical solution to the 2D incompressible Navier-Stokes (NS) equations is presented in Section 3.1 and is used to verify the spatial and temporal accuracy of momentum equation. However, to our knowledge, there are no similar (i.e., time dependent and periodic in space) analytical solutions for the compressible NS equations, which could be used for verification of both compressible and variable-density low-Mach flow solvers.

The aim of the present work is to take a small step toward developing such analytical solutions. The main idea is that, given a specified velocity field, the continuity equation can be rearranged into a linear hyperbolic PDE for the logarithm of the density. Let ρ denote the density and let $\mathbf{u} = [u, v]^T$ denote the velocity. The continuity equation (conservation of mass) can then be written as

$$\frac{\partial \ln \rho}{\partial t} + \mathbf{u} \cdot \nabla \ln \rho + \nabla \cdot \mathbf{u} = 0. \quad (3.11)$$

Further, for certain, simple specifications of the velocity, this PDE can be solved using the method of characteristics.

In what follows we present 1D and 2D solutions to (3.11) for two basic irrotational flow fields. All the solutions are periodic in space. The first configuration is a pulsating flow that cycles between compressing the fluid toward the center and then the corners of the domain. In the second configuration, time periodicity is achieved by using a constant and uniform advection velocity in combination with the compression waves. This results in a solution with a qualitatively different character than the first.

3.5.1 Pulsating 1D solution

We specify the velocity as

$$u(x, t) = B \sin(x) \cos(\omega t), \quad (3.12)$$

where B is a constant amplitude and ω is the frequency of the compression cycle. The velocity divergence in 1D is then

$$\frac{\partial u}{\partial x} = B \cos(x) \cos(\omega t). \quad (3.13)$$

Let $q \equiv \ln \rho$ (this notation is used through out this work). The 1D continuity equation can then be written as the following linear hyperbolic PDE:

$$\frac{\partial q}{\partial t} + B \sin(x) \cos(\omega t) \frac{\partial q}{\partial x} + B \cos(x) \cos(\omega t) = 0, \quad (3.14)$$

which can be solved using the method of characteristics to obtain the solution

$$q(x, t) = q(x_0[x, t], 0) + \ln \left\{ \frac{1 + \tan^2 \left(\frac{x_0[x, t]}{2} \right) \exp \left(\frac{2B}{\omega} \sin[\omega t] \right)}{1 + \tan^2 \left(\frac{x_0[x, t]}{2} \right)} \right\} - \frac{B}{\omega} \sin(\omega t), \quad (3.15)$$

where the initial position is given by

$$x_0(x, t) = 2 \arctan \left(\tan \left[\frac{x}{2} \right] \exp \left[-\frac{B}{\omega} \sin(\omega t) \right] \right). \quad (3.16)$$

Note that we have taken the initial time to be zero, as is done throughout this work.

3.5.2 Pulsating 2D solution

There is a simple extension of the 1D stationary wave solution to 2D. In this section we consider the velocity field $\mathbf{u} = [u, v]^T$ with components and velocity divergence given by

$$u(x, t) = B \sin(x) \cos(\omega t), \quad (3.17)$$

$$v(y, t) = B \sin(y) \cos(\omega t), \quad (3.18)$$

$$\nabla \cdot \mathbf{u} = B(\cos[x] + \cos[y]) \cos(\omega t), \quad (3.19)$$

where, again, B is a constant amplitude and ω is the compression frequency. The 2D continuity equation may then be written as

$$\frac{\partial q}{\partial t} + B \sin(x) \cos(\omega t) \frac{\partial q}{\partial x} + B \sin(y) \cos(\omega t) \frac{\partial q}{\partial y} + B(\cos[x] + \cos[y]) \cos(\omega t) = 0, \quad (3.20)$$

where, again, $q \equiv \ln \rho(\mathbf{x}, t)$.

The solution to (3.20) can be obtained by adding the solutions of the following two PDEs:

$$\frac{\partial q_1}{\partial t} + B \sin(x) \cos(\omega t) \frac{\partial q_1}{\partial x} + B \cos(x) \cos(\omega t) = 0, \quad (3.21)$$

$$\frac{\partial q_2}{\partial t} + B \sin(y) \cos(\omega t) \frac{\partial q_2}{\partial y} + B \cos(y) \cos(\omega t) = 0. \quad (3.22)$$

Thus, utilizing (3.15) and (3.16), and replacing $q_1(x_0[x, t], 0) + q_2(y_0[y, t], 0)$ with $q_0(x, y, t)$, we find that the solution to (3.20) is

$$\begin{aligned} q(x, y, t) &= q_0(x, y, t) \\ &+ \ln \left\{ \frac{1 + a(x_0[x, t]) \exp \left(\frac{2B}{\omega} \sin[\omega t] \right)}{1 + a(x_0[x, t])} \right\} \\ &+ \ln \left\{ \frac{1 + a(y_0[y, t]) \exp \left(\frac{2B}{\omega} \sin[\omega t] \right)}{1 + a(y_0[y, t])} \right\} \\ &- \frac{2B}{\omega} \sin(\omega t), \end{aligned} \quad (3.23)$$

where

$$a(z) \equiv \tan^2 \left(\frac{z}{2} \right), \quad (3.24)$$

and the initial positions are given by

$$x_0(x, t) = 2 \arctan \left(\tan \left[\frac{x}{2} \right] \exp \left[-\frac{B}{\omega} \sin(\omega t) \right] \right), \quad (3.25)$$

$$y_0(y, t) = 2 \arctan \left(\tan \left[\frac{y}{2} \right] \exp \left[-\frac{B}{\omega} \sin(\omega t) \right] \right). \quad (3.26)$$

Note that the initial condition $q_0(x, y, t)$ is restricted to cases where $\frac{\partial q_0}{\partial x}$ is independent of y and $\frac{\partial q_0}{\partial y}$ is independent of x . That is, the function q_0 must be *additively separable*.

An example of the solution to (3.23) is shown in Figure 3.11. The initial condition for the density is specified as $\rho(\mathbf{x}, 0) = 1$ and the amplitude and frequency are set to unity, $B = 1$ and $\omega = 1$. FDS is run with three scalar transport schemes: central differencing, Superbee, and the CHARM flux limiter. The solution at $(x, y) = (3\pi/2, 3\pi/2)$ for successively finer grid resolutions is plotted as a time series on the left and may be compared with the analytical solution (black line). On the right, we confirm second-order convergence for the FDS implementation. Central differencing and the CHARM limiter outperform Superbee for this problem because the solution is relatively smooth.

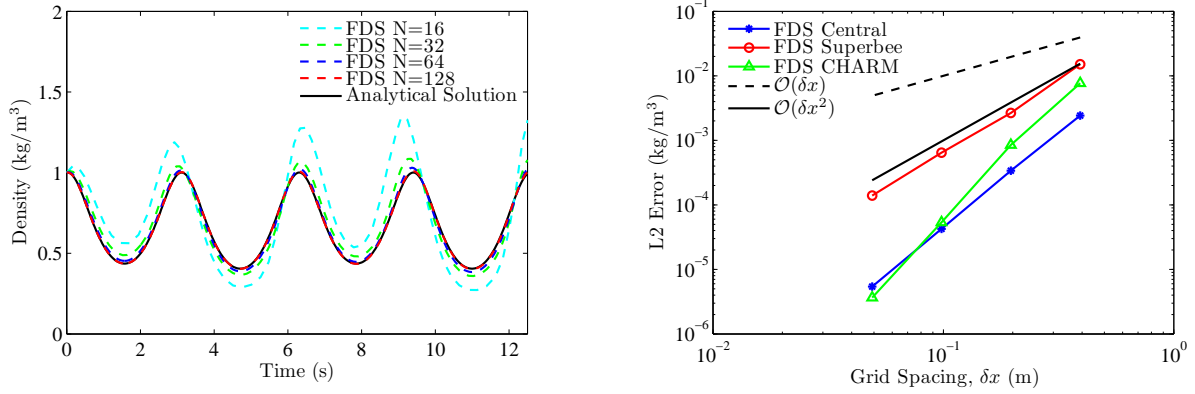


Figure 3.11: (Left) Time series of ρ at the position $(x, y) = (3\pi/2, 3\pi/2)$ for several grid resolutions using the Superbee limiter. (Right) Convergence plot for central differencing, Superbee, and CHARM. All schemes are second-order accurate.

3.5.3 Stationary compression wave in 1D

Another problem which can be solved analytically is that of a stationary compression wave. In this section we consider a stationary compression wave combined with a constant and uniform advection velocity in 1D. The velocity is specified to be

$$u(x) = c + \sin(x), \quad (3.27)$$

where $|c| > 1$ is a constant. The 1D continuity equation becomes

$$\frac{\partial q}{\partial t} + [c + \sin(x)] \frac{\partial q}{\partial x} + \cos(x) = 0. \quad (3.28)$$

A solution to (3.28) is

$$\begin{aligned} q(x, t) &= q(x_0[x, t], 0) \\ &+ \ln \left\{ -c^2 - \cos(bt + 2 \arctan[\gamma(x, t)]) + b \sin(bt + 2 \arctan[\gamma(x, t)]) \right\} \\ &- \ln \left\{ -c^2 - \cos(2 \arctan[\gamma(x, t)]) + b \sin(2 \arctan[\gamma(x, t)]) \right\}, \end{aligned} \quad (3.29)$$

where

$$b \equiv \sqrt{-1 + c^2} > 0, \quad (3.30)$$

$$\gamma(x, t) = \frac{1 + c \tan\left(\frac{x_0[x, t]}{2}\right)}{b}, \quad (3.31)$$

and

$$x_0(x, t) = 2 \arctan \left(\frac{b}{c} \tan \left[\arctan \left\{ \frac{1 + c \tan[x/2]}{b} \right\} - \frac{bt}{2} \right] - \frac{1}{c} \right). \quad (3.32)$$

3.5.4 Stationary compression wave in 2D

As with the pulsating flow, there is a simple extension of the 1D stationary wave solution to 2D. In this section we consider the velocity field with components

$$u(x) = c_1 + \sin(x), \quad (3.33)$$

$$v(y) = c_2 + \sin(y). \quad (3.34)$$

The continuity equation can be written as

$$\frac{\partial q}{\partial t} + [c_1 + \sin(x)] \frac{\partial q}{\partial x} + [c_2 + \sin(y)] \frac{\partial q}{\partial y} + \cos(x) + \cos(y) = 0. \quad (3.35)$$

A solution to (3.35) is

$$\begin{aligned} q(x, y, t) &= q_0(x, y, t) \\ &+ I_1(x, t) - I_1^0(x, t) \\ &+ I_2(y, t) - I_2^0(y, t), \end{aligned} \quad (3.36)$$

where

$$I_i(z, t) = \ln \left\{ -c_i^2 - \cos(b_i t + 2 \arctan[\gamma_i(z, t)]) + b_i \sin(b_i t + 2 \arctan[\gamma_i(z, t)]) \right\}, \quad (3.37)$$

$$I_i^0(z, t) = \ln \left\{ -c_i^2 - \cos(2 \arctan[\gamma_i(z, t)]) + b_i \sin(2 \arctan[\gamma_i(z, t)]) \right\}, \quad (3.38)$$

and

$$b_i \equiv \sqrt{-1 + c_i^2} > 0, \quad (3.39)$$

$$\gamma_i(z, t) = \frac{1 + c_i \tan\left(\frac{z_0[z, t]}{2}\right)}{b_i}, \quad (3.40)$$

$$z_0(z, t) = 2 \arctan \left(\frac{b_i}{c_i} \tan \left[\arctan \left\{ \frac{1 + c_i \tan[z/2]}{b_i} \right\} - \frac{b_i t}{2} \right] - \frac{1}{c_i} \right). \quad (3.41)$$

Note that $z_0 \Rightarrow x_0$ for $i = 1$ and $z_0 \Rightarrow y_0$ for $i = 2$. To be clear, no summation is implied over repeated indices. Also, note that the same restrictions apply to the initial condition as did in Section 3.5.2. Namely, that $\frac{\partial q_0}{\partial x}$ is independent of y and $\frac{\partial q_0}{\partial y}$ is independent of x .

An example of the solution to (3.36) is shown in Figure 3.12. In this case we set $c_1 = 2$ and $c_2 = 3$ to create an asymmetry in the flow. The periodicity in time depends on the choices of c_1 and c_2 ; it is possible that no periodicity exists. We have not found a case that generates a singularity. The analytical time series of the density at the position $(x, y) = (3\pi/2, 3\pi/2)$ is shown as the solid black line. FDS is run with the CHARM flux limiter scheme (as this is a DNS flow field). The solution at successively finer grid resolutions is plotted and compared with the analytical solution, demonstrating convergence of the scheme. On the right side of the figure we demonstrate second-order convergence of the central, Superbee, and CHARM limiter schemes in FDS.

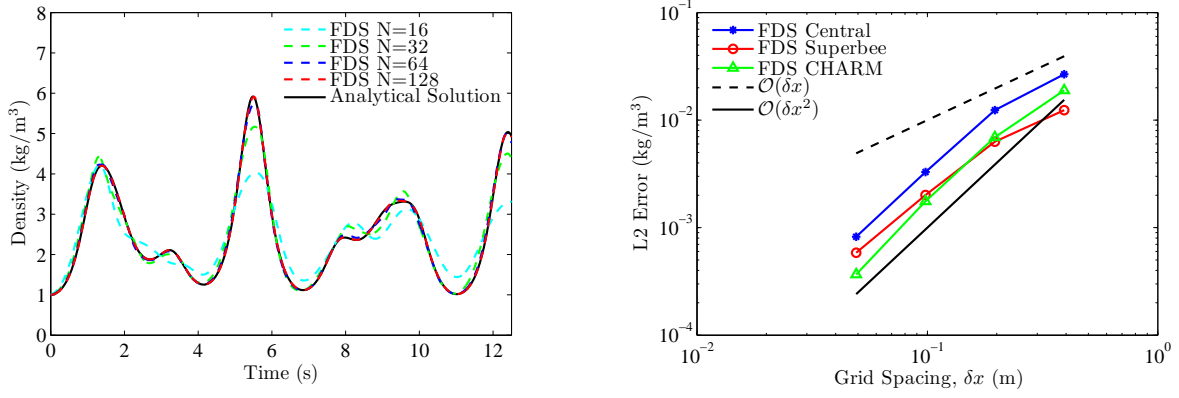


Figure 3.12: (Left) Time series of ρ at the position $(x,y) = (3\pi/2, 3\pi/2)$ for several grid resolutions using the CHARM flux limiter. (Right) Convergence plot for three different scalar transport schemes in FDS: central, Superbee, and CHARM. All schemes are second-order accurate. In addition, notice that Superbee gives the lowest error at the coarsest resolution while CHARM gives the lowest error at higher resolution. This is one reason why Superbee is recommended for LES and CHARM is the default for DNS.

3.6 Scalar Transport (move_slug)

In this section we demonstrate the qualitative behavior of the Superbee flux limiter scheme for transport of a square wave. The diffusivity is set to zero and the advecting velocity is constant and uniform $\mathbf{u} = [1.0 \ 1.0]$. The domain is the unit square with a passive scalar marker initialized to zero everywhere, except for two ‘slugs’ of mass. The first slug is set to unity over the region $x \times z = [0.125, 0.375] \times [0.125, 0.375]$. The second slug is set to 1/2 over the region $x \times z = [0.500, 0.750] \times [0.500, 0.750]$. With the scalar bounds set to $[0,1]$, these slugs demonstrate both the boundedness and TVD (total variation diminishing) behavior of the transport scheme.

This case also tests two different types of boundary conditions applied in FDS. First, the domain is periodic and the simulation runs for one flow through time. The scalar slugs therefore ideally arrive back to their original locations with as little diffusion as possible. Also, the domain is broken into four equally sized meshes, each with 40×40 uniform cells. To increase temporal accuracy and focus on the potential spacial error, we run the case with a CFL of 0.25. In FDS, we refer to the mesh interface as an ‘interpolated boundary’.

The results of the test are shown visually in Figure 3.13. The upper-left image shows the initial condition. The black lines indicate the mesh interfaces. To the right of the initial condition we show the first slug crossing the mesh interfaces without incurring spurious noise. The lower left image shows the final result for the Superbee limiter. By comparison with a first-order scheme (lower right), this test case confirms that relatively low levels of diffusion are incurred at both periodic and interpolated boundaries in FDS.

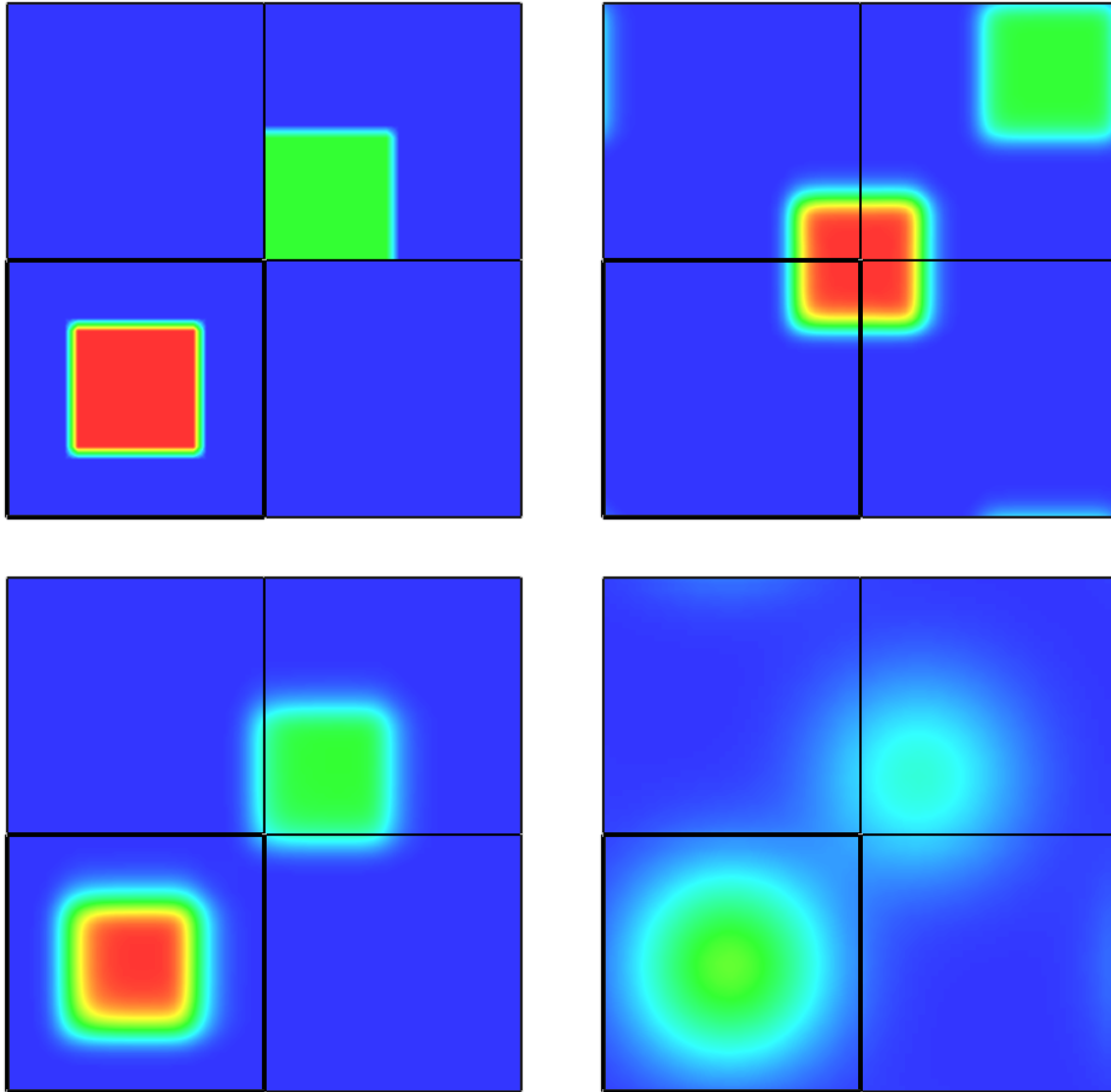


Figure 3.13: (Upper left) Initial condition. (Upper right) Superbee solution after 0.175 seconds showing the scalar slug cleanly passing through the mesh interface. (Lower left) Final result for Superbee after one flow through time. (Lower right) Result for first-order upwinding after one flow through time, illustrating the relatively low dissipation of the Superbee scheme. Note that, though the first-order scheme is available as an option in FDS, it is presented here for comparison purposes only. In practice, the higher order Superbee scheme is preferred for LES (FDS default).

3.7 Energy Conservation (energy_budget)

The examples in this section check that mass and energy are conserved for relatively simple configurations.

3.7.1 The Heat from a Fire (energy_budget)

For the purpose of verifying that the basic FDS algorithm is energy conserving, it is useful to think of a single compartment as a control volume into which energy is generated by a fire and out of which energy either flows via openings or is conducted through the walls. If the fire's heat release rate (HRR) is steady, eventually the system will reach a quasi-steady state (in an LES calculation, there is never a true "steady state"). Two simple cases, called **energy_budget_adiabatic_walls** and **energy_budget_cold_walls**, illustrate that in the quasi-steady state, the energy generated by the fire is conserved. For the case with adiabatic walls, a 1200 kW fire is simulated within a compartment that is 10 m by 10 m by 5 m tall. There is a single door and a single horizontal vent in the ceiling. The walls are assumed to be adiabatic; that is, there is no net heat flux through them. Another way to look at it is that the walls are perfect insulators. To simplify the case even further, the radiation transport algorithm is turned off. It is expected that in this case 1200 kW ought to flow out of the compartment either via the door or ceiling vent. The plot to the left side of Fig. 3.14 shows both the HRR and enthalpy flow out of the compartment converging to 1200 kW. During the warm up phase, the enthalpy flow is less than the HRR because energy is consumed heating up the air within the room.

Next, the same compartment with the same fire is now assumed to have cold (20 °C) walls, and the radiation is switched back on. After a few minutes of simulation, the net enthalpy outflow is approximately 470 kW and the heat losses to the wall (both radiative and convective) are approximately 730 kW. The plot is shown on the right hand side of Fig. 3.14.

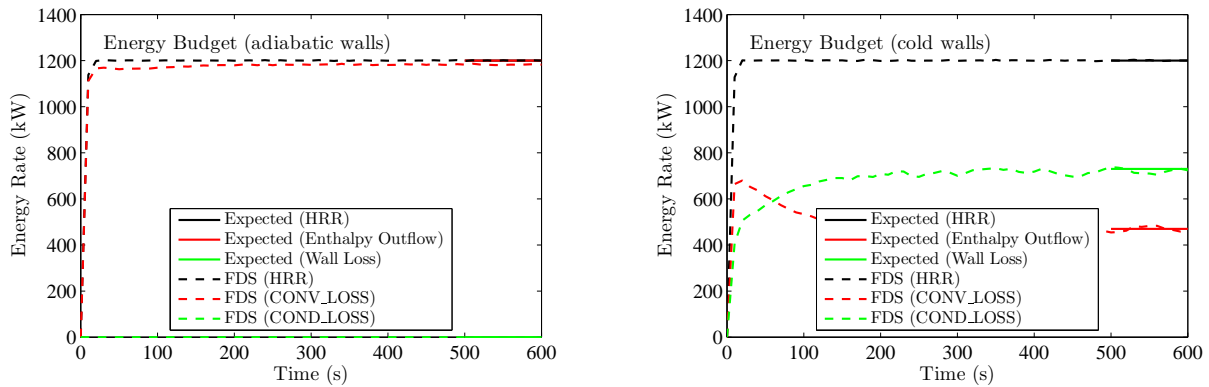


Figure 3.14: The Energy Budget for two simple compartment fire simulations.

3.7.2 Gas Injection via an Isentropic Process (isentropic)

This example checks that if nitrogen is added to a sealed compartment with adiabatic (*i.e.* no heat loss) walls, that the density, pressure and temperature ought to rise according to the ideal gas law for an isentropic process:

$$\frac{p_2}{p_1} = \left(\frac{\rho_2}{\rho_1} \right)^\gamma = \left(\frac{T_2}{T_1} \right)^{\frac{\gamma}{\gamma-1}} \quad (3.42)$$

The subscripts 2 and 1 refer to the final and initial state, respectively. Nitrogen is a diatomic gas for which $\gamma = 1.4$. As an additional check, the nitrogen is injected at two different rates such that in case A the injection occurs in 10 s and in case B the injection occurs in 50 s. The nitrogen is introduced into the domain via small spheres that do not generate or absorb heat. They do not occupy volume either. They just inject the nitrogen at a specified rate into the particular grid cell that each occupies.

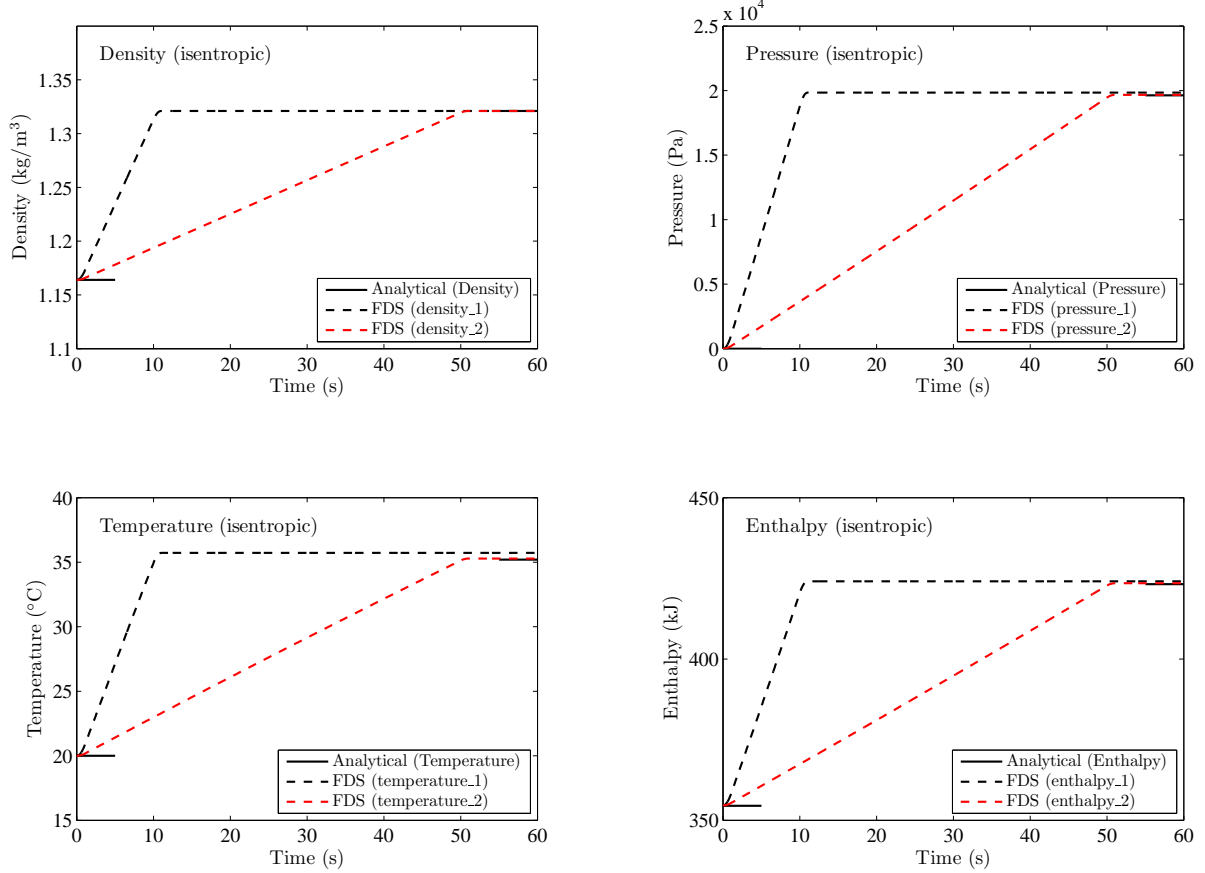


Figure 3.15: Density, pressure, temperature, and enthalpy rise due to the injection of nitrogen into a sealed compartment.

3.7.3 Gas Injection via a Non-Isentropic Process (isentropic2)

This example checks that if nitrogen is added via an external vent to a sealed compartment with adiabatic (*i.e.* no heat loss) walls, that the density, pressure and temperature ought to rise to the same values regardless of the time of injection. In the two cases, 0.2 kg of N_2 are added to a compartment that is 1 m³ in volume. In the first case, the injection occurs in 10 s, in the second case in 50 s. The temperature of the gas in both cases is 500 °C. It is expected that the pressure, p , should rise at the rate:

$$\frac{dp}{dt} = \frac{\gamma p u A}{V} \quad (3.43)$$

where u is the injection velocity and A is the area of the vent. The vent area is 0.04 m^2 . The density of the incoming N_2 is found from the Equation of State:

$$\rho = \frac{\bar{W} p}{\mathcal{R} T} \quad (3.44)$$

The injection velocity is the mass flux divided by the density, $u = \dot{m}''/\rho$, in which case, the pressure rise can be written

$$\frac{dp}{dt} = \frac{\gamma \dot{m}'' \mathcal{R} T A}{\bar{W} V} \quad (3.45)$$

Note that the pressure rise is constant. In both the fast and slow injection cases, the pressure is expected to rise 64282 Pa above ambient. The density and temperature rise are also linear. The density increases from 1.164 kg/m^3 to 1.364 kg/m^3 . The temperature increases from 20°C to 135.7°C . The change in the internal energy of the system, based on the mass and temperature of the added N_2 , is:

$$\Delta E = (0.2 \text{ kg}) \times (1.039 \text{ kJ/kg/K}) \times (773.15 \text{ K}) = 160.7 \text{ kJ} \quad (3.46)$$

Adding in the work due to the pressure yields the change in total enthalpy:

$$\Delta H = \Delta E + V \Delta P = 160.7 \text{ kJ} + (1 \text{ m}^3) \times (64.3 \text{ kJ/m}^3) = 225 \text{ kJ} \quad (3.47)$$

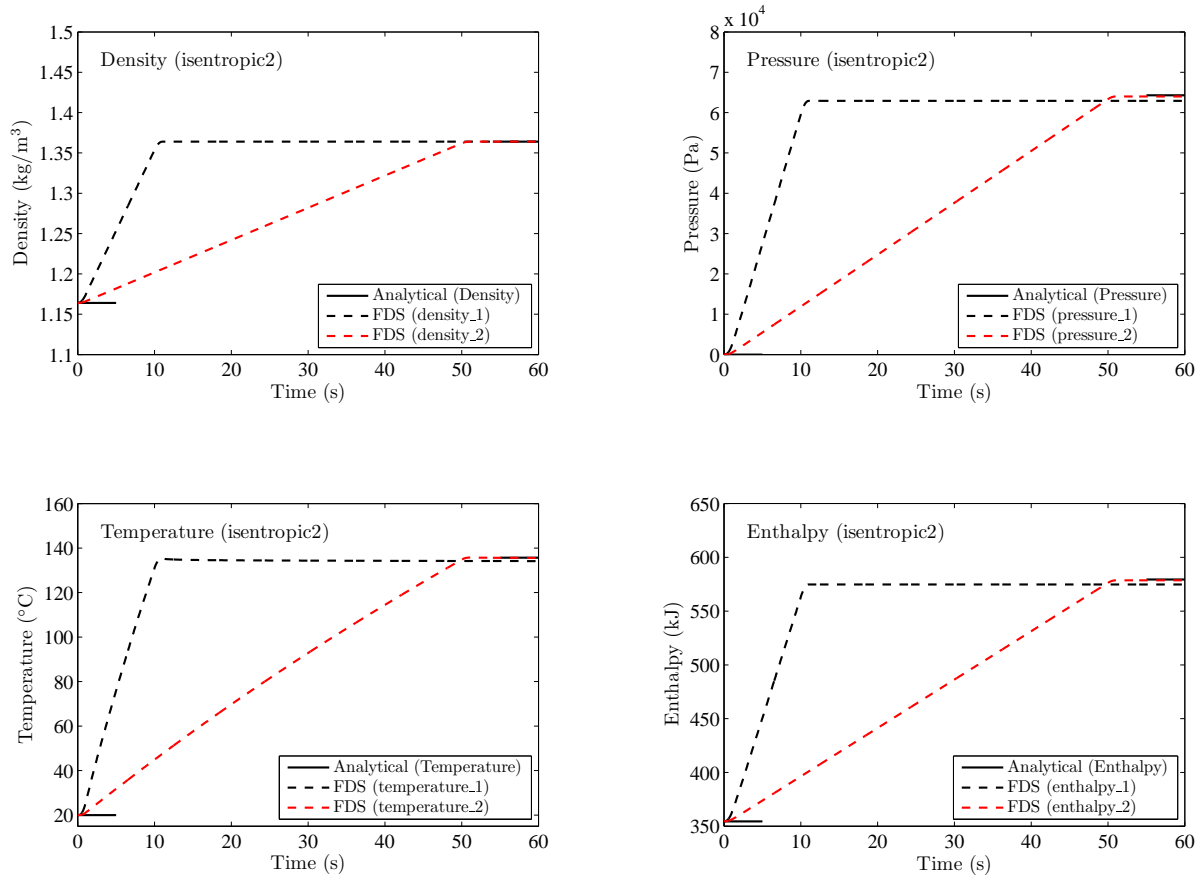


Figure 3.16: Density, pressure, temperature, and enthalpy rise due to the injection of nitrogen into a sealed compartment.

3.8 Checking for Coding Errors (symmetry_test)

This example is a very simple test to determine if there are coding errors in the basic flow solver. A closed box, 1 m on a side, has 6 injection vents, one centered on each face. Air is pumped into the box at a rate of 0.5 m/s. Anything that might lead to an asymmetry in the flow field is turned off, for example, gravity, atmospheric stratification, natural convection, and random noise. The resulting flow field is shown at the left in Fig. 3.17. On the right are plots of the three components of velocity at equidistant corners of the enclosure. Ideally, there should be two equal and opposite time histories of the three components. Even the slightest error in coding will throw this off almost immediately.

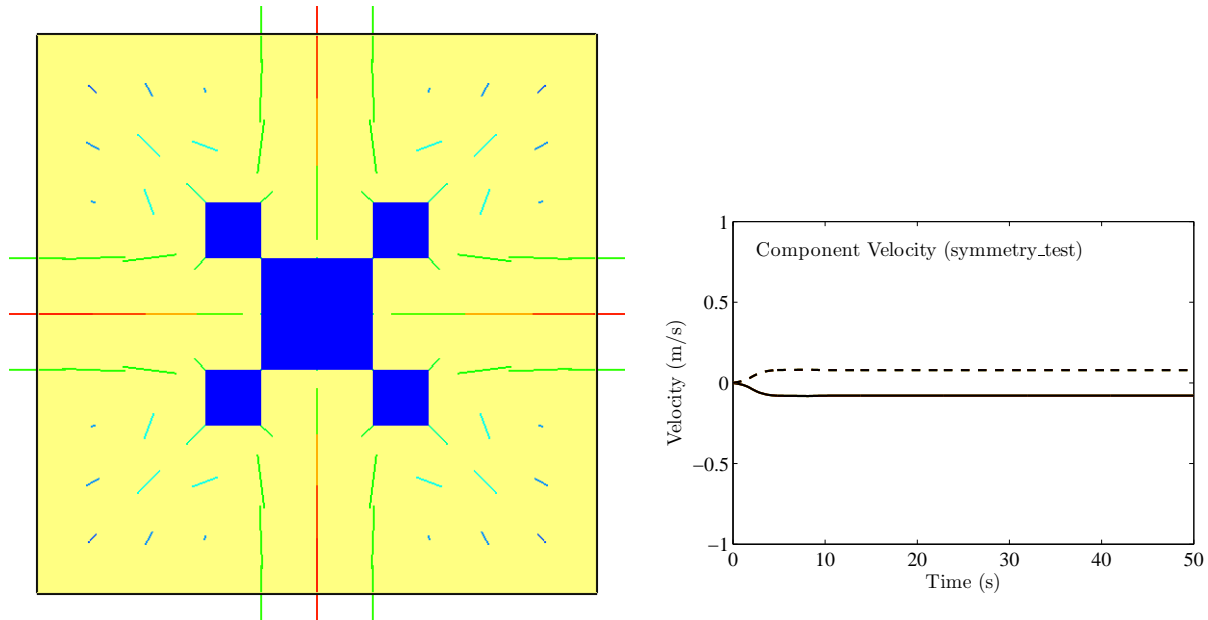


Figure 3.17: Flow field (left) and velocity component plot (right) for the symmetry_test case.

Chapter 4

Thermal Radiation

The Radiative Transport Equation (RTE) for an absorbing/emitting and scattering medium is

$$\mathbf{s} \cdot \nabla I_\lambda(\mathbf{x}, \mathbf{s}) = - \left[\kappa(\mathbf{x}, \lambda) + \sigma_s(\mathbf{x}, \lambda) \right] I_\lambda(\mathbf{x}, \mathbf{s}) + B(\mathbf{x}, \lambda) + \frac{\sigma_s(\mathbf{x}, \lambda)}{4\pi} \int_{4\pi} \Phi(\mathbf{s}, \mathbf{s}') I_\lambda(\mathbf{x}, \mathbf{s}') d\mathbf{s}' \quad (4.1)$$

where $I_\lambda(\mathbf{x}, \mathbf{s})$ is the radiation intensity at wavelength λ , \mathbf{s} is the direction vector of the intensity, $\kappa(\mathbf{x}, \lambda)$ and $\sigma_s(\mathbf{x}, \lambda)$ are the local absorption and scattering coefficients, respectively, and $B(\mathbf{x}, \lambda)$ is the emission source term. The integral on the right hand side describes the in-scattering from other directions. In the case of a non-scattering gas the RTE becomes

$$\mathbf{s} \cdot \nabla I_\lambda(\mathbf{x}, \mathbf{s}) = \kappa(\mathbf{x}, \lambda) \left[I_b(\mathbf{x}) - I_\lambda(\mathbf{x}, \mathbf{s}) \right] \quad (4.2)$$

where $I_b(\mathbf{x})$ is the source term given by the Planck function (see below).

In practical simulations the spectral (λ) dependence cannot be solved accurately. Instead, the radiation spectrum is divided into a relatively small number of bands and a separate RTE is derived for each band. The band specific RTE is

$$\mathbf{s} \cdot \nabla I_n(\mathbf{x}, \mathbf{s}) = \kappa_n(\mathbf{x}) \left[I_{b,n}(\mathbf{x}) - I_n(\mathbf{x}, \mathbf{s}) \right], \quad n = 1 \dots N \quad (4.3)$$

where I_n is the intensity integrated over the band n , and κ_n is the appropriate mean absorption coefficient inside the band. The source term can be written as a fraction of the blackbody radiation

$$I_{b,n} = F_n(\lambda_{\min}, \lambda_{\max}) \sigma T^4 / \pi \quad (4.4)$$

where σ is the Stefan-Boltzmann constant. The calculation of factors F_n is explained in Ref. [61]. When the intensities corresponding to the bands are known, the total intensity is calculated by summing over all the bands

$$I(\mathbf{x}, \mathbf{s}) = \sum_{n=1}^N I_n(\mathbf{x}, \mathbf{s}) \quad (4.5)$$

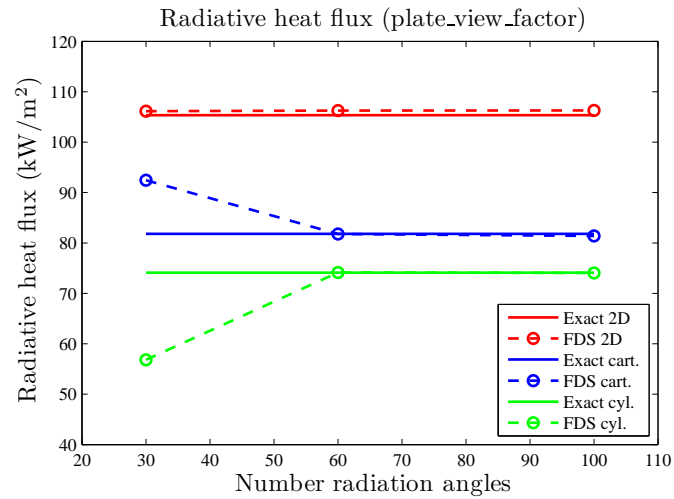
There are numerous examples in the heat transfer literature of exact solutions, for simple configurations of hot and cold objects, of the radiation transport equation.

4.1 Radiation from parallel plate in different co-ordinate systems (plate_view_factor)

This verification case tests the computation of radiative heat flux from hot surface to a differential, parallel surface at 1 m distance in different co-ordinate systems. The radiating surface is at 1000 °C temperature and has emissivity of 1.0. The exact values are calculated using the analytical expressions for the view factors.

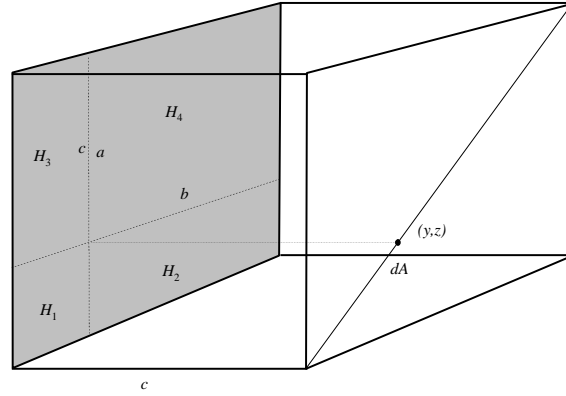
Co-ordinates	Radiation source	Heat flux (kW/m ²)
2D cartesian	Infinite plate of width 2 m	105.3
3D cartesian	Square plate of width 2 m	81.8
2D cylindrical	Circular disk of diameter 2 m	74.1

A comparison of exact values and FDS predictions at three different angular resolutions is shown below.



4.2 Radiation inside a box (radiation_in_a_box)

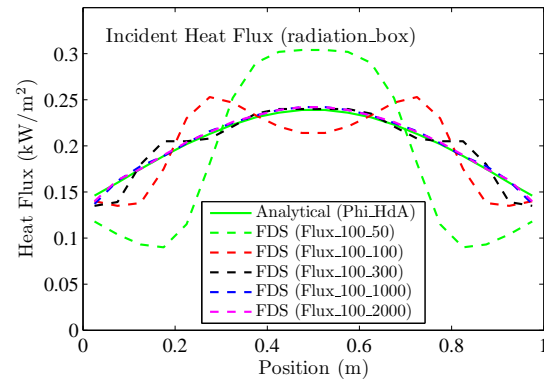
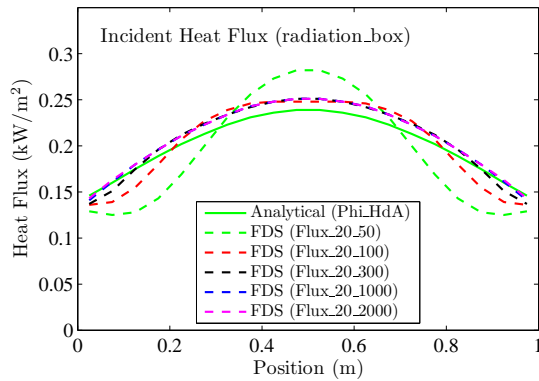
This verification case tests the computation of three-dimensional configuration factor Φ inside a cube box with one hot wall and five cold (0 K) walls. An overview of the test geometry is shown here:



The configuration factors are calculated at the diagonal of the cold wall opposite to the hot wall. The exact values of the configuration factor from plane element dA to parallel rectangle H are calculated using the analytical solution [61]

(y,z)	Φ_{HdA}	(y,z)	Φ_{HdA}
0.025	0.1457	0.275	0.2135
0.075	0.1603	0.325	0.2233
0.125	0.1748	0.375	0.2311
0.175	0.1888	0.425	0.2364
0.225	0.2018	0.475	0.2391

Different variations of the case include the mesh resolution (20^3 and 100^3 cells) and the number of radiation angles (50, 100, 300, 1000, 2000). The exact and FDS results are shown here:



4.3 Radiation from a plane layer (radiation_plane_layer)

This case tests the computation of three-dimensional radiation from a homogenous, infinitely wide layer of hot gases. The temperature of the layer is 1273.15 K and the absorption coefficient, κ , is varied. The thickness of the layer is fixed at 1 m, and the optical depth is $\tau = (1 \kappa) \text{ m}^{-1}$. Wall temperatures are set to 0 K. The results are compared against the exact solution $S(\tau)$ presented in [62]

$$S(\tau) = S_b [1 - 2E_3(\tau)] \quad (4.6)$$

where $S_b = \sigma T^4$ is the black-body heat flux from the radiating plane and $E_3(\tau)$ is the exponential integral function (order 3) of the optical depth τ .

The FDS results are computed at two mesh resolutions in the x -direction ($I=20$ and $I=150$). For $I=20$, both one-band and six-band versions are included to test the correct integration of heat fluxes over multiple bands. For $I=20$, 2-D versions are also computed ($J=1$). The limiting case, $\tau = \infty$, using a solid wall of temperature 1273.15 K, is computed to test the wall heat flux computation. The exact values and FDS predictions of the wall heat fluxes are given in the table below.

τ (m^{-1})	$S(\tau)$ (kW/m^2)	FDS ($I=20, J=20$)		FDS ($I=20, J=1$)		FDS ($I=150$)
		1 band	6 bands	1 band	6 bands	1 band
0.01	2.8970	2.9214	2.9104	2.8364	2.8257	2.9285
0.1	24.9403	25.5668	25.4705	25.1078	25.0133	25.7191
0.5	82.9457	83.1353	82.8224	84.3719	84.0542	84.0311
1.0	116.2891	115.4055	114.9710	117.8011	117.3576	116.7755
10	148.9698	148.9619	148.4011	148.9677	148.4069	148.9695
∞	148.9709	147.7533	147.1970	147.9426	147.3856	147.9419

4.4 Wall Internal Radiation (wall_internal_radiation)

In-depth absorption of thermal radiation in a solid is computed using a two-flux model. In this example, the accuracy of the two-flux model is tested in the computation of the emissive flux from a homogenous layer of material (thickness $L = 0.1$ m) at 1273.15 K temperature, surrounded by an ambient temperature of 10 K. The absorption coefficient κ is varied to cover a range $[0.01, 10]$ of optical depth $\tau = \kappa L$.

The exact solutions for radiative flux are the analytical solutions of plane layer emission [62]

$$S(\tau) = S_b [1 - 2E_3(\tau)] \quad (4.7)$$

where $S_b = \sigma T^4$ is the black-body heat flux from the radiating plane and $E_3(\tau)$ is the exponential integral function (order 3) of optical depth, τ . The exact solutions and FDS results are shown in the table below.

τ	$S(\tau)$ (kW/m ²)	FDS (kW/m ²)
0.01	2.897	2.950
0.1	24.94	26.98
0.5	82.95	93.90
1.0	116.3	128.4
10.	149.0	149.0

4.5 Radiation Emitted by Hot Spheres (hot_spheres)

This case tests the calculation of the radiation heat flux from a collection of hot objects. Within two completely open volumes that are 1 m on a side, hot spheres with a diameter of 1 cm and temperature of 500 °C are situated within a smaller volume that is 0.5 m on a side. One of the open volumes contains 10 spheres, the other contains 50,000. The simulation lasts for 10 s. In the first volume, the heat loss is just the sum of the areas of the spheres multiplied by σT^4 (emissivity is specified as unity in this case). See the upper left plot in Fig. 4.1. In the second volume, the region is densely packed and it is expected that the collection of spheres will radiate like a solid cube that is 0.5 m on a side and whose temperature is 500 °C. This is just under 30 kW, as shown in the upper right of Fig. 4.1. The plot in the lower left of Fig. 4.1 shows the incident heat flux to a gauge positioned at the center of the densely packed volume. It is expected that this gauge would register a heat flux of $\sigma T^4 = 20.26 \text{ kW/m}^2$. Finally, the plot in the lower right of Fig. 4.1 indicates the integrated intensity, $4\sigma T^4 = 81.04 \text{ kW/m}^2$.

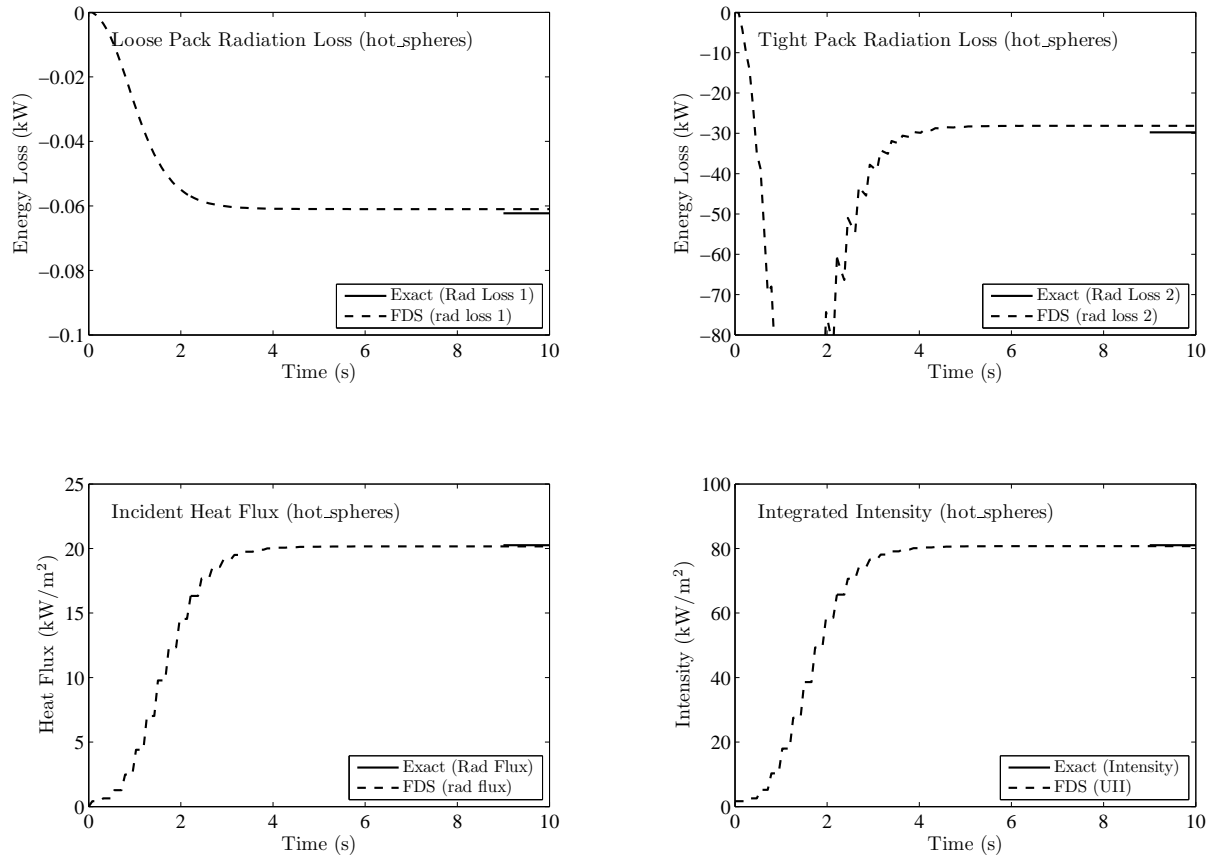


Figure 4.1: The total heat losses, radiative heat flux, and integrated intensity of a collection of loosely and densely packed radiating spheres.

4.6 Radiation Absorbed by Liquid Droplets (droplet_absorption)

This case tests the conservation of energy that is absorbed by liquid droplets. We want to make sure that the energy that is taken away from the thermal radiation field is accurately converted into increased temperature of the droplets. Considering the total mass of absorbing droplets, the average droplet temperature \bar{T}_d is increased by the absorbed radiation \dot{Q}_r according to the following ODE

$$mc_p \frac{d\bar{T}_d}{dt} = \dot{Q}_r \quad (4.8)$$

where m and c_p are the total mass and specific heat of the droplets, respectively. Here we have assumed that the convective heat transfer between the gas and droplets is small. (This is implemented by increasing the gas phase Prandtl number into a artificially high value.) If the absorbed power remains constant during the time step, the average droplet temperature in the end should be

$$\bar{T}_d = T_0 + dt \int \dot{Q}_r dV / (mc_p) \quad (4.9)$$

By setting $T_0 = 0^\circ\text{C}$, $dt = 0.01$ s, $m = 0.01$ kg and $c_p = 1.0$ kJ/kg, the value of \bar{T}_d should be equal to the volumetric integral of \dot{Q}_r . The following two plots show comparison of the predicted average droplet temperature and the analytical value in cartesian and cylindrical co-ordinate systems.

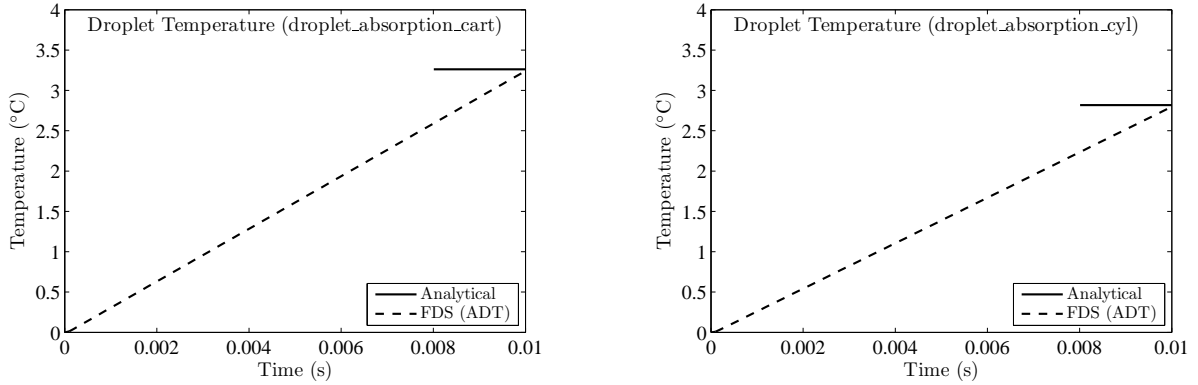


Figure 4.2: Conservation of absorbed thermal radiation energy into increased average droplet temperature.

Chapter 5

Species and Combustion

This chapter contains examples that test the computations related to species concentrations, gas properties and combustion.

5.1 Boundary Conditions

For most problems involving fire or combustion, *the* most important parameter of a model is the total heat release. It is therefore extremely important to assure that the correct amount of fuel is injected into the FDS computational domain. Below we present a series of test cases for the species boundary conditions.

5.1.1 Specified Mass Flux (low_flux_hot_gas_filling)

The specification of the fuel mass flux is probably the most commonly used boundary condition for specifying a fire. When the user specifies the `HRRPUA` (heat release rate per unit area), FDS divides this input by the heat of combustion for the specified fuel (propane by default) and uses this values as the specified mass flux \dot{m}''_{α} at the `VENT`. This seems simple enough. But the problem is complicated by the fact that the total species flux is the sum of the advective and diffusive fluxes,

$$\dot{m}''_{\alpha} = \rho Y_{\alpha} u_n - \rho D_{\alpha} \frac{\partial Y_{\alpha}}{\partial n} \quad (5.1)$$

where u_n is the face normal mass-average velocity and $\partial/\partial n$ is the gradient normal to the face. The velocity is determined from the total mass flux and the density at the face,

$$u_n = \frac{\sum_{\alpha} \dot{m}''_{\alpha}}{\rho(\mathbf{Y}, T)} \quad (5.2)$$

The density is computed using old values of the face mass fractions and the face temperature which may be specified or computed depending on choices made by the user. The new face mass fraction is then set to satisfy (5.1). The test case below is designed to exercise contributions from both the advective and diffusive terms in this boundary condition.

In the test case, we inject propane into a cube with 1 m² vents on all six faces. We specify the `MASS_FLUX` of propane to be 0.0001 kg/(m² s) and the temperature of the face of the `VENT` (`TMP_FRONT`) is specified to be 500 °C. The box is initially filled with air at standard conditions. We `DUMP` a `MASS_FILE` and compare the accumulation of propane with the specified rate. The results are shown in Figure 5.1.

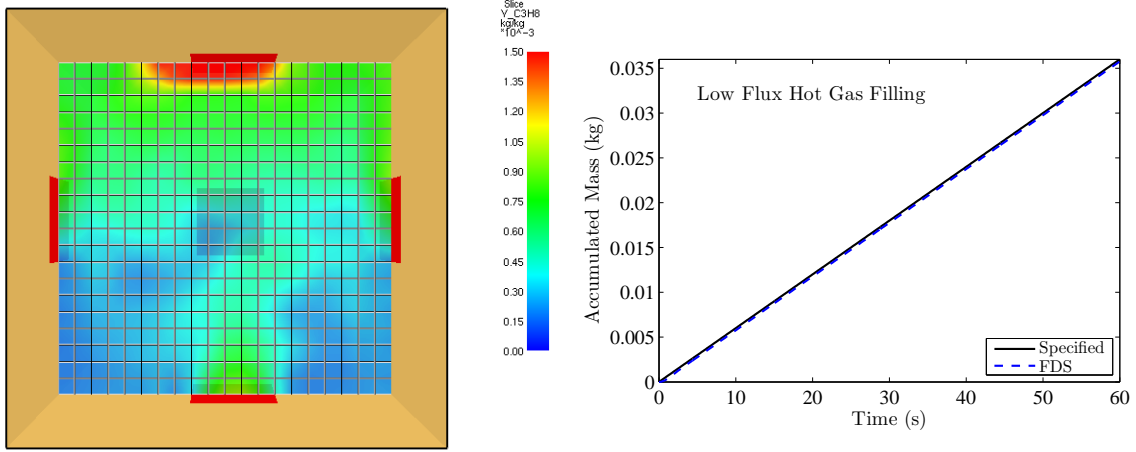


Figure 5.1: Test of specified mass flux boundary condition for low mass flux and specified temperature on the face of the VENT. (Left) Image of the domain showing contours of propane mass fraction. (Right) Comparison of the accumulated mass of propane with the FDS values reported in the `_mass` file.

5.2 Fractional Effective Dose (FED_Device)

The Fractional Effective Dose index (FED), developed by Purser [63], is a commonly used measure of human incapacitation due to the combustion gases. The present version of FDS uses only the concentrations of the gases CO, CO₂, and O₂ to calculate the FED value as

$$\text{FED}_{\text{tot}} = \text{FED}_{\text{CO}} \times \text{HV}_{\text{CO}_2} + \text{FED}_{\text{O}_2} \quad (5.3)$$

The fraction of an incapacitating dose of CO is calculated as

$$\text{FED}_{\text{CO}} = 4.607 \times 10^{-7} (C_{\text{CO}})^{1.036} t \quad (5.4)$$

where t is time in seconds and C_{CO} is the CO concentration (ppm). The fraction of an incapacitating dose of low O₂ hypoxia is calculated as

$$\text{FED}_{\text{O}_2} = \frac{t}{60 \exp[8.13 - 0.54(20.9 - C_{\text{O}_2})]} \quad (5.5)$$

where C_{O_2} is the O₂ concentration (volume per cent). The hyperventilation factor induced by carbon dioxide is calculated as

$$\text{HV}_{\text{CO}_2} = \frac{\exp(0.1930 C_{\text{CO}_2} + 2.0004)}{7.1} \quad (5.6)$$

where C_{CO_2} is the CO₂ concentration (percent).

The FED values were computed from specified constant gas concentrations using an external spreadsheet. The gas concentrations are listed in the following table and the FDS and spreadsheet predictions of FED values are compared in the figures below.

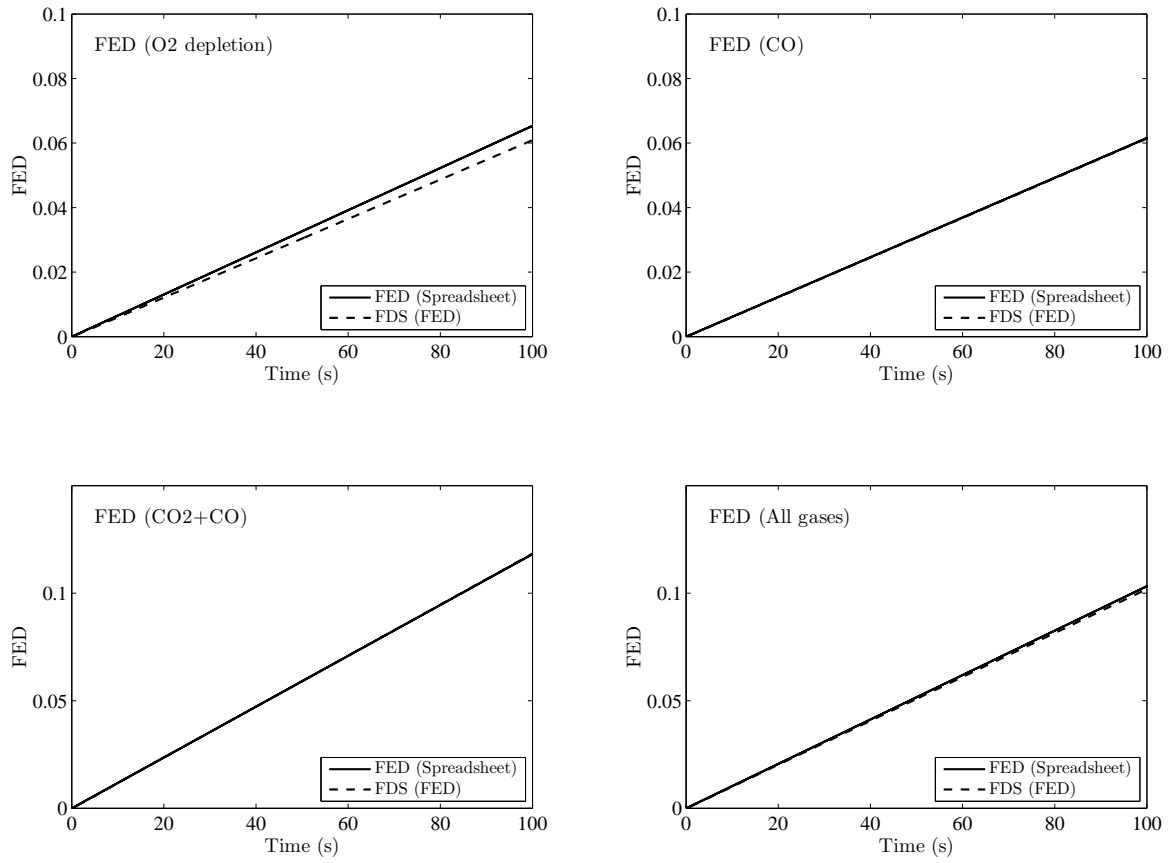


Figure 5.2: Comparison of FED index predictions with spreadsheet computations.

Chapter 6

Heat Conduction

This chapter contains examples that test the one-dimensional heat conduction solver in FDS. A one-dimensional heat conduction equation for the solid phase temperature $T_s(x, t)$ is applied in the direction x pointing into the solid (the point $x = 0$ represents the surface)

$$\rho_s c_s \frac{\partial T_s}{\partial t} = \frac{\partial}{\partial x} k_s \frac{\partial T_s}{\partial x} + \dot{q}_s''' \quad (6.1)$$

In cylindrical and spherical coordinates, the heat conduction equation is written

$$\rho_s c_s \frac{\partial T_s}{\partial t} = \frac{1}{r} \frac{\partial}{\partial r} \left(r k_s \frac{\partial T_s}{\partial r} \right) + \dot{q}_s''' \quad ; \quad \rho_s c_s \frac{\partial T_s}{\partial t} = \frac{1}{r^2} \frac{\partial}{\partial r} \left(r^2 k_s \frac{\partial T_s}{\partial r} \right) + \dot{q}_s''' \quad (6.2)$$

FDS offers the user these options, with the assumption that the obstruction is not actually recti-linear, but rather cylindrical or spherical in shape. This option is useful in describing the behavior of small, complicated “targets” like cables or heat detection devices.

6.1 Simple Heat Conduction Through a Solid Slab (heat_conduction)

Analytical solutions of transient, one-dimensional heat conduction through a slab can be found in Refs. [64] and [65]. Four cases are examined here. In each, a slab of thickness $L = 0.1$ m is exposed on one face to an air temperature of $T_g = 120$ °C. The other face is insulated (adiabatic). The convective heat transfer from the gas to the slab is $\dot{q}_c'' = h(T_g - T_s)$, where h is constant, and T_s is the slab face temperature. No thermal radiation is included.

Case	k (W/m/K)	ρ (kg/m ³)	c (kJ/kg/K)	h (W/m ² /K)	Bi hL/k
A	0.1	100	1	100	100
B	0.1	100	1	10	10
C	1.0	1000	1	10	1
D	10.0	10000	1	10	0.1

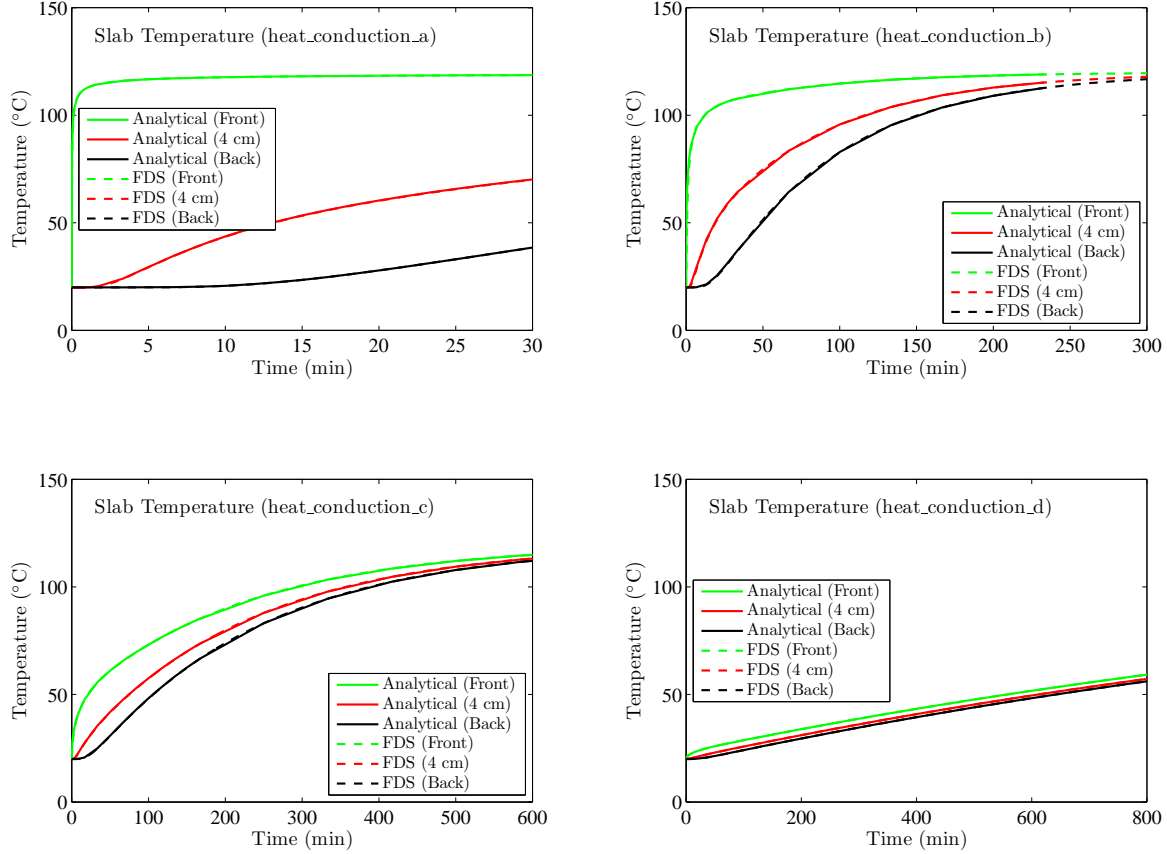


Figure 6.1: Comparison of heat conduction calculations with analytical solutions.

6.2 Temperature-Dependent Thermal Properties (heat_conduction_kc)

This example demonstrates the 1-D heat conduction in cartesian, cylindrical and spherical geometries with temperature-dependent thermal properties. The cartesian solution was computed using HEATING (version 7.3), a multi-dimensional, finite-difference, general purpose heat transfer model [66]. The cylindrical and spherical solutions were computed using a commercial finite-element solver, ABAQUS.

The sample of homogenous material is initially at 0 °C and at $t > 0$ exposed to a gas at 700 °C. A fixed heat transfer coefficient of 10 W/m²/K is assumed. The density of the material is 10000 kg/m³. The conductivity and specific heat are functions of temperature with the following values: $k(0) = 0.10$ W/m/K, $k(200) = 0.20$ W/m/K, $c(0) = 1.0$ kJ/kg/K, $c(100) = 1.2$ kJ/kg/K, $c(200) = 1.0$ kJ/kg/K. The thickness (radius) of the sample is 0.01 m. In the cartesian case, the back surface of the material is exposed to a gas at 0 °C. In the figure below, the light colored solid lines are FDS results and the dark lines are the HEATING results. An example input with cylindrical geometry looks like:

```
&MATL ID='MAT_1'
    EMISSIVITY = 0.0
    CONDUCTIVITY_RAMP='K_RAMP'
    SPECIFIC_HEAT_RAMP = 'C_RAMP'
    DENSITY=10000. /

&RAMP ID = 'K_RAMP' T=0,    F= 0.10 /
&RAMP ID = 'K_RAMP' T=100, F= 0.15 /
&RAMP ID = 'K_RAMP' T=200, F= 0.20 /
&RAMP ID = 'C_RAMP' T=0,    F= 1.00 /
&RAMP ID = 'C_RAMP' T=100, F= 1.20 /
&RAMP ID = 'C_RAMP' T=200, F= 1.00 /

&SURF ID='SLAB'
    STRETCH_FACTOR = 1.0
    GEOMETRY = 'CYLINDRICAL'
    MATL_ID='MAT_1'
    THICKNESS=0.01 /
```

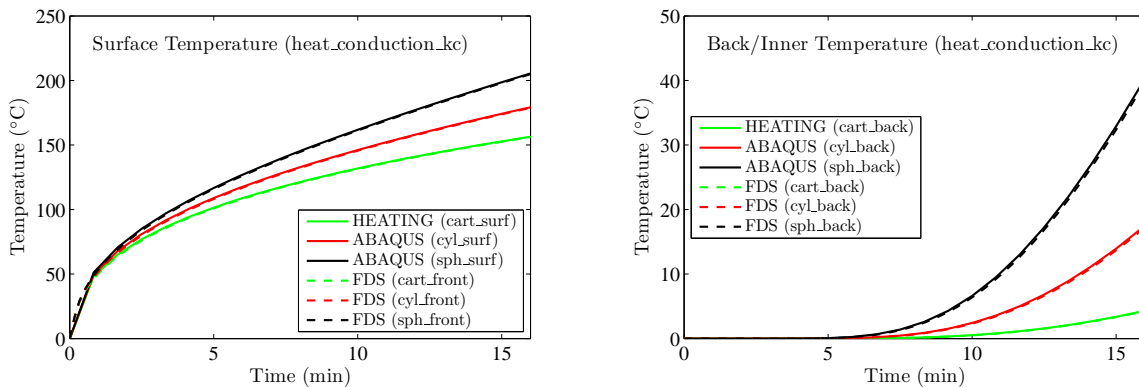


Figure 6.2: Comparison of heat conduction calculations with a finite-element model.

6.3 Simple Thermocouple Model (thermocouples)

This example tests the simple thermocouple model in FDS. It consists of a box whose walls and gas temperatures are fixed at 500 °C. Inside the box are three thermocouples with bead diameters of 1, 2, and 3 mm. Also included in the box are three “targets” – small solid objects whose surfaces are assumed to be composed of small spheres of the same diameter as the thermocouples. Figure 6.3 compares the temperature rise of the objects. The thermocouple model is not compared with an analytical solutions. This is simply a comparison of the thermally-thin thermocouple calculation with the thermally-thick “target” calculation. Small differences in temperature are due to slightly different flow conditions in different regions of the box, and numerical error due to node spacing and time step size.

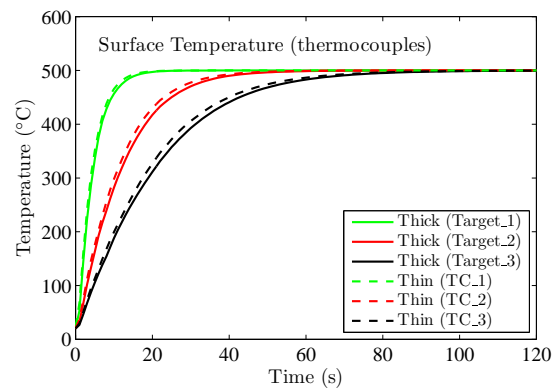


Figure 6.3: Comparison of thermally-thin and thick heat conduction into a small sphere.

Chapter 7

Pyrolysis

This chapter tests the routines in FDS that calculate the thermal decomposition of materials. Solid surfaces can consist of multiple layers, and each layer can consist of multiple material components. Each material component may undergo several competing reactions, and each of these reactions may produce some other solid component (residue), gaseous fuel, and/or water vapor.

7.1 Mass conservation of pyrolyzed mass (surf_mass_conservation)

The calculations described in this section check the conservation of mass produced by the pyrolysis algorithm. Parameters describing the geometric configuration of the solid are input via a `SURF` line, and the reacting materials are described on respective `MATL` lines. In the tests, four independent modeling options are varied:

1. The `SURF` line can be associated with either a solid surface as designated by a `VENT` line, or by solid particles as described by a `PART` line.
2. The `SURF` geometry can be either `CARTESIAN`, `CYLINDRICAL`, or `SPHERICAL`.
3. The `MATL` can be either charring (non-zero `NU_RESIDUE`) or non-charring.
4. The pyrolysis product can be either the fuel gas defined by the mixture fraction model, or an additional gas species, defined by a `SPEC` line.

In all cases, the wall thickness (or radius for cylindrical and spherical geometries) is 0.01 m. The material density is 360 kg/m^3 and the yield of gaseous products for the charring cases is 0.5, *i.e.* half of the original mass. For cartesian surfaces, the mass loss per unit area is 1.8 kg/m^2 for charring, and 3.6 kg/m^2 for non-charring materials. For cylindrical surfaces, the volume per unit surface area is $r/2$, and thus the mass loss per unit area is $360(1 - 0.5) \times r/2 = 0.9 \text{ kg/m}^2$ for charring, and 1.8 kg/m^2 for non-charring materials. For spherical surfaces, the volume per unit surface area is $r/3$, and thus the mass loss per unit area is $360(1 - 0.5) \times r/3 = 0.6 \text{ kg/m}^2$ for charring, and 1.2 kg/m^2 for non-charring materials. On the figures found on the following pages, the computed results are labeled as follows:

Expected indicates the total mass that has pyrolyzed by the end of the simulation.

Gaseous indicates the instantaneous concentration of pyrolyzed mass integrated over the volume of the computational domain. It should gradually increase from zero to the “Expected” value.

Solid indicates the instantaneous value of the solid surface density integrated over the entire surface area. For charring materials it should decrease from its initial value (twice the final value) to the final “Expected” value. For non-charring materials, it should decrease from the “Expected” value to zero.

Fuel Gas is the total burning rate integrated over time. It should increase from zero to the “Expected” value.

7.1.1 Pyrolysis at a Solid Surface

The analytical mass losses are calculated by multiplying the mass per unit area by the VENT area, which in all cases is 1 m². The expected and computed results for charring material are compared in 7.1. The expected and computed results for non-charring material are compared in 7.2.

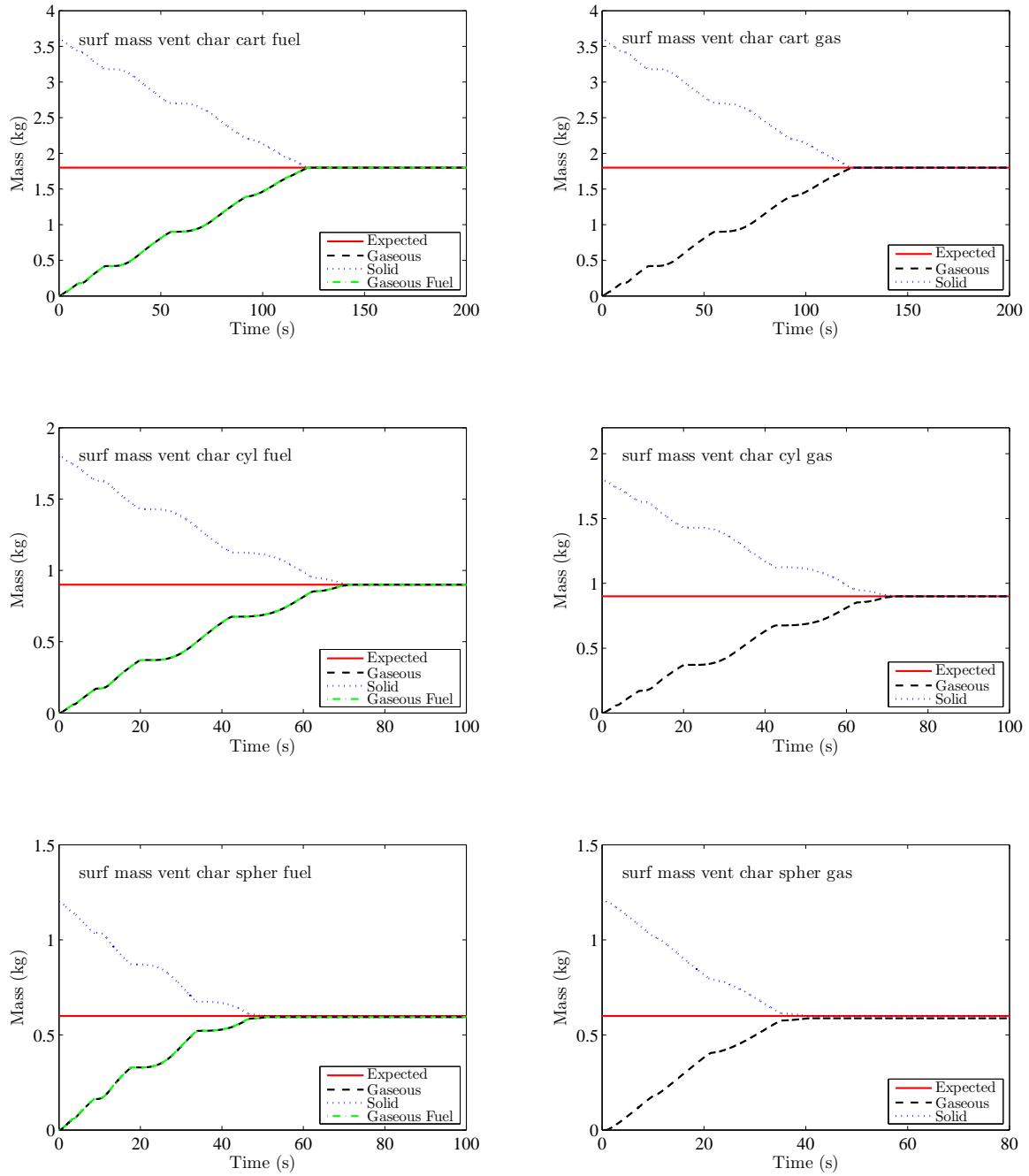


Figure 7.1: Comparison of analytical mass change and simulated mass changes for charring surfaces associated with vents.

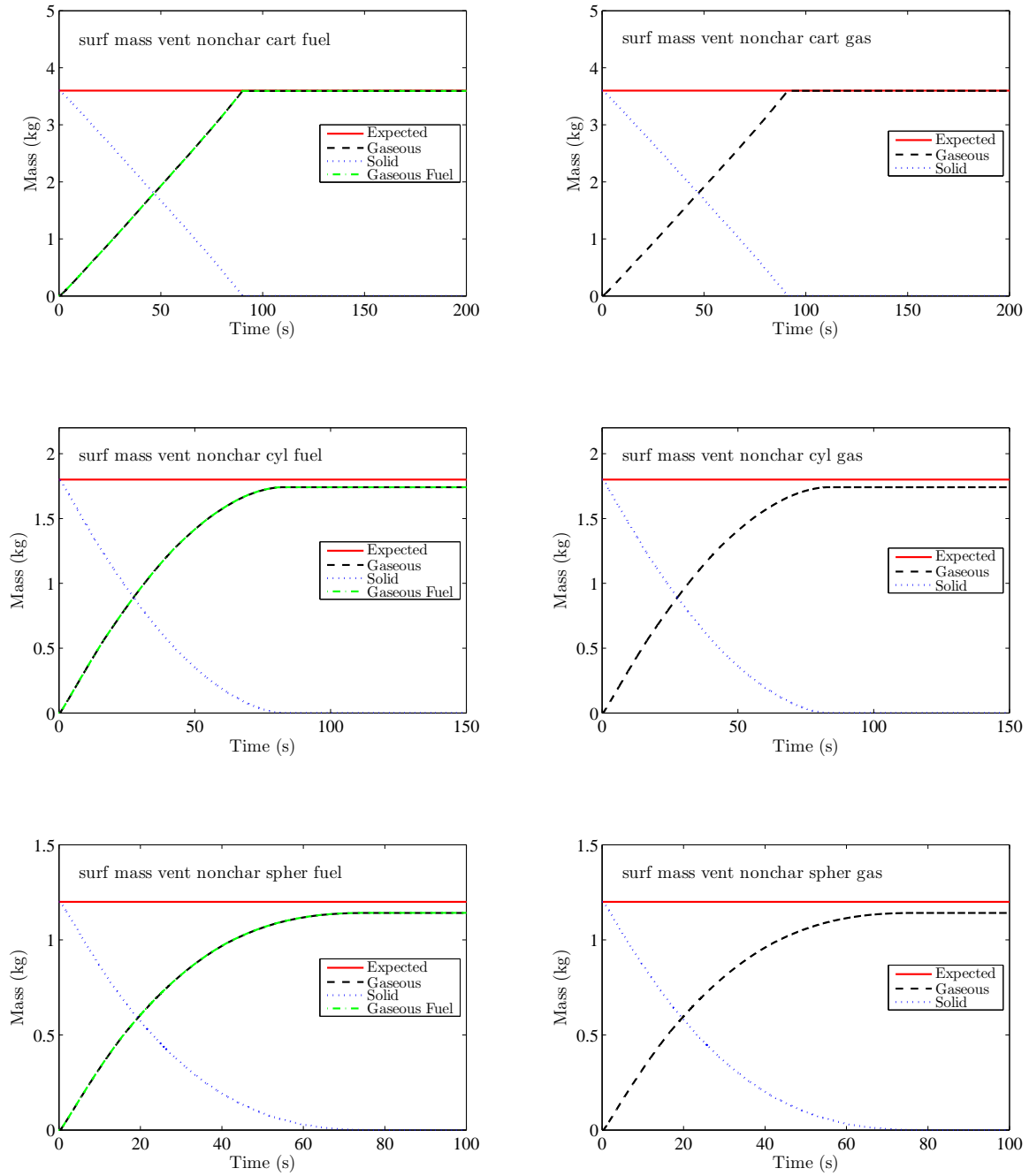


Figure 7.2: Comparison of analytical mass change and simulated mass changes for non-charring surfaces associated with vents.

7.1.2 Pyrolysis of Discrete Particles

For lagrangian particles, the expected values of the mass are obtained by multiplying the material density by the particle volume by the residue fraction. For cartesian surfaces, the particle area is two times the product of the parameters `LENGTH` and `WIDTH` on the `SURF` line, both of which are given a value 0.05 m. As a result, the expected masses for particles with cartesian surfaces are $360(1 - 0.5) \times 2\delta LW = 0.009$ kg for charring, and 0.018 kg for non-charring materials. Note that the half-thickness, $\delta = 0.01$ m, is specified on the `SURF` line as `THICKNESS`. For cylindrical particles, the `LENGTH` is 0.1 m, and the radius, r (specified via `THICKNESS`), is 0.01 m. The expected masses are thus $360(1 - 0.5) \times \pi r^2 L = 0.00565$ kg for charring, and 0.0113 kg for non-charring materials. For spherical particles, the expected mass is $360(1 - 0.5) \times 4\pi r^3 / 3 = 7.54 \times 10^{-4}$ kg for charring, and 1.51×10^{-3} kg for non-charring materials.

The analytical and computed results for charring material are compared in 7.3. The analytical and computed results for non-charring material are compared in 7.4.

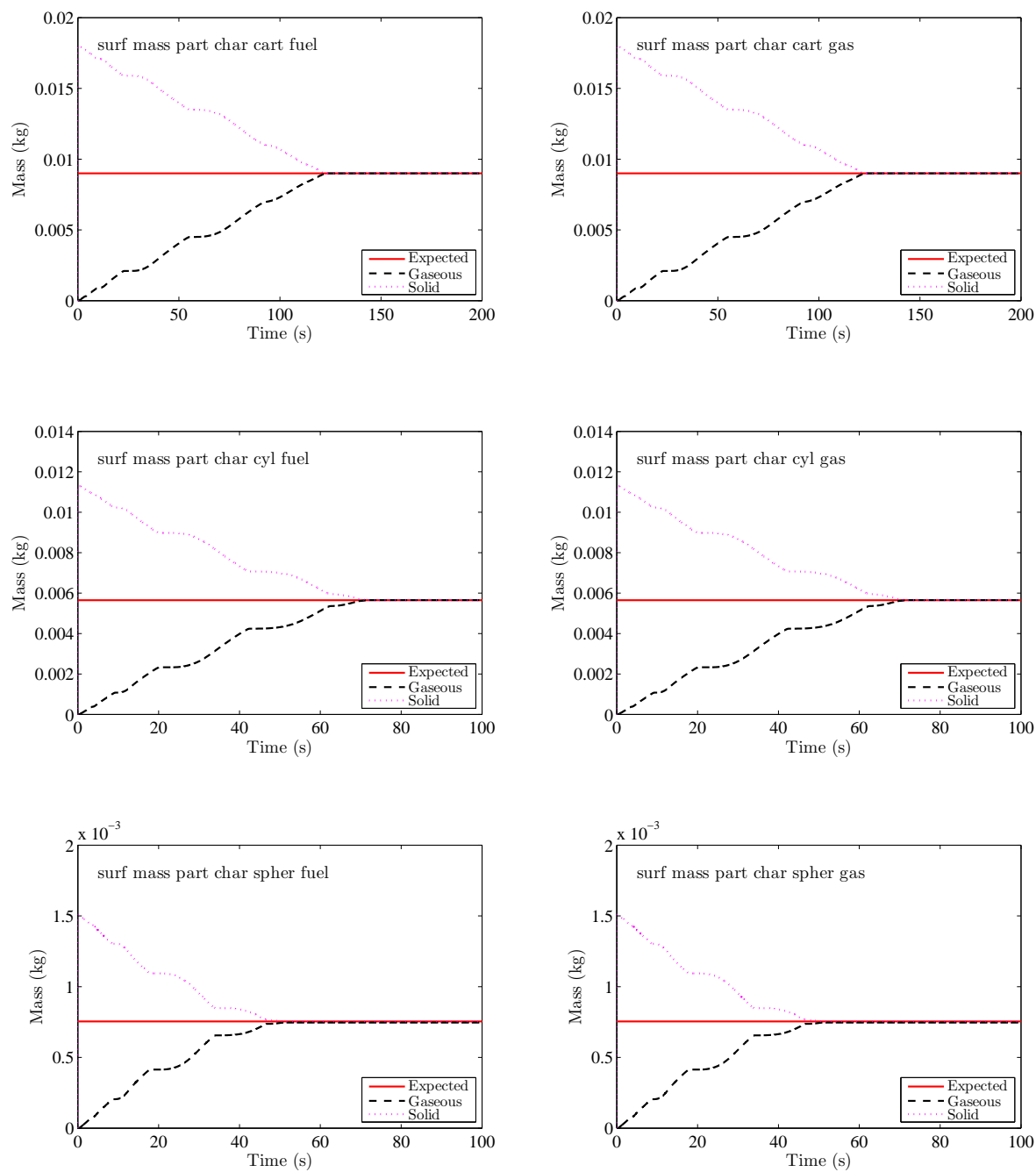


Figure 7.3: Comparison of analytical mass change and simulated mass changes for charring surfaces associated with particles.

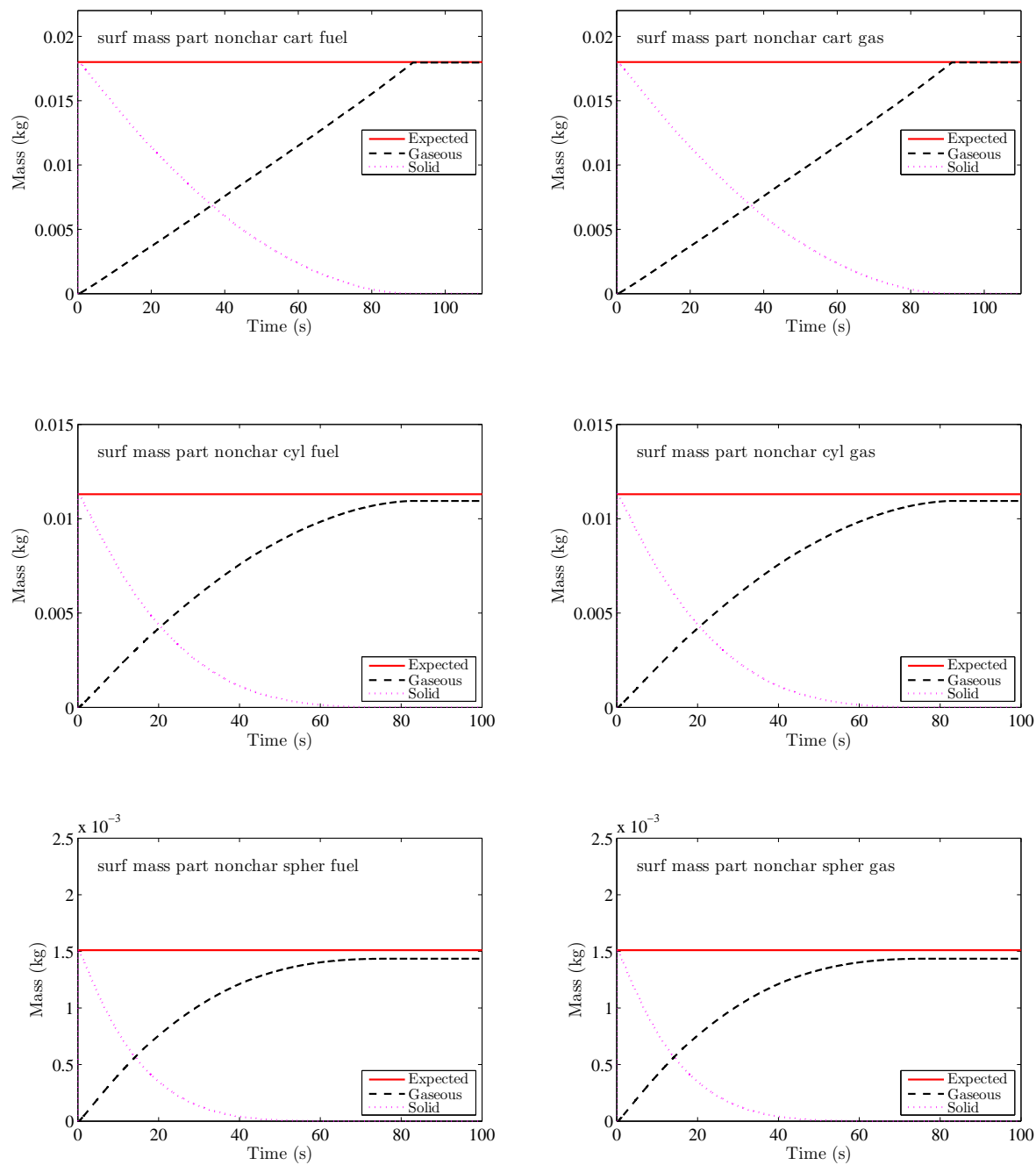


Figure 7.4: Comparison of analytical mass change and simulated mass changes for non-charring surfaces associated with particles.

7.2 Development of surface emissivity (emissivity)

For thermally thick materials, the surface emissivity is computed as a mass-weighted sum of the individual values of the emissivity in the first condensed phase grid cell. In this verification test, the initial material, having emissivity of 1.0, is converted to another material, having emissivity of 0.0, at a constant rate of 0.1 s^{-1} . As a result, the surface emissivity should change linearly from 1.0 to 0.0 in 10 s.

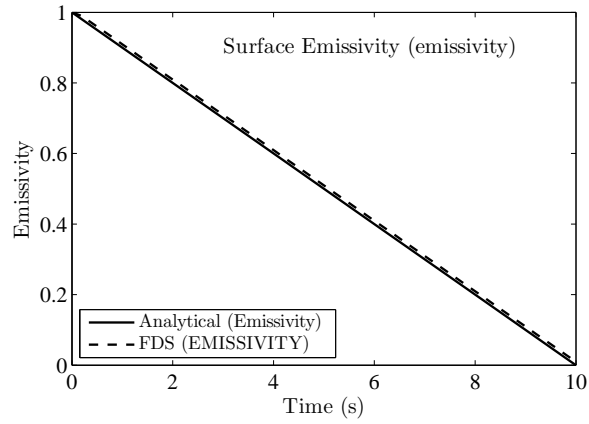


Figure 7.5: Testing the emissivity of solid materials.

7.3 Enthalpy of solid materials (enthalpy)

Consider a thin plate of conductive material that is exposed on one side to an elevated temperature heat source and exposed on the other to an ambient temperature void. In the thermally-thin limit, the temperature of the slab is governed by the following equation

$$\frac{dT_s}{dt} = \frac{\dot{q}_{\text{front}}'' + \dot{q}_{\text{back}}''}{c_s \rho_s \delta} \quad (7.1)$$

In this example, the initial exposure to the front side of the slab is 3 kW/m^2 . The original material (call it A) undergoes a reaction to form material B. The reaction rate is constant, 0.2 s^{-1} , which in this case means that material A disappears in exactly 5 s. This is achieved by setting n_s and E to 0 and A to 0.2 in the reaction rate term:

$$r = \left(\frac{\rho_{s,A}}{\rho_{s0}} \right)^{n_s} A \exp \left(-\frac{E}{RT_s} \right) \quad (7.2)$$

The density and conductivity of both materials are 30 kg/m^3 and 10 W/m/K , respectively. The emissivity of front and back is 1. The specific heat of material A changes from 1.0 kJ/kg/K to 0.1 kJ/kg/K above 80°C , while the specific heat of material B is constant at 1.0 kJ/kg/K . The slab is 1 mm thick.

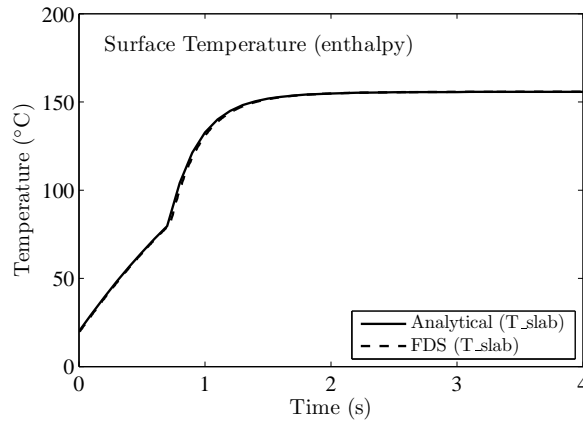


Figure 7.6: Testing the enthalpy of solid materials.

Note that the “analytical” solution is actually a simple numerical integration of the equations above with a small time step to ensure accuracy. This example tests a number of features, including the reaction rate, mass weighted specific heats, and radiation boundary conditions. Note that the convective heat transfer has been turned off, and the correct steady-state temperature is calculated by FDS.

7.4 A Simple Two-Step Pyrolysis Example (two_step_solid_reaction)

Before considering actual experimental measurements, it is necessary to check the accuracy of the ordinary differential equation solver within FDS. Consider the simplified set of ordinary differential equations describing the mass fraction of three components of a solid material undergoing thermal degradation:

$$\begin{aligned}\frac{dY_a}{dt} &= -K_{ab}Y_a \\ \frac{dY_b}{dt} &= K_{ab}Y_a - K_{bc}Y_b \\ \frac{dY_c}{dt} &= K_{bc}Y_b\end{aligned}\tag{7.3}$$

where the mass fraction of component a is 1 initially. The analytical solution is:

$$\begin{aligned}Y_a(t) &= \exp(-K_{ab}t) \\ Y_b(t) &= \frac{K_{ab}}{K_{bc} - K_{ab}} \exp(-K_{ab}t) - \exp(-K_{bc}t) \\ Y_c(t) &= [K_{ab}(1 - \exp(-K_{bc}t)) + K_{bc} * (\exp(-K_{ab}t) - 1)] / (K_{ab} - K_{bc})\end{aligned}\tag{7.4}$$

$$Y_c(t) = [K_{ab}(1 - \exp(-K_{bc}t)) + K_{bc} * (\exp(-K_{ab}t) - 1)] / (K_{ab} - K_{bc})\tag{7.5}$$

The analytical and numerical solution for the parameters $K_{ab} = 0.389$ and $K_{bc} = 0.262$ are shown here:

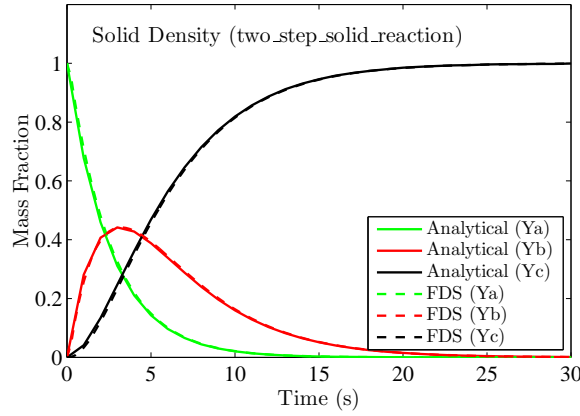


Figure 7.7: Comparison of a two-step solid pyrolysis calculation with an analytical solution.

7.5 Interpreting Bench-Scale Measurements

This section describes a method of deriving and applying the values of the kinetic parameters for the thermal decomposition of a solid, following the methodology described by Lyon [67].

7.5.1 General Theory

Consider a small sample of solid material that is heated at a relatively slow, constant rate. An example of this process is thermal gravimetric analysis (TGA). Assume that the solid consists of N material components, with each component mass fraction denoted by $Y_i(t)$. As the solid is heated, each component undergoes a reaction to form undetermined gases or a single solid residue whose mass fraction is denoted $Y_r(t)$ and whose yield is denoted by v_r . The governing equations for the component mass fractions is then:

$$\frac{dY_i}{dt} = -A_i Y_i \exp\left(-\frac{E_i}{RT}\right) \quad ; \quad Y_i(0) = Y_{0,i} \quad ; \quad i = 1, N \quad (7.6)$$

$$\frac{dY_r}{dt} = -v_r \sum_i \frac{dY_i}{dt} \quad ; \quad Y_r(0) = 0 \quad (7.7)$$

In the TGA apparatus, the temperature of the sample is increased linearly in time, $dT/dt = \beta$. Because TGA results are usually expressed as a function of temperature rather than time, it is convenient to rewrite Eq. (7.6) as:

$$\frac{dY_i}{dT} = -\frac{A_i}{\beta} Y_i \exp\left(-\frac{E_i}{RT}\right) \quad ; \quad Y(T = T_0) = Y_{0,i} \quad (7.8)$$

The decomposition rate, $-dY_i/dt$, peaks at a temperature denoted by $T_{p,i}$ with a value denoted by $r_{p,i}$. At this temperature, the second derivative of Y_i is zero:

$$\frac{d^2Y_i}{dT^2} = -\frac{A_i}{\beta} \frac{dY_i}{dT} \exp\left(-\frac{E_i}{RT_{p,i}}\right) - \frac{A_i}{\beta} Y_i \exp\left(-\frac{E_i}{RT_{p,i}}\right) \frac{E_i}{RT_{p,i}^2} = -\frac{dY_i}{dT} \left[\frac{A_i}{\beta} \exp\left(-\frac{E_i}{RT_{p,i}}\right) - \frac{E_i}{RT_{p,i}^2} \right] = 0 \quad (7.9)$$

Next, Eq. (7.8) can be integrated from $Y_{0,i}$ to $Y_{p,i}$ (the value of Y_i at the peak), and T_0 to $T_{p,i}$:

$$\int_{Y_{0,i}}^{Y_{p,i}} \left(\frac{dY_i'}{Y_i'} \right) = -\frac{A_i}{\beta} \int_{T_0}^{T_{p,i}} \exp\left(-\frac{E_i}{RT'}\right) dT' \approx -\frac{A_i R T_{p,i}^2}{\beta (E_i + 2RT_{p,i})} \exp\left(-\frac{E_i}{RT_{p,i}}\right) \quad (7.10)$$

Using Eq. (7.9) to eliminate A_i yields:

$$\ln\left(\frac{Y_{p,i}}{Y_{0,i}}\right) = -\frac{E_i}{E_i + 2RT_{p,i}} \approx -1 \quad (E_i \gg 2RT_{p,i}) \quad (7.11)$$

or more simply, $Y_{p,i} \approx Y_{0,i}/e$. Now, the activation energy can be evaluated using Eqs. (7.6) and (7.9):

$$E_i = RT_{p,i}^2 \frac{A_i}{\beta} \exp\left(-\frac{E_i}{RT_{p,i}}\right) = \frac{RT_{p,i}^2}{\beta} \frac{r_{p,i}}{Y_{p,i}} \approx \frac{RT_{p,i}^2}{\beta} \frac{e r_{p,i}}{Y_{0,i}} \quad (7.12)$$

Then A_i can be evaluated directly from Eq. (7.6):

$$A_i = \frac{r_{p,i}}{Y_{p,i}} \exp\left(\frac{E_i}{RT_{p,i}}\right) \approx \frac{e r_{p,i}}{Y_{0,i}} \exp\left(\frac{E_i}{RT_{p,i}}\right) \quad (7.13)$$

Note that the formulae for A_i and E_i can be evaluated with parameters that are obtained directly by inspection of the plot of mass loss rate versus temperature. For each peak, the values of $T_{p,i}$ and $r_{p,i}$ are obvious. The values of $Y_{0,i}$ can be estimated based on the relative area underneath each peak. The values of $Y_{0,i}$ should sum to 1.

7.5.2 Using Micro-Calorimetry Data (cable_11_mcc)

This section describes a method for interpreting micro-combustion calorimeter (MCC) measurements. The pyrolysis combustion flow calorimeter (PCFC), developed by Lyon and Walters [68] at the U.S. Federal Aviation Administration (FAA), is a device used to measure the heat generated from the combustion of small (4 mg to 6 mg) material samples by oxygen depletion calorimetry. Samples are pyrolyzed at a specified heating rate in an anerobic atmosphere (typically N₂) and the resulting gases are mixed with excess oxygen and combusted in a separate chamber. The heat release rate from the specimen is obtained from measurements of the concentration of oxygen in the effluent exiting the combustor as a function of time. The methodology is the basis for the standard test ASTM D 7309 [69].

The results of PCFC measurements for several multi-conductor control cables are shown in Fig. 7.8. For each cable, the insulation and jacket material were tested separately, and at least three replicates were performed for each (only one replicate is shown for each sample). The samples, weighing approximately 5 mg, were cut from the cable jackets and conductor insulation material of each of the cables. These samples were pyrolyzed in the PCFC at a rate of 1 K/s from 100 °C to 600 °C in a nitrogen atmosphere and the effluent combusted at 900 °C in a mixture consisting of 20 % O₂ and 80 % N₂. The resulting curve shows the heat release rate of the sample as it was heated, normalized by the mass of the original sample. There are usually one, two or three noticeable peaks in the curve, corresponding to temperatures where a significant decomposition reaction occurs. Each peak can be characterized by the maximum value of the heat release rate ($\dot{q}_{p,i}$), the temperature ($T_{p,i}$), and the relative fraction of the original sample mass that undergoes this particular reaction ($Y_{0,i}$). The area under the curve

$$\int_0^\infty \dot{q}(T) dT = \beta \Delta H' \quad (7.14)$$

is the sample heating rate (β) times the energy released per unit mass of the original sample ($\Delta H'$). This latter quantity is related to the more conventional heat of combustion via the relation

$$\Delta H = \frac{\Delta H'}{1 - v_r} \quad (7.15)$$

where v_r is the fraction of the original mass that remains as residue. Sometimes this is referred to as the “char yield.” Note that it is assumed to be the same for all reactions.

The MCC measurement is similar to TGA in that it is possible to derive the kinetic parameters, A_i and E_i , for the various reactions from the heat release rate curve. As an example of how to work with MCC data, consider the two plots shown in Fig. 7.8. The solid curves in the figures display the results of micro-calorimetry measurements for the insulation and jacket material of a multi-conductor control cable (the number 11 has no particular meaning other than to distinguish it from other cables being studied). The insulation material exhibits two fairly well-defined peaks, whereas the jacket material exhibits three. Thus, the insulation material is modeled using two solid components, each undergoing a single-step reaction that produces fuel gas and a solid residue. The jacket material is modeled using three solid components. The residue yield for the insulation material is 6 %; for the jacket 49 %, obtained simply by weighing the sample before and after the micro-calorimetry measurement. It is not known which reaction produces what fraction of the residue. Rather, it is assumed that each reaction yields the same residue in the same relative amount. The dashed curves in Fig. 7.8 are the results of FDS simulations of the MCC measurements. To mimic the sample heating, a very thin sheet comprised of a mixture of the solid components with an insulated backing is heated at the rate specified in the experiment (1 K/s or 60 K/min, the units needed in FDS). For each reaction, the kinetic parameters are calculated using the formulae (7.12) and (7.13). The values of $T_{p,i}$ are

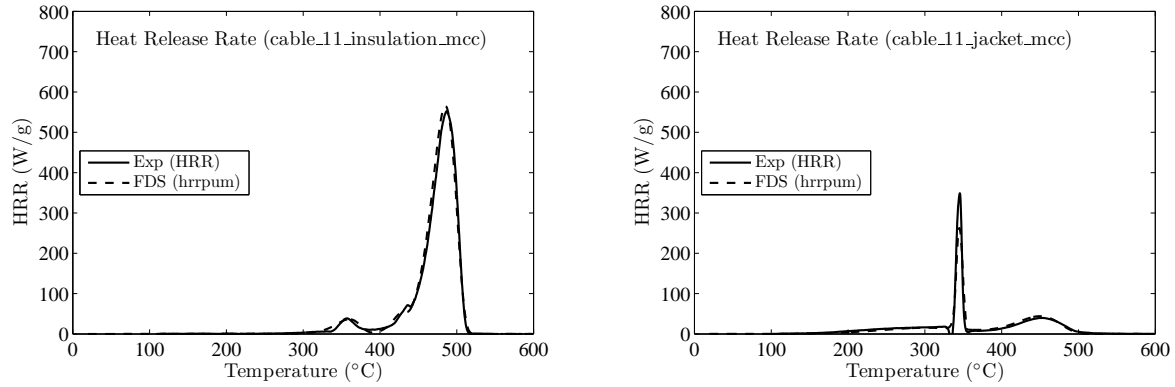


Figure 7.8: Results of a micro-calorimetry analysis of a sample of cable insulation (left) and jacket material (right).

obtained directly from the figures. The value of $r_{p,i}/Y_{0,i}$ for the i th reaction can be found from:

$$r_{p,i} = \beta \frac{\dot{q}_{p,i}}{\Delta H'} \quad ; \quad \Delta H' = \int_0^\infty \dot{q}(T) dT \quad (7.16)$$

where $\dot{q}_{p,i}$ is the value of the i th heat release rate peak. The values, $Y_{0,i}$, can be estimated from the relative area under the curve. Their sum ought to be 1. It is important to check the units of all of these quantities because the results of these experiments are often presented in different ways depending on the particular application. A mistake in units can result in values of A_i and/or E_i that will invariably cause spurious results.

The dashed curves in Fig. 7.8 are the results of numerically integrating Eq. (7.6) within FDS for each material component. A typical input line for FDS that describes a single material component undergoing a single reaction is given by:

```
&MATH ID = 'Cable 11 Jacket Component A'
EMISSION = ...
DENSITY = ...
CONDUCTIVITY = ...
SPECIFIC_HEAT = ...
N_REACTIONS = 1
REFERENCE_TEMPERATURE = 300.
REFERENCE_RATE = 0.0064
HEATING_RATE = 60.
NU_RESIDUE = 0.49
RESIDUE = 'char'
NU_FUEL = 0.51
HEAT_OF_REACTION = ... /
```

Only the relevant parameters are shown. The other parameters are not relevant in this exercise. Note that REFERENCE_TEMPERATURE is $T_{p,i}$, but in units of °C. REFERENCE_RATE is actually $r_{p,i}/Y_{0,i}$, in units of s^{-1} . HEATING_RATE is β in units of K/min. NU_RESIDUE is v_r and NU_FUEL is $(1 - v_r)$. Table 7.1 lists all of the kinetic parameters for the cable insulation and jacket materials. The peak temperatures are easy to estimate, and the values of $r_{p,i}/Y_{0,i}$ can be fine-tuned to closely match the data. Note that it is possible to compute values of A_i and E_i and input them directly into FDS, rather than inputting those listed in the table. However, the values of A_i and E_i are fairly large numbers and have little meaning in their own.

Table 7.1: Parameters used to derive the kinetic constants for cable materials. The heating rate for both is 60 °C/min.

Parameter	Insulation, $v_r=0.06$		Jacket, $v_r=0.49$		
	1	2	1	2	3
$T_{p,i}$ (°C)	355	485	300	345	450
$r_{p,i}/Y_{0,i}$ (s ⁻¹)	0.0384	0.2426	0.0064	0.3500	0.0156

7.5.3 Using TGA Data (birch_tga)

This is an example of a comparison of a candidate solid phase model with TGA (Thermo-gravimetric Analysis) data. The sample cases called **birch_tga_1step_2** and **birch_tga_1step_20** simulate two standard TGA experiments in which small samples of birch wood are heated up slowly at constant rates of 2 °C/min and 20 °C/min, respectively. The model of the wood only involves one reaction that converts virgin wood to char and fuel gases. There is also a reaction in the simulation that does nothing more than evaporate the small amount of moisture in the wood. This evaporation is evident in Fig. 7.9 near the temperature of 100 °C.

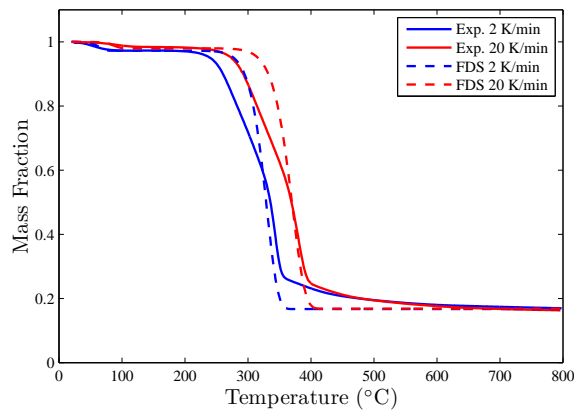


Figure 7.9: Comparison of a solid phase model of birch wood with TGA data.

Chapter 8

Lagrangian Particles

This chapter contains verification cases that test all aspects of particles, droplets, sprays, and so on. Note that in FDS, lagrangian particles are used for a variety of purposes, not just water droplets.

8.1 Momentum Transfer (particle_drag)

The particle drag test cases consider a 1 m by 1 m by 1 m channel with periodic boundary conditions on the x -faces and `FREE_SLIP` walls on y - and z -faces. Static droplets are placed in the center of the channel, one particle per computational cell, so that they form a surface perpendicular to the flow direction. Gravity is set to zero. Due to the symmetry of the problem the flow is one dimensional. Assuming that the droplets are of uniform diameter and the drag coefficient and gas density are constant, the velocity in the channel decays according to

$$u = \frac{u_0}{1 + B u_0 t} \quad ; \quad B = \frac{1}{2} \frac{\sum C_D \pi r_d^2}{V} \quad (8.1)$$

In the above, V is the volume of the channel, r_d is the droplet radius, C_D is the droplet drag coefficient, and u is the gas velocity in the x -direction. The summation is over all N particles. The common parameters used in all the simulations are

$$C_D = 10, \quad r_d = 0.005$$

The initial velocity, u_0 , for each case is listed in Table 8.1. Comparisons of computed and analytical results are shown in Figure 8.1.

Table 8.1: Parameters used in the **particle_drag** cases

Case	u_0	N
A	10	16
B	50	16
C	100	16
D	50	1600
E	100	1600
F	150	1600

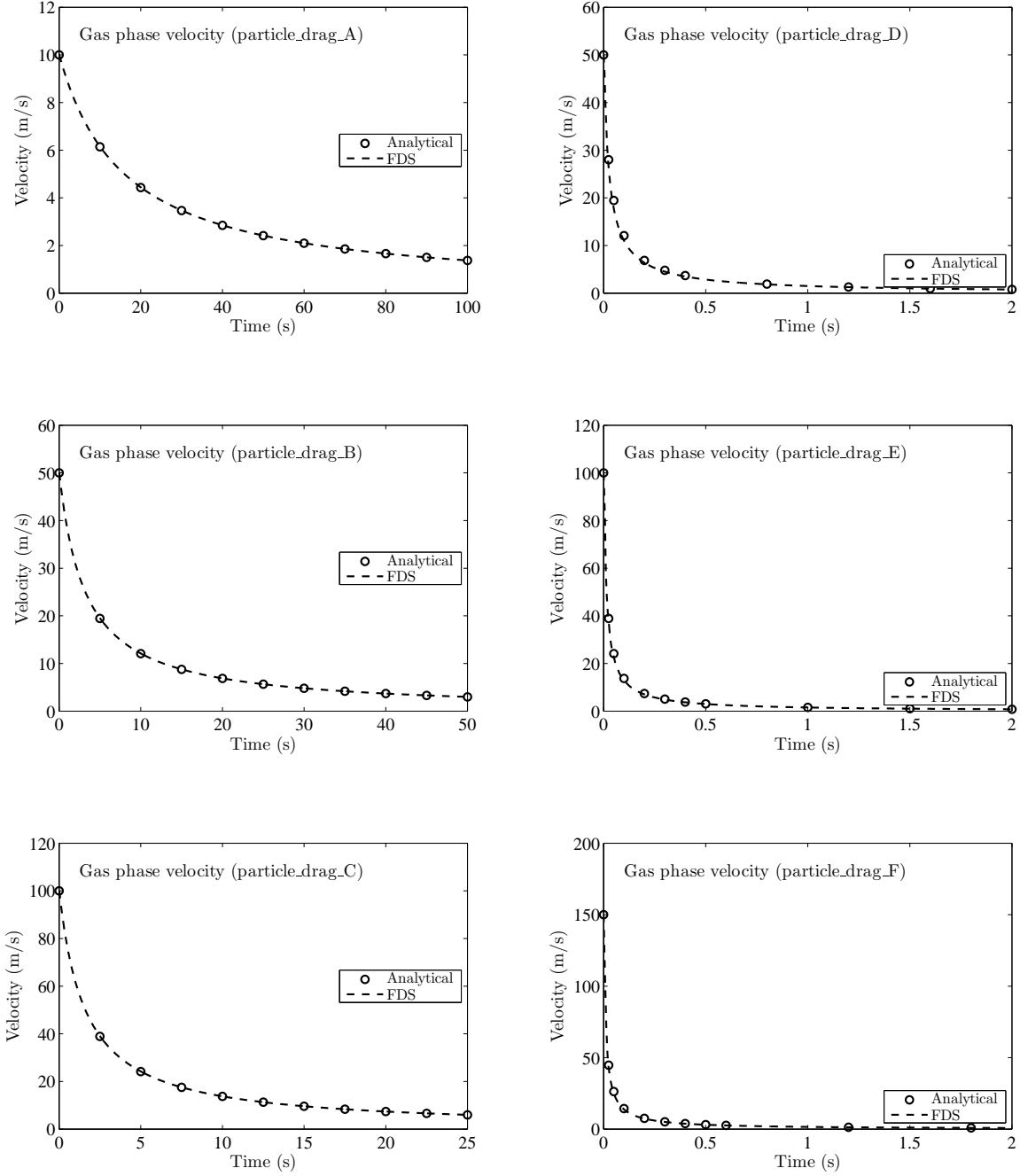


Figure 8.1: Outputs of the **particle_drag** test cases compared with analytical solutions.

8.2 Water Droplet Evaporation (water_evaporation)

The test case called **water_evaporation** involves stationary water droplets in a box with dimensions of 1 m on a side. The walls of the box are assumed adiabatic, meaning that there are no leaks or heat losses. The air within the box is stirred to maintain uniform conditions. Initially, the air temperature is 20 °C, the median volumetric diameter of the droplets is 100 μm , the water temperature is 90 °C, and the total mass of water droplets is 0.2 kg. It is expected that a steady-state will be achieved after about 5 s. Figure 8.2 displays the average enthalpy, humidity, density, pressure, temperature and mass of water of the gas. The horizontal lines denote the expected initial and steady-state values, respectively. The plot of enthalpy includes the gas (reference temperature is 0 K) and the liquid water droplets (reference temperature is 0 °C). The decrease in the enthalpy of the water droplets should equal the increase in the enthalpy of the gas minus the work performed due to increasing pressure. It is the internal energy of the system that is conserved. The internal energy can be expressed in terms of the enthalpy, pressure and density:

$$e = h - \frac{p}{\rho} \quad (8.2)$$

In differential form:

$$de = dh - \frac{1}{\rho} dp - p d\left(\frac{1}{\rho}\right) = dh - v dp - p dv \quad (8.3)$$

Multiplying by mass and noting that the volume, V , is constant yields:

$$dE = dH - V dp \quad (8.4)$$

The enthalpy decrease of the liquid water droplets is equal to the enthalpy gain of the gas (both expressed in kJ) minus the pressure increase times the volume in units of kPa and m^3 , respectively. Finally, note that in this example that a water droplet will evaporate until the vapor pressure at the droplet surface is in equilibrium with the vapor pressure in the surrounding air. Thus, the relative humidity should be equal to 100 %, but since FDS does not currently compute condensation, a slight overshoot is not unexpected.

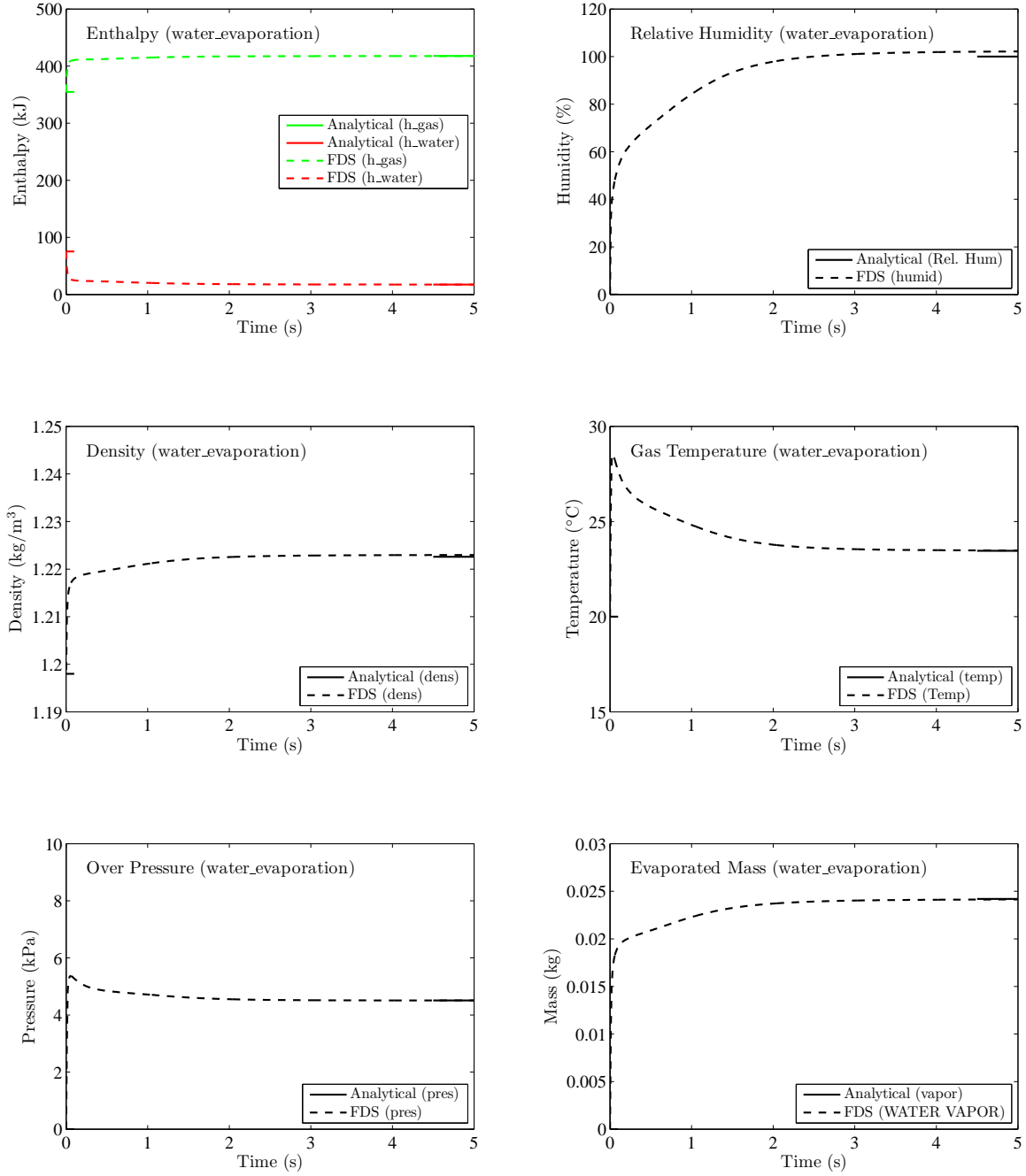


Figure 8.2: Output of the test case called **water_evaporation**.

Bibliography

- [1] K.B. McGrattan, S. Hostikka, and J.E. Floyd. Fire Dynamics Simulator (Version 5), User's Guide. NIST Special Publication 1019-5, National Institute of Standards and Technology, Gaithersburg, Maryland, October 2007. [i](#)
- [2] American Society for Testing and Materials, West Conshohocken, Pennsylvania. *ASTM E 1355-04, Standard Guide for Evaluating the Predictive Capabilities of Deterministic Fire Models*, 2004. [i](#), [1](#), [9](#)
- [3] W. Mell, K.B. McGrattan, and H. Baum. Numerical Simulation of Combustion in Fire Plumes. In *Twenty-Sixth Symposium (International) on Combustion*, pages 1523–1530. Combustion Institute, Pittsburgh, Pennsylvania, 1996. [3](#)
- [4] K.B. McGrattan, H.R. Baum, and R.G. Rehm. Large Eddy Simulations of Smoke Movement. *Fire Safety Journal*, 30:161–178, 1998. [3](#)
- [5] H.R. Baum, R.G. Rehm, P.D. Barnett, and D.M. Corley. Finite Difference Calculations of Buoyant Convection in an Enclosure, Part I: The Basic Algorithm. *SIAM Journal of Scientific and Statistical Computing*, 4(1):117–135, March 1983. [3](#)
- [6] H.R. Baum and R.G. Rehm. Finite Difference Solutions for Internal Waves in Enclosures. *SIAM Journal of Scientific and Statistical Computing*, 5(4):958–977, December 1984. [3](#)
- [7] H.R. Baum and R.G. Rehm. Calculations of Three Dimensional Buoyant Plumes in Enclosures. *Combustion Science and Technology*, 40:55–77, 1984. [3](#)
- [8] R.G. Rehm, P.D. Barnett, H.R. Baum, and D.M. Corley. Finite Difference Calculations of Buoyant Convection in an Enclosure: Verification of the Nonlinear Algorithm. *Applied Numerical Mathematics*, 1:515–529, 1985. [3](#)
- [9] K.B. McGrattan, T. Kashiwagi, H.R. Baum, and S.L. Olson. Effects of Ignition and Wind on the Transition to Flame Spread in a Microgravity Environment. *Combustion and Flame*, 106:377–391, 1996. [4](#)
- [10] T. Kashiwagi, K.B. McGrattan, S.L. Olson, O. Fujita, M. Kikuchi, and K. Ito. Effects of Slow Wind on Localized Radiative Ignition and Transition to Flame Spread in Microgravity. In *Twenty-Sixth Symposium (International) on Combustion*, pages 1345–1352. Combustion Institute, Pittsburgh, Pennsylvania, 1996. [4](#)
- [11] W. Mell and T. Kashiwagi. Dimensional Effects on the Transition from Ignition to Flame Spread in Microgravity. In *Twenty-Seventh Symposium (International) on Combustion*, pages 2635–2641. Combustion Institute, Pittsburgh, Pennsylvania, 1998. [4](#)

- [12] W. Mell, S.L. Olson, and T. Kashiwagi. Flame Spread Along Free Edges of Thermally-Thin Samples in Microgravity. In *Twenty-Eighth Symposium (International) on Combustion*, pages 2843–2849. Combustion Institute, Pittsburgh, Pennsylvania, 2000. 4
- [13] K. Prasad, Y. Nakamura, S.L. Olson, O. Fujita, K. Nishizawa, K. Ito, and T. Kashiwagi. Effect of Wind Velocity on Flame Spread in Microgravity. In *Twenty-Ninth Symposium (International) on Combustion*, pages 2553–2560. Combustion Institute, Pittsburgh, Pennsylvania, 2002. 4
- [14] Y. Nakamura, T. Kashiwagi, K.B. McGrattan, and H.R. Baum. Enclosure Effects on Flame Spread over Solid Fuels in Microgravity. *Combustion and Flame*, 130:307–321, 2002. 4
- [15] W.E. Mell, K.B. McGrattan, and H.R. Baum. g-Jitter Effects on Spherical Diffusion Flames. *Microgravity Science and Technology*, 15(4):12–30, 2004. 4
- [16] A. Mukhopadhyay and I.K. Puri. An Assessment of Stretch Effects on Flame Tip Using the Thin Flame and Thick Formulations. *Combustion and Flame*, 133:499–502, 2003. 4
- [17] A. Hamins, M. Bundy, I.K. Puri, K.B. McGrattan, and W.C. Park. Suppression of Low Strain Rate Non-Premixed Flames by an Agent. In *Proceedings of the 6th International Microgravity Combustion Workshop, NASA/CP-2001-210826*, pages 101–104. National Aeronautics and Space Administration, Lewis Research Center, Cleveland, Ohio, May 2001. 4
- [18] K.B. McGrattan, R.G. Rehm, and H.R. Baum. Fire-Driven Flows in Enclosures. *Journal of Computational Physics*, 110(2):285–291, 1994. 4
- [19] P. Friday and F. W. Mowrer. Comparison of FDS Model Predictions with FM/SNL Fire Test Data. NIST GCR 01-810, National Institute of Standards and Technology, Gaithersburg, Maryland, April 2001. 6
- [20] A. Bounagui, N. Benichou, C. McCartney, and A. Kashef. Optimizing the Grid Size Used in CFD Simulations to Evaluate Fire Safety in Houses. In *3rd NRC Symposium on Computational Fluid Dynamics, High Performance Computing and Virtual Reality*, pages 1–8, Ottawa, Ontario, Canada, December 2003. National Research Council, Canada. 6
- [21] R.L. Alpert. *SFPE Handbook of Fire Protection Engineering*, chapter Ceiling Jet Flows. National Fire Protection Association, Quincy, Massachusetts, 3rd edition, 2003. 6
- [22] A. Bounagui, A. Kashef, and N. Benichou. Simulation of the Dynamics of the Fire for a Section of the L.H.-La Fontaine Tunnel. IRC-RR- 140, National Research Council Canada, Ottawa, Canada, K1A0R, September 2003. 6
- [23] Y. Xin. Assessment of Fire Dynamics Simulation for Engineering Applications: Grid and Domain Size Effects. In *Proceedings of the Fire Suppression and Detection Research Application Symposium, Orlando, Florida*. National Fire Protection Association, Quincy, Massachusetts, 2004. 6
- [24] J.A. Ierardi and J.R. Barnett. A Quantitative Method for Calibrating CFD Model Calculations. In *Proceedings of the CIB-CTBUH International Conference on Tall Buildings*, pages 507–514. International Council for Research and Innovation in Building and Construction (CIB), 2003. 6
- [25] G. Heskestad. *SFPE Handbook of Fire Protection Engineering*, chapter Fire Plumes, Flame Height and Air Entrainment. National Fire Protection Association, Quincy, Massachusetts, 3rd edition, 2002. 6

- [26] N.M. Petterson. Assessing the feasibility of reducing the grid resolution in fds field modeling. Fire Engineering Research Report 2002/6, University of Canterbury, Christchurch, New Zealand, March 2002. 6
- [27] A. Musser, K. B. McGrattan, and J. Palmer. Evaluation of a Fast, Simplified Computational Fluid Dynamics Model for Solving Room Airflow Problems. NISTIR 6760, National Institute of Standards and Technology, Gaithersburg, Maryland, June 2001. 6
- [28] K.B. McGrattan, S. Hostikka, J.E. Floyd, H.R. Baum, R.G. Rehm, W.E. Mell, and R. McDermott. Fire Dynamics Simulator (Version 5), Technical Reference Guide, Volume 1: Mathematical Model. NIST Special Publication 1018-5, National Institute of Standards and Technology, Gaithersburg, Maryland, October 2007. 7, 20
- [29] W. Zhang, A. Hamer, M. Klassen, D. Carpenter, and R. Roby. Turbulence Statistics in a Fire Room Model by Large Eddy Simulation. *Fire Safety Journal*, 37:721–752, 2002. 7
- [30] J. Smagorinsky. General Circulation Experiments with the Primitive Equations. I. The Basic Experiment. *Monthly Weather Review*, 91(3):99–164, March 1963. 7
- [31] J.W. Deardorff. Numerical Investigation of Neutral and Unstable Planetary Boundary Layers. *Journal of Atmospheric Sciences*, 29:91–115, 1972. 7
- [32] M. Germano, U. Piomelli, P. Moin, and W.H. Cabot. A Dynamic Subgrid-Scale Eddy Viscosity Model. *Physics of Fluids A*, 3(7):1760–1765, 1991. 7
- [33] D.K. Lilly. A Proposed Modification of the Germano Subgrid-Scale Closure Method. *Physics of Fluids A*, 4(3):633–635, 1992. 7
- [34] J. Hietaniemi, S. Hostikka, and J. Vaari. FDS Simulation of Fire Spread – Comparison of Model Results with Experimental Data. VTT Working Papers 4, VTT Building and Transport, Espoo, Finland, 2004. 8
- [35] C. Lautenberger, G. Rein, and C. Fernandez-Pello. The application of a genetic algorithm to estimate the material properties for fire modeling from bench-scale fire test data. *Fire Safety Journal*, 41:204–214, 2006. 8
- [36] J.C. Adams, W.S. Brainerd, J.T. Martin, B.T. Smith, and J.L. Wagener. *Fortran 95 Handbook: Complete ISO/ANSI Reference*. MIT Press, Cambridge, Massachusetts, 1997. 9
- [37] R. McDermott. A nontrivial analytical solution to the 2-d incompressible Navier-Stokes equations. http://randy.mcdermott.googlepages.com/NS_exact_soln.pdf, 2003. 11
- [38] G. Comte-Bellot and S. Corrsin. Simple Eulerian time correlation of full- and narrow-band velocity signals in grid-generated, ‘isotropic’ turbulence. *J. Fluid Mech.*, 48:273–337, 1971. 15
- [39] Stephen M. de Bruyn Kops. *Numerical simulation of non-premixed turbulent combustion*. PhD thesis, The University of Washington, 1999. 15
- [40] R. McDermott, A. Kerstein, R. Schmidt, and P. Smith. Characteristics of 1D spectra in finite-volume large-eddy simulations with one-dimensional turbulence subgrid closure. In *58th Annual Meeting of the American Physical Society, Division of Fluid Dynamics*, Chicago, Illinois, November 2005. http://randy.mcdermott.googlepages.com/implicit_filter.pdf. 15, 16

- [41] Y. Morinishi, T. S. Lund, O. V. Vasilyev, and P. Moin. Fully conservative high order finite difference schemes for incompressible flow. *J. Comp. Phys.*, 143:90–124, 1998. 15
- [42] F. E. Ham, F. S. Lien, and A. B. Strong. A fully conservative second-order finite difference scheme for incompressible flow on non-uniform grids. *J. Comp. Phys.*, 177:117–133, 2002. 15
- [43] R. McDermott. Discrete kinetic energy conservation for variable-density flows on staggered grids. In *60th Annual Meeting of the American Physical Society, Division of Fluid Dynamics*, Salt Lake City, Utah, November 2007. http://randy.mcdermott.googlepages.com/aps2007_notes.pdf. 15
- [44] R. McDermott and S. B. Pope. A particle formulation for treating differential diffusion in filtered density function methods. *J. Comp. Phys.*, 226(1):947–993, 2007. 18
- [45] M. Germano, U. Piomelli, P. Moin, and W. Cabot. A dynamic subgrid-scale eddy viscosity model. *Phys. Fluids A*, 3(7):1760–1765, 1991. 18, 20
- [46] M. Pino Martin, U. Piomelli, and G. Candler. Subgrid-scale models for compressible large-eddy simulation. *Theoret. Comput. Fluid Dynamics*, 13:361–376, 2000. 18
- [47] P. Moin, K. Squires, W. Cabot, and S. Lee. A dynamic subgrid-scale model for compressible turbulence and scalar transport. *Phys. Fluids A*, 3(11):2746–2757, 1991. 18
- [48] T. S. Lund. On the use of discrete filters for large eddy simulation. Center for Turbulence Research Annual Research Briefs, 1997. 18
- [49] R. McDermott. Variable density formulation of the dynamic smagorinsky model. Unpublished notes (http://randy.mcdermott.googlepages.com/dynsmag_comp.pdf), 2004. 18
- [50] Stephen B. Pope. *Turbulent Flows*. Cambridge, 2000. 18, 20
- [51] S.B. Pope. Ten questions concerning the large-eddy simulation of turbulent flows. *New Journal of Physics*, 6:1–24, 2004. 19
- [52] J. S. Baggett. Some modeling requirements for wall models in large eddy simulation. *Stanford Center for Turbulence Research Annual Research Briefs*, 1997. 20
- [53] J. S. Baggett. On the feasibility of merging LES with RANS for the near-wall region of attached turbulent flows. *Stanford Center for Turbulence Research Annual Research Briefs*, 1998. 20
- [54] W. Cabot. Large-eddy simulations with wall models. *Stanford Center for Turbulence Research Annual Research Briefs*, 1995. 20
- [55] Pierre Sagaut. *Large Eddy Simulation for Incompressible Flows*. Springer, 2001. 20
- [56] H. Werner and H. Wengle. Large-eddy simulation of turbulent flow over and around a cube in a plate channel. In *8th Symposium on Turbulent Shear Flows*, pages 155–168, 1991. 20
- [57] NIST Web Site. <http://www.fire.nist.gov/wui>. 20
- [58] L. F. Moody. Friction factors for pipe flow. *Transactions of the ASME*, 66, 1944. 20
- [59] H. Tennekes and J. L. Lumley. *A First Course in Turbulence*. MIT Press, 1972. 20
- [60] Bruce R. Munson, Donald F. Young, and Theodore H. Okiishi. *Fundamentals of Fluid Mechanics*. John Wiley and Sons, 1990. 22

- [61] R. Siegel and J. R. Howell. *Thermal Radiation Heat Transfer*. Taylor & Francis, New York, 4th edition, 2002. [37](#), [39](#)
- [62] Y.B. Zel'dovich and Y.P. Raizer. *Physics of shock waves and high-temperature hydrodynamic phenomena*. Dover Publications, New York, 2002. Translated from the Russian and then edited by W.D.Hayes and R.F. Probstein. [40](#), [41](#)
- [63] D.A. Purser. *SFPE Handbook of Fire Protection Engineering*, chapter Toxicity Assessment of Combustion Products. National Fire Protection Association, Quincy, Massachusetts, 3rd edition, 2002. [46](#)
- [64] D. Drysdale. *An Introduction to Fire Dynamics*. John Wiley and Sons, New York, 2nd edition, 2002. [50](#)
- [65] H.S. Carslaw and J.C. Jaeger. *Conduction of Heat in Solids*. Oxford University Press, 2nd edition, 1959. [50](#)
- [66] K.W. Childs. HEATING 7: Multidimensional, Finite-Difference Heat Conduction Analysis Code System. Technical Report PSR-199, Oak Ridge National Laboratory, Oak Ridge, TN, 1998. [51](#)
- [67] R.E. Lyon. Heat Release Kinetics. *Fire and Materials*, 24:179–186, 2000. [63](#)
- [68] R.E. Lyon and R.N. Walters. Pyrolysis Combustion Flow Calorimetry. *Journal of Analytical and Applied Pyrolysis*, 71(1):27–46, March 2004. [64](#)
- [69] American Society for Testing and Materials, West Conshohocken, Pennsylvania. *ASTM D 7309-07, Standard Test Method for Determining the Flammability Characteristics of Plastics and Other Solid Materials Using Microscale Combustion Calorimetry*, 2007. [64](#)